

3D Printing and Supercritical Foaming of Hierarchical Cellular Materials

THÈSE N° 8388 (2018)

PRÉSENTÉE LE 30 AVRIL 2018

À LA FACULTÉ DES SCIENCES ET TECHNIQUES DE L'INGÉNIEUR
LABORATOIRE DE BIOMÉCANIQUE EN ORTHOPÉDIE
PROGRAMME DOCTORAL EN SCIENCE ET GÉNIE DES MATÉRIAUX

ÉCOLE POLYTECHNIQUE FÉDÉRALE DE LAUSANNE

POUR L'OBTENTION DU GRADE DE DOCTEUR ÈS SCIENCES

PAR

Matteo Gregorio Modesto MARASCIO

acceptée sur proposition du jury:

Prof. P. Bowen, président du jury
Prof. D. Pioletti, Dr P.-E. Bourban, directeurs de thèse
Dr F. Thieringer, rapporteur
Prof. R. S. Trask, rapporteur
Dr E. Boillat, rapporteur



ÉCOLE POLYTECHNIQUE
FÉDÉRALE DE LAUSANNE

Suisse
2018

Abstract

Hierarchical porous structures have been gathering interest in different fields owing to their unique properties associated with their multi-scale features. The observation of natural materials brought new insights into the functionality of cellular materials and inspired new processes to produce synthetic hierarchical structures. Such hierarchical cellular materials have shown significant potential in many applications, as filtering, tissue engineering and drug delivery. Polymers in particular gathered a burgeoning interest thanks to their ease of processing, which allows producing structures at high strength/density ratio and high surface area with defined porosity.

In the present study, it is proposed to develop novel technologies to manufacture polymer cellular structures. Hierarchical porous structures were created from the combination of Supercritical Carbon Dioxide Foaming (ScCO₂) and Fused Deposition Modelling / Fused Filament Fabrication (FDM / FFF) additive manufacturing. This process is named homothetic foaming. The material transformation phenomena and the processing window to control this method were studied. The fine-tuning of the foaming parameters allowed creating a micro cellular porosity within a 3D printed structure, without modifying the 3D topology. This permitted producing a wide range of cellular structures with controlled multi scale porosity and stiffness reduced up to hundred times the stiffness of the 3D printed cellular structures.

Homothetic foaming was then applied to biopolymers in order to create gradient hierarchical porous structures. In particular, articular cartilage and bone (osteocondral) defects were targeted. Cartilage repair is a challenging clinical problem because large defects do not regenerate. Tissue engineering offers a solution by implanting a material, defined as scaffold, loaded with cells to induce a regeneration in the tissue that otherwise would not occur. Multi material Poly(lactide-co-caprolactone) – Poly(lactide-βTCP) cellular structures were successfully processed into a scaffold able to replicate the complex gradient mechanical properties of the osteocondral tissue. In particular, the processing windows to produce multi material 3D printed and foamed structures was established. The mechanical properties under compression of these scaffolds were compared to the values measured by nanoindentation on human articular cartilage, showing a good correlation between scaffold and target application.

Furthermore, from the developed knowledge, a novel additive manufacturing method is proposed from the integration of FDM/FFF and ScCO₂ into a single process, named 3D Foam Printing. 3D Foam Printing was applied to process structures with hollow filaments or filaments with radial porosity. The influence of processing parameters on foam morphology was investigated. Different cellular structures achievable by tuning the printing temperature and speed were described for different biomaterials.

The processes described in this work allowed mimicking the complex mechanical properties of the osteocondral tissue, a natural hierarchical material. In addition, the developed processes are relevant to a wide range of materials, as polymers, blends and composites. This is particularly true for 3D Foam Printing, which could positively influence many engineering applications, as aerospace, medicine and energy, where tuneable cellular polymers are highly demanded.

Keywords

Hierarchical cellular structures, supercritical foaming, extrusion based additive manufacturing, multi material structures, medical polymers

Résumé

Les structures poreuses suscitent un intérêt croissant dans différents domaines en raison de leurs propriétés uniques associées à leurs caractéristiques multi-échelle. L'observation de matériaux naturels a apporté de nouvelles perspectives sur la fonctionnalité des matériaux cellulaires et a inspiré de nouveaux procédés de fabrication de ces structures. Ces matériaux cellulaires ont suscité un intérêt significatif pour de nombreuses applications, comme le filtrage, l'ingénierie tissulaire et les systèmes d'administration de médicaments. Les polymères sont intéressants en raison de leur facilité à être transformés, permettant de produire des structures avec un rapport résistance/densité et une surface spécifique élevés. Dans cette étude, de nouvelles technologies pour fabriquer des structures cellulaires en polymère sont proposées. Le moussage au dioxyde de carbone supercritique (ScCO₂) et l'impression 3D par extrusion de polymère (FDM/FFF) sont combinés pour créer des structures hiérarchiques micro et macro poreuses. Les phénomènes de transformation des matériaux et la fenêtre de mise en œuvre de ce procédé ont été étudiés. Le réglage des paramètres de moussage a permis de créer une porosité micro-cellulaire au sein d'une structure imprimée en 3D, sans modifier la topologie 3D. Ce procédé a été nommé moussage homothétique. Cette approche a permis de produire une large gamme de structures cellulaires avec une macro et microporosité contrôlée présentant des rigidités jusqu'à cent fois plus faibles que celles des structures cellulaires imprimées en 3D.

Le moussage homothétique a ensuite été appliqué aux biopolymères pour créer des structures hiérarchiques possédant des gradients de porosité pour des applications d'ingénierie tissulaire. La réparation du cartilage est un problème clinique complexe car une fois endommagé, il se régénère difficilement. L'ingénierie tissulaire offre une solution en implantant un matériau chargé de cellules et servant de support pour induire une régénération du tissu. Des structures cellulaires combinant Poly(lactide-co-caprolactone) et Poly(lactide-βTCP) ont été produites dans une structure qui reproduit le gradient complexe des propriétés mécaniques du tissu ostéochondral. En particulier, les fenêtres de mise en œuvre pour produire une structure composée par une partie imprimée et une partie imprimée puis moussée ont été décrites. Les propriétés mécaniques en compression de ces structures ont été comparées aux valeurs mesurées par nanoindentation sur des cartilages articulaires humains et une bonne corrélation fut observée.

De plus les connaissances développées ont permis de proposer une nouvelle méthode de fabrication additive, intégrant les procédés FDM/FFF et ScCO₂ en un seul procédé, l'impression 3D de mousses. Ce procédé, appelé moussage homothétique, a été appliqué pour la production de structures avec des filaments creux ou avec des gradients de porosité. L'influence de la température et de la vitesse d'impression sur la morphologie finale a été étudiée pour différents polymères.

Les procédés proposés ont permis de fabriquer des structures à base de polymères, de mélange de polymères et de composites reproduisant les propriétés du tissu ostéochondral. L'impression 3D de mousse ouvre de nouveaux horizons pour d'autres applications, par exemple en aérospatiale, en médecine et ou dans les domaines de l'énergie, où les polymères à structures cellulaires hiérarchiques sont très demandés.

Mots-clés

Structures cellulaires hiérarchiques, moussage supercritique, fabrication additive à base d'extrusion, structures en multi-matériaux, polymères médicaux

Acknowledgements

This work was carried out in the framework of an excellent collaboration between two laboratories, the Laboratory for Processing of Advanced Composites (LPAC-EPFL) and the Laboratory of Biomechanical Orthopedics (LBO-EPFL) and supported by the Swiss National Science Foundation (grant 2000021-150190).

All the work described in this Thesis would not be possible without the essential contribution of many people that helped throughout these four years.

Professor Jan-Anders Månson, which gave me the opportunity to start my PhD in what was called Laboratory of Polymer and Composite Technology (LTC-EPFL) at first and Professor Veronique Michaud to renewing this trust to continue at the Laboratory for Processing of Advanced Composites (LPAC-EPFL).

Professor Dominique Pioletti, head of LBO, which welcomed me in his laboratory, for his continuous and constant feedbacks from the first day to the very end.

Dr. Pierre-Etienne Bourban, which deserves the highest of the acknowledgements for being a constant source of discussion, positive vibration and improvements, always finding the time to share a chat and celebrate small and big achievements.

Dr. Christopher Plummer and Dr. Yves Leterrier, for the discussions and guidance during the PEXs that flew into the results that compose this Thesis.

The LBO and Discovery Learning Lab (DLL) teams, for their help to achieve part of the results here described and for being always ready to challenge me with productive discussions.

The EPFL Technology Transfer Office (TTO – EPFL), for supporting the valorisations of this work into a patent.

The ETH-EPFL Doctoral School and the CCMX, in the person of Carey Sargent, for sponsoring and helping me organizing the 3D Printing Summer School at the EPFL.

The LTC team and the LPAC team, the big family that welcomed me 5 years ago and with whom I shared some of the happiest and enjoyable moments of my life as a PhD.

Alessandra, that believed in that nerdy student 5 years ago and helped him turning into the author of this Thesis.

Amaël Cohades, for the beers, the discussions on good music and sharing the path during these 4 years. Jens Antons, for being an excellent source of inspiration and an extraordinary research partner during these four years.

Damiano and Chiara, for welcoming me home with a smile and bearing my guitar&voice session in the evenings. Federica, Marta, Lara, Luis, Tommaso, Claudia, Fabio, Barış, Bushra, Anja and all the good friends, for connecting the dots between work and free time and allowing me to never go short of good laughs.

To Miriam, for the incessant love and support during the unavoidable up and down of this journey.

To my family, for being there to help me to hold the ship's wheel in stormy water.

Ad maiora

Table of Contents

ABSTRACT	II
RÉSUMÉ.....	III
ACKNOWLEDGEMENTS.....	V
TABLE OF CONTENTS	VIII
CHAPTER 1 INTRODUCTION AND MOTIVATION	2
1.1 INTRODUCTION	2
1.2 OBJECTIVES.....	3
1.3 APPROACH.....	3
CHAPTER 2 STATE OF THE ART	6
2.1 CELLULAR STRUCTURES.....	6
2.2 MECHANICS OF CELLULAR STRUCTURES.....	8
2.3 PROCESSING CELLULAR STRUCTURES.....	9
2.3.1 <i>Solvent casting / particulate leaching</i>	9
2.3.2 <i>Freeze drying</i>	10
2.3.3 <i>Gas foaming</i>	10
2.4 ADDITIVE MANUFACTURING	12
2.4.1 <i>Stereolithography</i>	13
2.4.2 <i>Inkjet printing</i>	13
2.4.3 <i>Selective laser sintering (SLS)</i>	13
2.4.4 <i>Melt extrusion/fused deposition modelling (FFF/FDM)</i>	13
2.4.5 <i>Cellular materials in nature</i>	16
2.5 BIOMATERIALS.....	16
2.5.1 <i>Natural-based polymers</i>	16
2.5.2 <i>Synthetic polymers</i>	16
2.5.3 <i>Ceramics</i>	17
2.5.4 <i>Hydrogels</i>	17
2.5.5 <i>Composites</i>	17
2.6 APPLICATIONS OF CELLULAR MATERIALS: OSTEOCHONDRAL SCAFFOLDS	18
2.6.1 <i>Osteochondral tissue</i>	18
2.6.2 <i>Composition of the osteochondral tissue</i>	19
2.6.3 <i>Osteochondral defects</i>	20
2.6.4 <i>Osteochondral tissue engineering</i>	21
2.6.5 <i>Requirements for osteochondral tissue engineering</i>	22
2.6.6 <i>Scaffold design for osteochondral tissue engineering</i>	23
2.6.7 <i>Mechanical properties of the osteochondral tissue</i>	25
2.6.8 <i>Measurements of the articular cartilage local stiffness</i>	26
2.7 CONCLUSIONS AND CHALLENGES	28
CHAPTER 3 MATERIALS AND METHODS.....	32
3.1 MATERIALS	32
3.1.1 <i>Model materials</i>	32

3.1.2	<i>Medical materials</i>	32
3.2	PROCESSING METHODS.....	33
3.2.1	<i>Filament extrusion</i>	33
3.2.2	<i>FDM /FFF 3D Printing</i>	34
3.2.3	<i>Supercritical CO₂ Foaming</i>	34
3.3	CHARACTERIZATION METHODS	35
3.3.1	<i>Dynamic Calorimetric Scanning (DSC)</i>	35
3.3.2	<i>Thermogravimetric Analysis (TGA)</i>	36
3.3.3	<i>Foam density and porosity</i>	36
3.3.4	<i>Compression behaviour of 3D printed structures and foams</i>	37
3.3.5	<i>Fracture mechanics</i>	38
CHAPTER 4	HOMOTHETIC FOAMING OF 3D PRINTED STRUCTURES	40
4.1	INTRODUCTION	40
4.2	MATERIALS AND METHODS.....	41
4.2.1	<i>Materials</i>	41
4.2.2	<i>Foaming processing conditions</i>	41
4.2.3	<i>3D printing</i>	41
4.3	PROCESSING CELLULAR STRUCTURES.....	41
4.3.1	<i>Partial foaming</i>	42
4.4	HOMOTHETIC FOAMING OF 2D AND 3D PRINTED STRUCTURES.....	48
4.4.1	<i>Morphology and porosity</i>	48
4.4.2	<i>Properties of cellular structures</i>	53
4.5	CONCLUSIONS	56
CHAPTER 5	HOMOTHETIC FOAMING OF 3D PRINTED MULTI-MATERIAL STRUCTURES.....	58
5.1	INTRODUCTION.....	58
5.2	MATERIALS AND METHODS.....	58
5.2.1	<i>3D Printing</i>	58
5.3	MONO MATERIAL SCAFFOLDS	61
5.3.1	<i>Morphology</i>	61
5.3.2	<i>Mechanical properties of the printed cellular structures</i>	62
5.3.3	<i>Fracture toughness at the interface of mono material structures</i>	65
5.4	MULTI MATERIAL SCAFFOLDS.....	69
5.5	MULTI MATERIAL FOAMED SCAFFOLDS.....	72
5.5.1	<i>Mechanical properties of 3D printed and foamed multi material scaffolds</i>	75
5.6	CONCLUSIONS	77
CHAPTER 6	3D FOAM PRINTING.....	80
6.1	INTRODUCTION	80
6.2	MATERIALS AND METHODS.....	80
6.2.1	<i>Material selection</i>	80
6.2.2	<i>Filament saturation</i>	80
6.2.3	<i>Printing 3D foams</i>	81
6.2.4	<i>Strands expansion and porosity</i>	81
6.2.5	<i>Mechanical properties</i>	81
6.3	RESULTS	81
6.3.1	<i>Filament saturation</i>	82
6.3.2	<i>Strand expansion</i>	83

Introduction and Motivation

6.3.3	Pores morphology and porosity distribution.....	84
6.3.4	Strand-to-strand interface	87
6.3.5	Pores density evolutions.....	87
6.3.6	Strand mechanical properties	88
6.3.7	3D printing of medical foams.....	89
6.4	CONCLUSIONS	91
CHAPTER 7	CONCLUSIONS AND PERSPECTIVES	94
7.1	CONCLUSIONS	94
7.2	PERSPECTIVES.....	96
7.2.1	Increase open porosity.....	96
7.2.2	Interface quality of a 3D Printed structure	97
7.2.3	Optimization of 3D Foam Printing	97
7.3	TOWARDS APPLICATIONS	97
ANNEX I	CELLS RESPONSE TO BIOMATERIAL	100
AI.1	MATERIALS AND METHODS.....	100
AI.1.1	3D Printing	100
AI.1.2	Homothetic foaming	100
AI.2	RESULTS	100
AI.2.1	Cells viability on 3D printed scaffolds	100
AI.2.2	Cells viability in 3D printed, foamed and impregnated scaffolds.....	102
AI.3	CONCLUSIONS	105
ANNEX II	MEDICAL FILAMENTS EXTRUSION	106
AII.1	INTRODUCTION	106
AII.2	MATERIALS AND METHODS.....	106
AII.2.1	Materials.....	106
AII.2.2	Characterization.....	106
AII.3	PROCESSING WINDOWS	106
AII.3.1	Food grade model material PLAm1.....	106
AII.3.2	Medical materials	109
AII.4	PROCESSING INFLUENCE ON FILAMENTS AND 3D PRINTED STRUCTURE PROPERTIES	113
AII.5	CONCLUSIONS	116
BIBLIOGRAPHY	118
CURRICULUM VITAE	130

Chapter 1 Introduction and Motivation

1.1 Introduction

Polymer composites are getting more and more applied in different fields, as transportation, sport, aeronautics, and mechanical industry ^{1,2}. This is due to their excellent mechanical properties and lightness, an unique combination that allows energy and space savings ³. Moreover, polymer composites can be tailored in all their properties with a high degree of freedom, thanks to their potential of being processed with various methods.

Materials for biomedical applications are largely investigated nowadays, especially after the introduction of tissue engineering approaches for regenerative medicine. In particular, biocomposites invest a special role, thanks to their specific mechanical properties, high freedom of design and lightness. Moreover, the knowledge acquired in other fields is often translated into biomaterials, permitting to create new solutions and innovative approaches (e.g. drug delivery systems). Finally, natural tissue can be described as composites, due to intrinsic tissue complexity and presence of different phases.

Bone is a natural porous composite structure, consisting of an organic matrix of collagen fibres and a mineral support of hydroxyapatite. It has an interconnected porous microstructure with a gradient of pore sizes. Articular cartilage is a specialized load-bearing and hydrated soft tissue that covers the articulated surface of bones. From a material science point of view, cartilage is a fibre-reinforced composite made of a dense stable network of collagen fibres embedded in a very high concentration of proteoglycan gel.

An osteochondral defect results from a lesion that involves the hyaline cartilage and the underlying subchondral bone. It is a typical situation arising following a traumatic injury in sport and thus concerns mainly the young active population. As cartilage tissue has a very limited healing potential, degenerative arthritis is a natural evolution of this situation. To avoid the tissue degeneration, which would ultimately lead to the need of a total joint arthroplasty, several techniques are used in clinical practice to repair the cartilage, such as drilling, autograft and allograft. All of them, however have shown to have a limited success, especially in the long-term ^{4,5}. Tissue engineering has emerged as a possible solution to overcome this issue, inducing the tissue to regenerate the defect and ideally leading to a complete wound healing.

Tissue engineering is a multidisciplinary field that joins developments in cell/molecular biology, materials science and engineering, chemistry and medical science towards the development of hybrid substitute combining biodegradable scaffold, cells and signalling molecules such as growth factors aimed at restoring tissue or organs functions ⁵. Tissue engineering has the potential to be used in the regeneration of organs or tissues such as articular cartilage and is considered as a potential osteoarthritis treatment strategy superior to the current surgical techniques ⁴⁻⁷. This is due to limited results of conventional surgery procedure in the long term and the symptomatic approach, which lead thus a chronic or periodic treatment ⁸. Thus, the aim of cartilage tissue engineering is to promote long-lasting, functional repair of defective articular cartilage lesions through the development and ex vivo manufacture of implantable artificial cartilage tissue substitutes ⁹.

Polymer foams and bio-printed structures are currently being investigated for use in tissue engineering. Mechanical properties of these cellular solids can be varied by tailoring the morphology of the pores, the properties of the raw material and the density of the foam ¹⁰. Physical foaming techniques such as gas foaming are preferred in the biomechanical field as they are solvent free, do not involve chemical reactions and are

less toxic for added bioactive species ^{11,12}. For the same reason, 3D printing is acquiring more and more attention for biomedical structures. Moreover, this technique allows an incredible degree of freedom to design scaffold structure, obtaining for the first time scaffold 100% interconnected and 100% reproducible ¹³. Hydrogels are an appealing scaffold material because they are structurally similar to the extracellular matrix of many tissues such as articular cartilage. Integration of hydrogels with thermoplastic porous structure to mimic soft and strong cartilage feature is a cutting-edge approach for Biofabrication ^{14–17}. However, issues regarding process windows, transformation and combination of thermoplastic materials still limit the current approaches.

1.2 Objectives

The research will particularly focus to:

- ✓ Propose and process novel hierarchical cellular structures of thermoplastic polymers.
- ✓ Analyse local properties of the cartilage, extrapolating by instrumental indentation the stiffness of the different hierarchical layers composing the tissue.
- ✓ Print 3D structures of medical thermoplastics by Fused Deposition Modelling / Fused Filament Fabrication (FDM/FFF) 3D printing. Improve the knowledge on the involved material behaviour and processing influence at various manufacturing stages, from granules to the final printed scaffold.
- ✓ Introduce an additional degree of porosity into a 3D printed object, softening the structure and creating a hierarchical cellular geometry. This process involves Supercritical CO₂ and it takes the name of homothetic foaming.
- ✓ Apply homothetic foaming to 3D printed structures to process multi-material structures. In particular only a single material will be foamed without modifying the remaining materials composing the 3D multi material structure.
- ✓ Apply homothetic foaming to produce a structure with similar mechanical properties than the osteochondral tissue. This structure will be composed by a softer layer to mimic cartilage and a stiffer one for the subchondral bone.

Chapter 2 will discuss cellular materials. Processing methods will be here introduced, with a deep focus on the state of the art of supercritical foaming and additive manufacturing. Osteochondral tissue defects will be introduced, describing the requirements to design a valid scaffold for tissue engineering applications. Chapter 3 will discuss the materials selection and the main processing and characterization techniques applied in this study. Chapter 4 will discuss the results on processing of porous structures to create a dual porosity cellular material with a model material, showing the processing windows of a model material to control the homothetic foaming. Chapter 5 will show how to apply homothetic foaming to a single material in a multi-material structure. Such a scaffold, mimicking the mechanical properties of articular cartilage, will therefore be compared with the results retrieved from Chapter 4. A multi material cellular scaffold for osteochondral tissue regeneration will therefore be proposed. Chapter 6 will introduce a novel additive manufacturing technology to deposit porous strands into a hierarchical micro-macro cellular structure, called 3D Foam Printing. Finally, Chapter 7 will present the conclusions and some perspectives.

1.3 Approach

The schematic of the Thesis workflow is shown in Figure 1.1. It is composed by three different stages, described in Chapter 4, Chapter 5 and Chapter 6. Different raw Poly(lactide) based materials are transformed

from granules to input filaments for FDM/FFF 3D Printers and processed into cellular structures. The obtained structures are therefore foamed into an hierarchical cellular structure with a controlled macro and micro porosity. This process takes the name of homothetic foaming. Chapter 4 describes the influence of the foaming parameters on the 3D structures for a neat Poly(lactide), showing how to tune the stiffness of the final structure during the applied processes. Chapter 5 describes how homothetic foaming was applied to medical materials, processing multi materials hierarchical cellular structures. Finally, Chapter 6 discusses how to combine supercritical foaming and 3D Printing into a single process, called 3D Foam Printing. Two annexes complete the work, providing insights into preliminary studies on the biocompatibility of the obtained structures and the processing window to produce controlled FDM/FFF filaments from the raw granular materials.

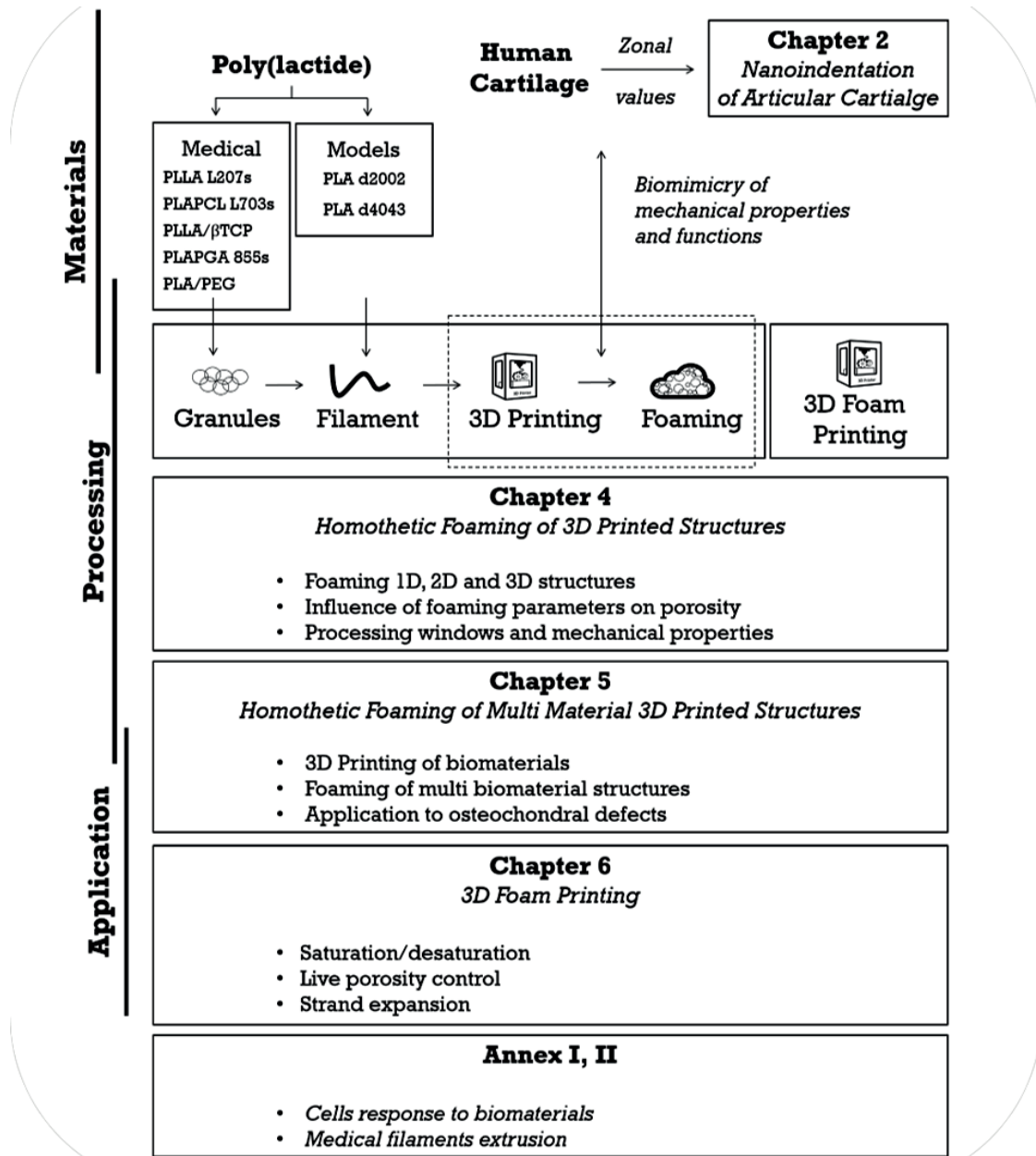


Figure 1.1 Overview of the workflow describing the results discussed in this Thesis.

Chapter 2 State of the Art

This chapter describes first the state of the art in manufacturing of cellular structures. Materials for porous scaffolds are presented, with an emphasis on synthetic thermoplastic polymers. Then the discussion moves to solvent-free approaches, describing carbon dioxide foaming and 3D printing. One of the targeted application is osteochondral tissue engineering. Articular cartilage composition and properties will thus be described, as well as which solutions have been implemented in the past to target such application.

2.1 Cellular structures

Cellular structures are defined as an assembly of cells packed together to fill a volume. In particular, natural cellular materials, as bamboo and beeswax honeycomb, are usually complex hierarchical geometries, designed to carry out a specific task or optimize a specific property. As an example, cellular structure in nature have high stiffness-to-weight ratio, better crash energy absorption, fire resistance, in-flammability, non-toxicity, low thermal conductivity and magnetic permeability and lower density obtained by introducing pores¹⁸. Man has often taken inspiration from natural cellular materials for engineering applications, as light weight construction, crash energy absorption, noise control, heat exchangers, purifiers, decoration and arts and sound damping¹⁹. In the biomedical industry, cellular materials are required to mimic the natural organization of the target tissue, providing a porosity for human cells to proliferate and migrate. This is especially true in tissue engineering applications, where a material, called scaffold, is designed to cause desirable biochemical interactions to contribute to the formation of new functional tissues. A key feature of cellular material is the apparent density, defined as the ratio between the density of the cellular solid (ρ^*) and the density of the bulk material (ρ_0)²⁰ (eq.1)

$$\text{apparent density} = \frac{\rho^*}{\rho_0} \quad \text{eq (1)}$$

Cell wall thickness and cell size define the apparent density of a cellular material. At constant apparent density, an increase of cell size produces a decrease of cell wall thickness and *vice versa* (Figure 2.1). These parameters are also responsible of the overall mechanical properties of a cellular material.

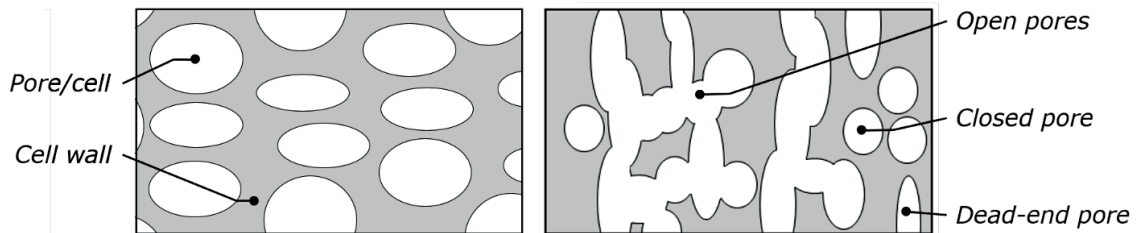


Figure 2.1 Schematic of the structure of a cellular material and of the differences among open, closed and dead-end porosity.

It is important to differentiate between cells in cellular materials and cells in biology. To avoid misunderstanding, cells in cellular materials will be defined as pores. The sum of the volumes of the single pores in a cellular material is defined as porosity.

Porosity can be divided in two main classes, (i) open porosity and (ii) closed porosity. It is common to distinguish these two classes in cellular materials; as different mechanical model applies to the two cases. The open cells are interconnected i.e. a fluid phase can flow from one cell to another and perfuse the structure. On the other hand, closed porosity means that each cell is sealed off from its neighbours, due to the presence of dead-end pores (Figure 2.1) ^{21,22}.

Materials can be processed into cellular structures by different processing methods. Cellular structures are different in terms of pore size, pore morphology and pores distribution. As example, a cellular structure produced by extrusion based additive manufacturing will often differ from one produced by foaming. Figure 2.2Figure 2.2 Schematic of cellular structure typology envisaged in this work. A) Cellular structure produced by particulate leaching or supercritical foaming. B) Particle or fibre reinforced composite cellular structures. C, D) Cellular structures produced by based additive manufacturing. shows a schematic of these different typology of cellular materials. Several manufacturing methods for cellular structure, as freeze-drying, particulate leaching and supercritical foaming, have been used to such cellular structure. The main goals of such processes is to control pore size, morphology and orientation (Figure 2.2A, Figure 2.2B). While sharing the same objective, the principal different among these processes is the quality of the create porosity. In particulate leaching, pore size and morphology are based upon the particulate used (e.g. the pore size will be a function of the particulate diameter). In supercritical foaming, pore size and morphology will be mostly inhomogeneous and pore morphology might show elliptical pores towards one axis. A higher potential to control pore morphology is expressed by extrusion based additive manufacturing methods, as Fused Deposition Modelling / Fused Filament Fabrication (FDM/FFF) (Figure 2.2C, Figure 2.2D). Additive manufacturing technologies are the only up today to be able to process 100% interconnected cellular structure.

Within the scope of this work, we will focus on the processing of polymer cellular materials to tailor porosity at different scales.

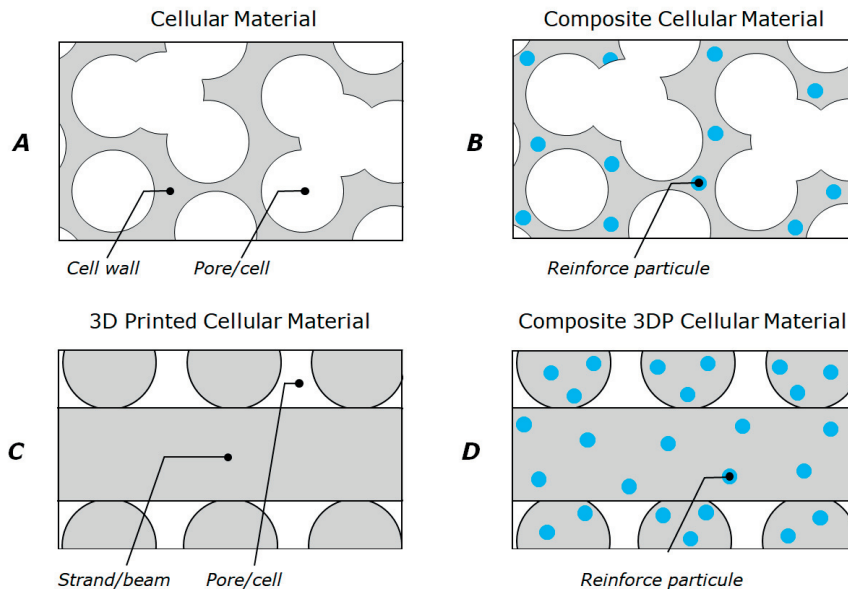


Figure 2.2 Schematic of cellular structure typology envisaged in this work. A) Cellular structure produced by particulate leaching or supercritical foaming. B) Particle or fibre reinforced composite cellular structures. C, D) Cellular structures produced by based additive manufacturing.

2.2 Mechanics of cellular structures

Gibson and Ashby¹⁰ did the most complete study of the mechanics of cellular solids. Their model predicts the Young's modulus of a foam, E^* , and the collapse stress, σ_{pl}^* as a function of the apparent density, ρ^*/ρ_s , the porosity type and the degree of cellular anisotropy. Indices “*” represent the foam properties and “s” the properties of the bulk solid material.

The stress-strain curve of such structures can be divided in three zones Figure 2.3. Zone I corresponds to the linear elastic behaviour of the foam characterized by cell edge bending in open cell foams and additional cell wall elastic stretching in closed cell structures²³. The Young's modulus of the foam E^* is given by the slope of the curve in this zone. Zone II shows a steady plateau. The foam collapses by buckling of cell edges and walls. The last one (zone III) is the densification zone where cell edge and walls come into contact. Further strain compresses the solid itself giving the final region of rapidly increasing stress.

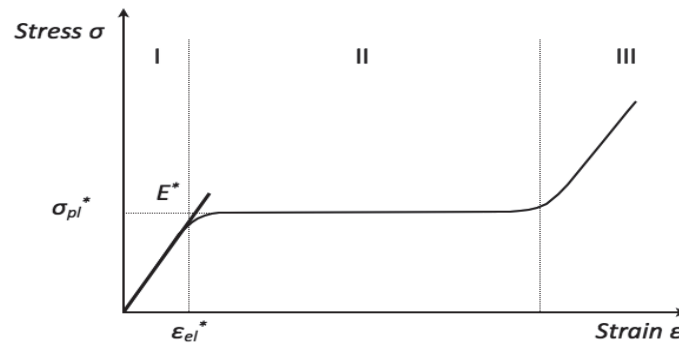


Figure 2.3 Schematic compressive stress-strain curve of model cellular structures²⁴

Gibson and Ashby modelled the cells as a cube with cell edges and cell faces. Figure 2.4 displays the cubic model for an open cell (a), an open cell under load (b) and a closed cell (c) l is the edge length and t the edge thickness.

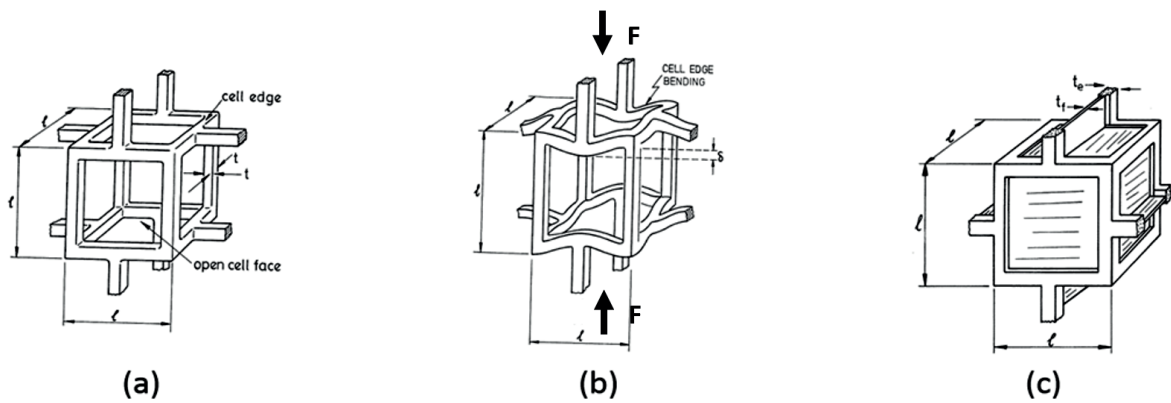


Figure 2.4 The cubic model for (a) open cell, (b) open cell bending during linear elastic deformation and (c) closed cell²⁴

The theoretical relation for isotropic open cell structure is derived from this cubic model, as shown in eq. 2

$$\frac{E^*}{E_s} = C_1 \left(\frac{\rho^*}{\rho_s} \right)^2 \quad eq (2)$$

where E_s the Young's modulus of the solid material, C_1 a constant including the geometric constants of proportionality, ρ^* and ρ_s the foam density and the solid density, respectively.

Cellular structures with closed cell are more complicated to model. Cells of respectively the cellular stretching, perpendicularly to the testing direction occurs in addition to cell edge bending. Moreover, fluid contained within the cells have to be taken into account too because it opposes a significant resistance to compression. The following relation is obtained

$$\frac{E^*}{E_s} \approx \phi^2 \left(\frac{\rho^*}{\rho_s} \right)^2 + (1 - \phi) \frac{\rho^*}{\rho_s} + \frac{\rho_0(1 - 2\nu^*)}{E_s \left(1 - \frac{\rho^*}{\rho_s} \right)} \quad eq (3)$$

where ϕ is the fraction of solid contained in a cell, ρ_0 the initial pressure inside the cell, usually taken as 1 atm, ν^* the foam Poisson coefficient usually considered as constant and equal to 1/3. This model is for foams made of an isotropic material.

This model shows that the Young's modulus of the foam is strongly dependent on the foam density. Open cell foams are required in cartilage tissue engineering. According to equation 2 and equation 3, to decrease the foam density or to use softer polymers are the only ways to decrease the modulus of the resulting foam.

2.3 Processing cellular structures

Various techniques have been reported for the preparation of cellular structures. Many of them commonly generate constructs with poor control of pores interconnectivity, size and distribution. This affects the mechanical properties of the obtained cellular material, resulting in low mechanical strength, structural instability and generally low structure reproducibility. These techniques include solvent casting, freeze drying and foaming²⁵.

Novel methods have been developed on the base of these golden standard technologies. As example, particulate leaching when used with solvent casting allow overcoming some of the limitations of these methods alone. Some other methods have been spontaneously acquired from other fields, such as additive manufacturing based technologies.

2.3.1 Solvent casting / particulate leaching

The process using solvent casting/particulate leaching involves the mixing of water-soluble salt particles into a biodegradable polymer solvent solution. The mixture is then cast into the desired shaped mold and the solvent is removed by vacuum drying and lyophilisation. The water-soluble salt particles are then leached out with water to leave a porous structure. This method is characterized by its adequate control of pore size and porosity of the materials, provided by the amount and size of the particulate²⁶. The particulates typically used in the field are sodium chloride, ammonium bicarbonate, or glucose with different crystal sizes²⁷. This technique has been largely adopted to create cellular scaffold for tissue engineering applications. As an example, porous scaffolds for the growth of endothelial cells have been previously reported²⁸. The achievement of open, interconnected porosity is critical in such applications for ensuring proper nutrient and waste transport, tissue ingrowth, vascularization, and eventually, the integration of the construct within the host

²⁹. While providing a generally acceptable interconnectivity, solvent casting / particulate leaching still generates closed pores which do not contribute to maximize diffusion and homogeneous tissue ingrowth. Moreover, a well-known limit of this manufacturing method is the retrain of particulates within the matrix, mostly due to impossibility to rinse such particles because of low permeability in certain material areas. Finally, the use of solvents requires a further rinsing step to prepare the material for cell seeding.

2.3.2 Freeze drying

This technique is based on the principle of liquid-liquid or solid-liquid phase separation. Phase separation is based on thermodynamic demixing of a homogeneous polymer-solvent solution into a polymer-rich phase and a polymer-poor phase is usually achieved by either exposure of the solution to another immiscible solvent or cooling the solution below a binodal solubility curve. Thermally induced phase separation (TIPS) uses thermal energy as a latent solvent to induce phase separation. The quenched polymer solution below the freezing point of the solvent is subsequently freeze-dried to produce porous structure ²⁶. One of the advantages of this technique is that various porous structures can be easily obtained. However, the solvent sublimation is time-consuming and this method is thus limited to small-scale production. The main drawback of this method is the use of organic solvent.

2.3.3 Gas foaming

CO₂ supercritical foaming was widely used to develop foams at the Laboratory for Processing of Advanced Composites (LPAC). Japon *et al.* ³⁰ developed poly(ethylene terephthalate) PET foams using CO₂ supercritical foaming for applications such as thermal insulation panels and sandwich structure. Mathieu *et al.* ^{11,31,32} have processed porous polymer composites for bone tissue engineering. Foaming of a bioresorbable polymer, PLLA, reinforced with ceramic fillers such as hydroxyapatite (HA) and β -tricalcium phosphate (β -TCP) was carried out using CO₂ supercritical foaming. Structural and mechanical properties similar to those of cancellous bone were demonstrated. These scaffolds have then demonstrated both biocompatibility and osteoconductivity *in vivo* ^{33,34}. Subsequently, with the same PLLA, Bühler *et al.* ^{35–37} developed cellular composites with gradient of fibres content and porosity using the same method. Solvent free foaming with clean physical agent, which is the case for CO₂ supercritical foaming, is thus considered a better alternative and is detailed in the next paragraph.

Odourless, colourless, non-flammable and low reactivity gas, CO₂ can have the properties of supercritical fluids (SCF). Above a critical temperature T_c and pressure P_c , CO₂ shows intermediate properties between those of a liquid and a gas, i.e. a density similar to those of a liquid and a diffusivity and viscosity similar to those of a gas ³⁸. A schematic CO₂ phase diagram is displayed in Figure 2.5. Its critical temperature T_c is 31.06°C and its critical pressure P_c 73.8 bar ²³.

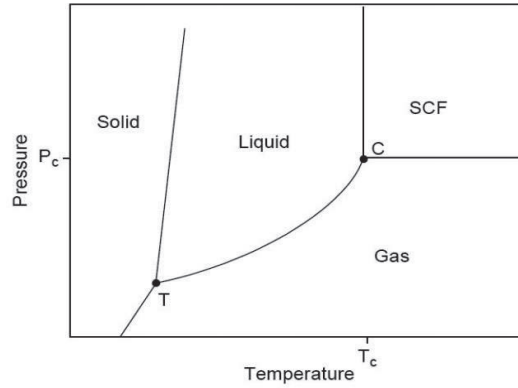


Figure 2.5 Schematic CO₂ phase diagram ($T_c=31.06^\circ\text{C}$; $P_c=73.8$ bar).

The gas foaming process can be decomposed in several steps, (i) gas saturation, (ii) nucleation, (iii) cell growth and (iv) stabilization of the structure. All steps are dependent on gas-polymer interactions. The first step is the CO₂ saturation of the polymer by increasing both pressure and temperature (step 1 and 2 in Figure 2.6). Diffusivity and solubility of the gas, temperature and pressure mainly control the gas dissolution in the molten polymer.

The diffusivity, D , is influenced by the nature of the gas component. A large gas molecule diffuses slower than a small one or the more crystalline the polymer is, the more difficult the gas diffusion is. The diffusion can be described by the Fick's second law given the change in gas concentration $\partial C/\partial t$ during the diffusion process as a function of the concentration gradient ∇C .

$$\frac{\partial C}{\partial t} = \nabla(D\nabla C) \text{ with } D = D_0 \exp\left(-\frac{E_a}{RT}\right) \quad eq (4)$$

where D_0 is a pre-exponential factor, E_a is the activation energy for diffusion, T is the temperature and R the gas constant. Diffusivity is therefore strongly dependent with increasing temperature.

The solubility, S , or Henry's constant, k_H , defines the maximum gas concentration in the polymer at equilibrium. It depends on the saturation pressure P_{sat} and the saturation temperature T_{sat} . The concentration of gas C at a given temperature and pressure in function of the gas solubility is given by Henry's law (for simple gas at low concentration).

$$S = \frac{C}{P_{sat}} \quad eq (5)$$

In function of these physical laws, the parameters that can be chosen for the processing are T_{sat} , P_{sat} and the saturation time t_{sat} .

Once saturation is completed, dissolved gas/polymer forms a one-phase system in a metastable state. Each small difference in temperature or pressure induces reactions to find another equilibrium state. At this step, the pressure is release quickly and the temperature is decreased. This sudden pressure release is enough to induce bubble nucleation. Free energy of the system is thus lowered to reach a stable state (step 3 in Figure 2.6).

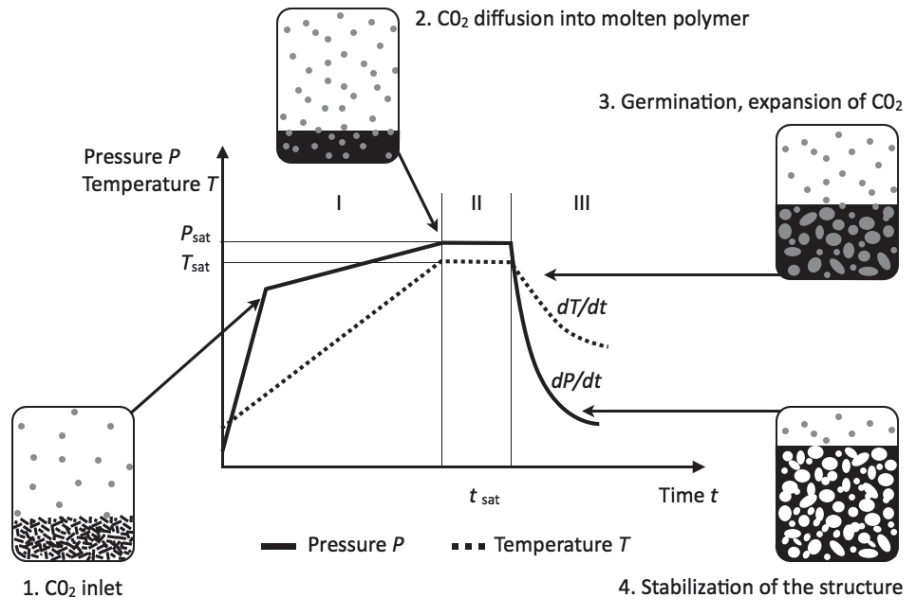


Figure 2.6 Schematic representation of the foaming process ³⁹.

Nucleation will determine pore distribution and density. Three nucleation mechanisms exist, (i) homogeneous, (ii) heterogeneous and (iii) a mixed mode where the two mechanisms modes compete. For example, in presence of fibres, nucleation can occur homogeneously in the matrix but also heterogeneously at the fibre/polymer interface. CO₂ does not dissolve in the wood fibres but these offer sites at which cell nucleation can take place ²³.

The next step is the cell growth induced by pressure difference between the interior and exterior of the pore. The elongational viscosity and polymer surface tension counterbalance this pressure difference. The process parameters governing the cell growth are the depressurization rate $\partial P/\partial t$ and the cooling rate $\partial T/\partial t$. At the end, the temperature is enough low to freeze the structure and foam is obtained (step 4 Figure 2.6).

CO₂ dissolved in the polymer causes a considerable modification of the rheological properties of the polymer. Acting as a plasticizer, the viscosity of the molten polymer is decreased. The addition of reinforcement such as filler or fibre affects the different steps and parameters by nucleation site addition and viscosity modification.

The current limitation of CO₂ foaming is the control of the heat transfer and thus of the fine tuning of pore size and morphology. Moreover, a non-porous layer of material covers the outer edge of the structure, preventing the porosity to be externally exposed. Finally, the pores morphology is often poorly interconnected, generating cellular structures with low permeability.

2.4 Additive manufacturing

In recent years, a number of automated fabrication methods have been employed to create scaffolds with well-defined architectures ^{40,41}. These have been classified as additive manufacturing (AM), which seems to be the most used name, but also as rapid prototyping (RP) technologies and solid freeform fabrication (SFF)

techniques. Computer-aided design is applied to obtain precise geometries, with the possibility to tailor the shape on anatomical medical imaging, as MRI ^{42,43}. Together with the development of biomaterials suitable for these techniques, the automated fabrication of scaffolds with tuneable, reproducible and mathematically predictable physical properties has become a fast-developing research area ¹⁴.

2.4.1 Stereolithography

Stereolithography (SLA) is a laser-based method applied to create 3D solid objects from UV-sensitive photopolymers and it is normally classified with the family of VAT photo polymerization. This processes usually employ two distinct methods of irradiation. The first method is a mask-based method in which an image is transferred to a liquid polymer by irradiating through a patterned mask. The second method is a direct writing process using a focused UV ⁴⁴. Two laser sources are normally applied: a UV laser or a projector.

2.4.2 Inkjet printing

The process deposits a stream of micro particles of a binder material over the surface of a powder bed, joining particles together where the object is to be formed. A piston lowers the powder bed so that a new layer of powder can be spread over the surface of the previous layer and then selectively joined to it. The process is repeated until the 3D object is completely formed ^{45,46}.

2.4.3 Selective laser sintering (SLS)

This technique uses a laser emitting infrared radiation, to selectively heat powder material just beyond its melting point. The laser traces the shape of each cross-section of the model to be built, sintering powder in a thin layer. After each layer is solidified, the piston over the model retracts to a new position and a new layer of powder is supplied using a mechanical roller ⁴⁷.

2.4.4 Melt extrusion/fused deposition modelling (FFF/FDM)

The FDM process creates 3-D objects from a CAD file as well as digital data produced by an imaging source such as computer tomography (CT) or magnetic resonance imaging (MRI)⁴⁸. The process begins with the design of a conceptual geometric model on a CAD workstation. The design is imported into a software, which mathematically slices the conceptual model into horizontal layers. Toolpaths are generated before the data is downloaded to the FDM hardware. The FDM extrusion head operates in the X and Y axes while the platform lowers in the Z-axis for each new layer to form. In effect, the process draws the designed model (scaffold) one layer at a time. Thin thermoplastic filaments or granules are molten and extruded through a nozzle in a layer-by-layer fashion to form a 3D object. The material leaves the extruder in a liquid form and hardens immediately. The previously formed layer, which is the substrate for the next layer, must be maintained at a temperature just below the solidification point of the thermoplastic material to assure good interlayer adhesion (Figure 2.7).

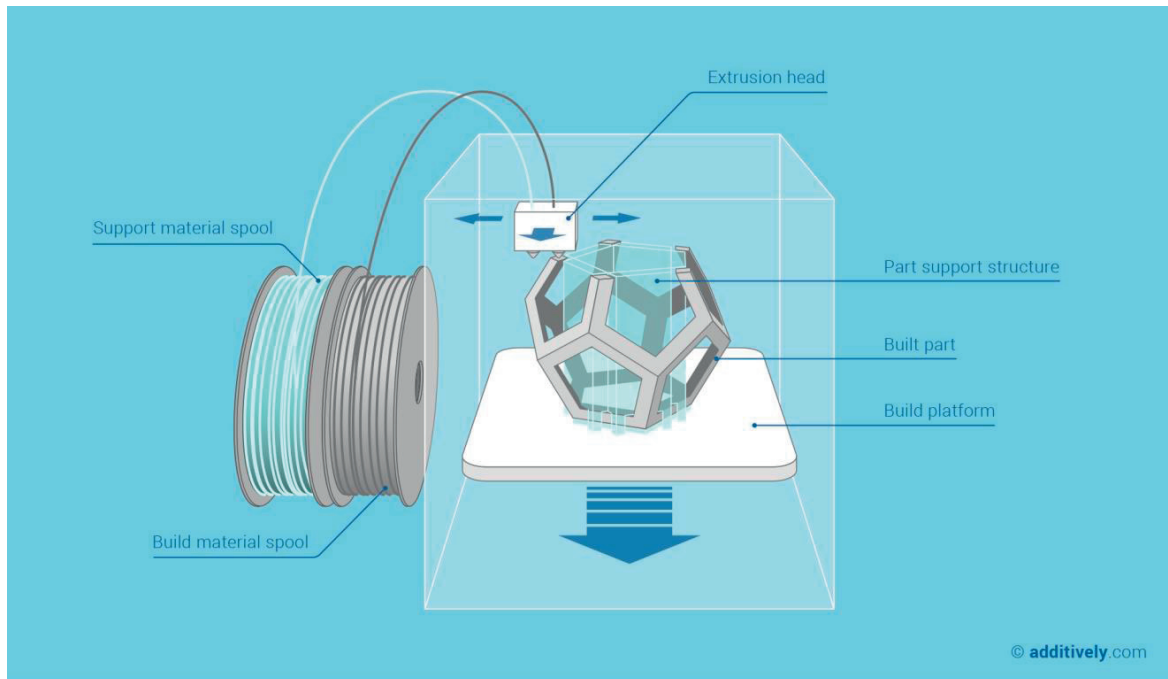


Figure 2.7 Graphic representing the main components of Fused Filament Fabrication or Fused Deposition Modelling machines (FFF/FDM 3D Printing). A thermoplastic material is fed in form of filament (or less commonly granules) from the feeding zone through the hot end.

With the expire of the patents protecting this technology, many companies flood the market with a variety of thermoplastics available in form of filament, ready to be printed. However, most of these are PLA and ABS matrixes with metal, wood and ceramic inclusions to improve mechanical properties, thermal stability and conductivity, electrical conductivity and printing aesthetics. In the last 5 years, a key buzzword in technical extrusion based printing has been “techno polymers”, describing a pool of advanced polymers with over standing mechanical properties, mostly deriving from hard engineering applications, as space and aerospace. Among the others, PEEK, PEK and POI represents the most represented. Those materials are mostly consumed in the high-end segment of the market, where the customization freedom of 3D printing meets precise mechanical requirements. From the consumer side, representing the low-end segment of the market, “classic” thermoplastics have been processed in form of filament. Among them, PP, PPS, PC, PETG, ASA, HIPS, PVA, TPU and many others have been applied to 3D printing application with alternate results. A list of the thermoplastic materials nowadays available as filaments for FDM/FFF machines is shown in Table 1.

FFF/FDM printing has been emerged as a powerful technique to process cellular structures. Overcoming some of the key limitation of other methods, as geometry complexity and ease of processing, this additive manufacturing technology has been reported to produce engineered materials with tailored properties. An example, honeycombs materials with high energy absorbing efficiency have been produced from TPU filaments⁴⁹. In medical application, FFF/FDM printing is still mostly confined to pre-surgical modelling, producing anatomical models that are used as reference by surgeons to plan the surgery. PLA is the most printed material, thanks to the low price, high geometrical stability and ease of printability. In vivo application of 3D printed resorbable structures has mostly been confined to PCL printing, thanks to its low melting temperature (60 °C) and high biocompatibility⁵⁰. For bone graft applications, PLLA-co-BTCP, PLA-co-CaP and PCL-co-

BTCP blends have been investigated as well, showing similar biocompatibility to scaffolds produced by standard methods^{51–53}. A great example of a successful application of in vivo 3D printing in medicine is the manufacturing of an ad-hoc skull bone in PMMA, a non resorbable thermoplastic⁵⁴. This case study showed how the customization and low-cost of extrusion based 3D printing shall represent a huge advantage in the future of medical applications.

Table 1. Materias nowadays available as FDM/FFF filaments (produced by various companies).

ACRONYMUS	MATERIAL
PLA	Poly(lactide) Acid
PLLA	Poly(L-lactide)
ABS	Acrylonitrile Butadiene Styrene
PCL	Poly(caprolactone)
PP	Poly(propylene)
PPS	Poly(phenylene) Sulphide
PC	Poly(carbonate)
PVA	Poly(vinyl alcohol)
PETG	Poly(ethylene) Terephthalate Glycol
PMMA	Poly(methyl methacrylate)
ASA	Acrylonitrile Styrene Acrylate
HIPS	High Impact Poly(styrene)
TPU	Thermoplastic Poly(urethane)
PEEK	Poly(ether) Ether Ketone
PEI	Poly(etherimide)
PEKK	Poly(etherketoneketone)
PEK	Poly(etherketone)

The current main limitation of cellular structures processing by FFF/FDM is the impossibility to increase the total porosity over a certain threshold. This is due to deposition of solid strands of materials in a layer-by-layer fashion. While it is possible to precisely control the deposition of such strands, defining the porosity, no technology allows the deposition of porous strands. Minimum layer height and strand diameter are a function of the nozzle size. However, the nozzle size cannot be freely decreased without jeopardizing the printing speed and increasing the back pressure on the filament. Anyway the nozzle size rarely allows a smooth printing below 0.1 mm.

2.4.5 Cellular materials in nature

Hierarchical porous structures have been gathering interest in different fields due to their unique properties associated with their multi-scale features. Their unusual attributes derive from the precise functional adaptation of the structure at all levels of hierarchy. The observation of natural materials brought new insights into the functionality of cellular materials. Wood, trabecular bone, butterfly, leaves and bamboo possess a unique hierarchical cellular structure that allows mechanical properties otherwise impossible to achieve. Understanding of such materials have inspired new processes to produce synthetic hierarchical structures. Such hierarchical porous materials have shown significant potential in many applications, as energy conversion and storage, catalysis, separation, tissue engineering and drug delivery. Polymers in particular gathered a burgeoning interest because of the easy processing, allowing to produce structures at high strength/density ratio and high surface area with defined porosity.

2.5 Biomaterials

Biomaterials can be described as a set of materials suitable for introduction in the human part, often integrated in a medical device or into a living tissue. From the whole pool of available materials, biomaterials are required to well interface with cells in a harsh and complex environment such as the body. Tissue engineering applications demand require degradable materials, possibly promoting tissue regeneration with the degradation products or at least minimizing the inflammatory response.

In this section, an overview on the material selection for osteochondral tissue engineering application is presented. Four major groups of materials will be discussed: (i) natural and synthetic polymers, (ii) ceramic and glasses, (iii) composites and (iv) hydrogels.

2.5.1 Natural-based polymers

Natural polymers, such as collagen, glycosaminoglycan, chitosan, starch, hyaluronic acid, alginate and bacterial sourced poly(hydroxyalkanoates), are widely used for osteochondral scaffolds. They possess inferior mechanical properties compared to synthetic polymers, ceramics and composites, but offer the advantage of flexibility to adapt their shape to required forms through a variety of molding and casting techniques⁵⁵. Moreover, natural polymers usually retrain the active ECM of the tissue, which can help cells proliferation and differentiation^{56–58}. However, natural material may produce an immunogenic response, requiring thus purification prior to use and they lack of reproducibility, since their composition and properties may vary significantly because of harvesting, age, donor and genetics. Sterilization is a crucial problem for natural-based polymers, as the intrinsic beneficial properties associated with the material might get lost due to the use of aggressive sterilization techniques.

2.5.2 Synthetic polymers

The most popular biodegradable synthetic polymers include poly(α -hydroxy acids), especially poly(lactic acid) (PLA), poly(glycolic acid) (PGA) and their co-polymer (PLGA), poly(ϵ -caprolactone) (PCL), poly(propylene fumarate), poly(dioxanone), polyorthoesters, polycarbonates, polyanhydrides and polyphosphazenes^{59,60}. These polymers offer a wide range of chemical and mechanical variety and can be obtained with controlled distribution of molecular weights. The main advantage of synthetic materials is the deep scientific knowledge of mechanical properties control (i.e. strength, stiffness) and degradation kinetic⁵⁶. They could also be processed by different techniques in different shapes and into cellular structures with controlled porosity⁶¹.

Finally, they are getting more and more interesting thanks to emerging techniques as electrospinning and additive manufacturing^{62–64}. On the other side, synthetic polymers present numerous problems, such as: (i) limited bioactivity due to high hydrophobicity and (ii) induction of pH modification within the tissue, due to degradation product (e.g. PLA degradation). Modification by surface treatments (e.g. with chondroitin sulphate⁶⁵, silicate⁶⁶, collagene⁶⁷, and alkaline⁶⁸) helps improving cell attachment and proliferation, as for inclusion of growth factors (e.g. TGF- β , BMP)^{69,70}.

2.5.3 Ceramics

Ceramics such as hydroxyapatite (HA) or other calcium phosphate (Ca-P) ceramics (including tricalcium phosphate, TCP) or bioactive glasses (such as Bioglass®) are used for bone grafts^{59,71–73}. They promote bone-like tissue formation, due to excellent osteoconductivity and osteoinductivity, well mimicking bone surface chemistry to attract cells and guide their proliferation and differentiation. Often, ceramics find a role as filler in polymer-based composite materials, known to promote bone-like apatite layer formation on their surfaces, improving implant fixation and stability^{74,75}. The main advantage of ceramic materials is their chemical stability, allowing a good implant inertia, a smooth surface and promoting a fainter inflammatory response. However, ceramic implants are susceptible to brittle failure, possible causing severe tissue damage in case of accident. For these reasons, ceramics shines in surface treatments application or for dental implants, where their features are often key success factors.

2.5.4 Hydrogels

Hydrogels are highly hydrated polymer networks and represent an appealing scaffold material because they are structurally similar to the extracellular matrix of many tissues⁷⁶. Hydrogels are defined as hydrophilic polymer networks, which may absorb up to thousands of times their dry weight in water⁷⁷. They are composed of hydrophilic polymer chains, which are either synthetic or natural in origin. Synthetic materials used to form hydrogels include poly (ethylene oxide) (PEO), poly (vinyl alcohol) (PVA), poly (acrylic acid) (PAA), poly (propylene furmarate-co-ethylene glycol) (P(PF-co-EG)) and polypeptides. Synthetic hydrogels give the advantages to control and reproduce their chemistry and properties such as molecular weights, block structure, degradable linkage, and crosslinking mode. Naturally derived polymers are represented by agarose, alginate, chitosan, collagen, fibrin, gelatine, and hyaluronic acid (HA)⁷⁶. The structural integrity of hydrogel depends on crosslinks formed between polymers chains via various chemical bonds and physical interactions. Hydrogels used for scaffold material are typically biodegradable. They can be processed under relatively mild conditions and can be delivered in a minimally invasive manner^{78,79}. A broad discussion on advantages and drawback of hydrogels is required, but the quick evolution of this class of materials and the huge variety of formulations prevent quickly summarizing the points in few lines. As general rule, hydrogels possess inferior mechanical properties compared to other classes of materials and often encounter stability issue due to their biphasic properties (e.g. swelling). However, their similarity to ECM matrix, their high water content and their ease of processing into different viable formulation allow an even higher degree of freedom compare to any other material. For this reason, hydrogel might be considered as the most applied class of material for tissue engineering applications.

2.5.5 Composites

As previously discussed, polymeric synthetic materials are often selected for the ease of processing, their restrained cost and the possibility to control their chemistry, allowing the tailoring of material properties.

However, some interesting polymers still do not possess the adequate stiffness or, more often, when processed in form of highly porous cellular materials, most of the materials lose their intrinsic mechanical properties. The addition of short fibres or particles with different volume to area ratio in a polymer improves the mechanical properties of the original material, producing what is called a composite material. As an example, poly(ethylene-glycolide) hydrogels have been reinforced with natural nanofibers to produce a suitable material for nucleus pulposus replacement⁸⁰. Poly(lactide) materials have been reinforced with different ceramics particles (e.g. hydroxyapatite and β -tricalcium phosphate) for bone graft application to improve foam stiffness^{58,81}. Moreover, bioactive agents as organic glass (e.g. Bioglass[®]) and calcium sulphate demonstrated a beneficial effect on osteochondral healing, improving not only the original mechanical properties of the polymeric matrix, but also the surface and biological properties⁸². The main drawback of composite materials is the difficulty to homogeneously disperse the fillers in the matrix, therefore leading to non-homogeneous properties. Moreover, degradable composite materials require a careful tailoring of the degradation kinetic of the single materials, which might be incompatible in this sense and lead to premature filler migration from the matrix into the body.

2.6 Applications of cellular materials: osteochondral scaffolds

2.6.1 Osteochondral tissue

Biological tissues are known to be hierarchical structures, i.e. possessing multi-scale features (e.g. collagen alignment or different degree of porosity) that enhance the overall properties of the plain tissue. Among these tissues, cartilage has one of the most peculiar structures showing a steep mechanical gradient. This gradient allows a smooth transition from the top surface of the tissue (i.e. the superficial layer) towards the subchondral bone. Articular cartilage is composed of a solid matrix, which primarily consists of proteoglycans (PGs), collagens (mainly type II) and water. PGs create a swelling pressure and are mainly responsible for the compressive stiffness⁸³. Collagens resist the swelling of articular cartilage and strongly determine cartilage tensile properties^{83,84}. Articular cartilage is structurally inhomogeneous and possesses anisotropic and non-linear mechanical properties both in compression and tension^{85–87}. The articular cartilage is a specialized connective tissue covering the extremity of the long bone. Its function is to provide lubrication and facilitate load transmission in articulations, as for knee and fingers. The articular cartilage of the tibia is located on its top portion, while the articular cartilage of the femur is on its end, covering it. It is the articulating portion of the epiphysis that is coated with a layer of hyaline cartilage. Bone is another example of hierarchical tissue. It is composed by an outer dense shell, called cortical bone, enclosing a nucleus of interconnected porous cellular structure, called trabecular bone. As trabeculae grow only along the principal stress axes, this structure allows the tissue to fulfil a load-bearing function minimizing the quantity of material employed, reducing body weight and boosting the biomechanical performances. Articular bone surfaces are covered in a thin layer of articular cartilage, defined as hyaline, which provides a smooth surface and protects the underlying bone from damage. The composition of bone and cartilage takes the name of osteochondral tissue.

The osteochondral tissue shows a steep mechanical gradient from cartilage superficial layer to subchondral bone. A key requirement to design scaffolds for osteochondral tissue engineering is therefore to reproduce such mechanical properties. This result could be achieved by varying scaffold porosity and composition throughout the thickness. Different methods have been applied in literature to produce a cellular structure with a continuous mechanical gradient using synthetic polymers. A common method is to increase the pore size along the longitudinal direction, reducing therefore the stiffness while increasing the permeability and

the porosity. This approach has been investigated for a PCL cylindrical scaffold by centrifugation and thermal fibril bonding⁸⁸. Particulate leaching has been largely applied in this sense, having the possibility to control the pore size by changing the particulate size and concentration⁸⁹. Freeze drying produce promising results, especially in combination with centrifugation to produce radial pores variation in a collagen scaffold^{90,91}. Electrospinning of a micro porous mesh on top of a 3D printed structure has been reported by Puppi et al., producing a dual porous cellular structure⁹². Others proposed methods to continuously control the concentration of a reinforcement material, in form of particles or fibres, through longitudinal axis⁹³.

Nowadays, the introduction of additive manufacturing technologies allows a precise deposition control of different classes of materials into complex 3D geometries. Multi-material scaffold with gradient mechanical properties (e.g. due to porosity and pore size increase/decrease) are easily created by Fused Filament Fabrication, Multijet, Binder Jetting and Biofabrication^{16,94}. However, while virtually any geometrical complexity is not an issue for additive manufacturing and the precision of most of the applied technologies is in the micro-meter scale, the transition through one direction is always discrete and never continuous. This is an intrinsic issue of any layer-by-layer manufacturing method, as properties may only vary among two different layers. Scaling down layers height would help, but only up to the minimum reproducible feature printable by the machine. Also, a discrete gradient is produced as a result of additive manufacturing methods, likeable to incur in delamination issue at the interface between the different materials.

2.6.2 Composition of the osteochondral tissue

Likewise other tissues, articular cartilage is composed of cells called chondrocytes, which are dispersed in a firm gel-like ground substance, the extra cellular matrix (ECM). However, differently from other connective tissues in the body it is fully avascular, lacking of blood vessels. This intrinsic feature of cartilage is the key factor limiting the regeneration potential of the tissue, since cells, nutriments and signalling molecules cannot easily reach the injured site. Moreover, chondrocytes are unable to migrate, being bounded in small niches (lacunae). This scenario leads to the development of stable defects or, more commonly for higher injury grade, to a progressive degeneration of the tissue after serious damages. This observation arose already in 1743, when William Hunter sated, “an ulcerated cartilage is a troublesome problem and once destroyed, it never repairs”⁹⁵. Some cases produce worse scenario with the proceeding of the injury. In the knee joint, where cartilage defects are common due to the high stress due to sport, excessive body weight and accidental falls, untreated injuries can become symptomatic and progressively lead to premature arthritis⁴. Articular cartilage composition is shown in Figure 2.8.

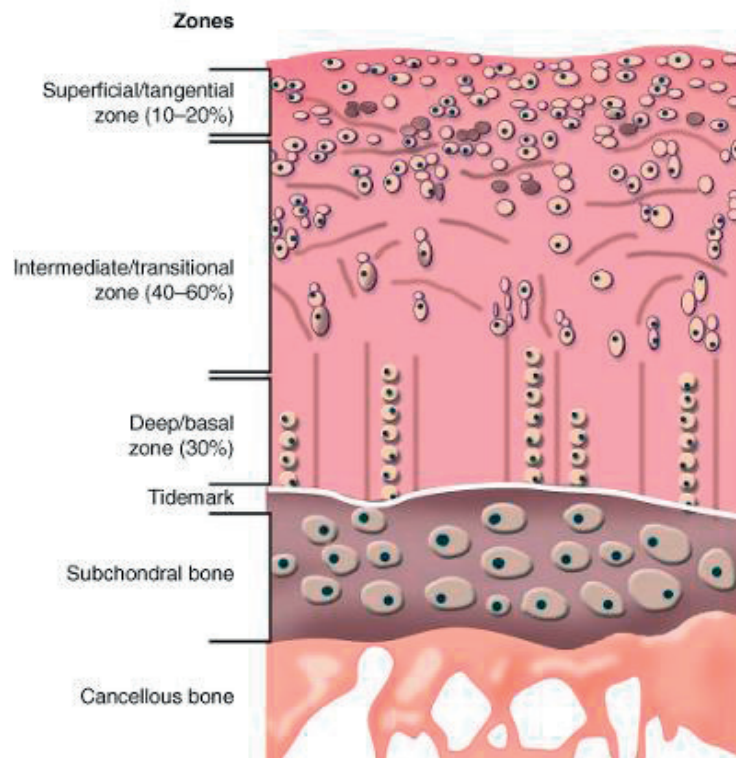


Figure 2.8 Articular cartilage composition and organization at the different layers composing the tissue (adapted from <https://musculoskeletalkey.com>).

Cartilage is found in different spots: the joints, the rib cage, the ear, the nose, the throat and between intervertebral disks. Therefore, the tissue evolved to adapt to specific local needs (e.g. stiffness, lubrication, load bearing), differentiating into three different classes: hyaline, elastic, and fibrocartilage.

2.6.3 Osteochondral defects

Cartilage repair is a challenging clinical problem because once damaged in adults, it never regenerates. The resulting defects may further lead to osteoarthritis OA⁹⁶. OA affects about 10% of the US population older than 30. By age 40 years, 90% of the population harbors degenerative changes in their weight-bearing joints, ultimately leading to pain and immobility⁹⁷. OA affects more people than any other joint syndrome does with direct costs estimated at 60 billion dollars a year in the U.S. as result of 20 million disabled citizens⁶. The result of this disease is the destruction of cartilage matrix leading to a progressive loss in joint function and pain.

Cartilage lesions can be divided into partial thickness defects which do not penetrate the subchondral bone and do not repair spontaneously, and full thickness defects which do penetrate subchondral bone have a partial repair potential, depending on the size and locations of the defect ⁹⁸ (Figure 2.9Figure 2.9).

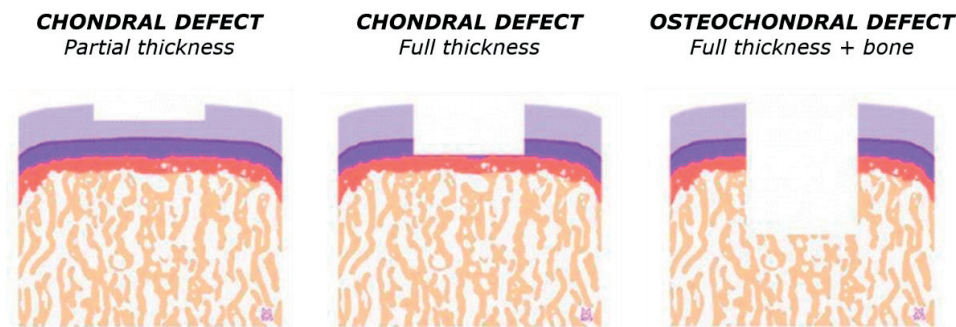


Figure 2.9 Osteochondral and chondral cartilage defects⁹⁹

Subchondral bone disruption produce blood leaking into the defects, leading thus to mesenchymal cells recruiting from the bone. This includes also growth factors and cytokines, which are known to be important signalling molecules for cells differentiation and proliferation^{100,101}. However, the repair response typically leads to the formation of fibrocartilage as neo-cartilage, which possess inferior mechanical properties compare with articular cartilage. Fibrocartilage fails to withstand the stresses of normal joint function and after long-term follow-up, degeneration of both repaired and adjacent native tissues is observed^{5,102}.

OA and joint injuries are significantly correlated. Knee joint injuries were 7.4 times as likely to induce knee OA more than to those individuals who did not have a history of knee injury¹⁰³. This observation is also true for hand joints, which however have a lower frequency due to different loads across joint life. Repair of articular cartilage is then a crucial goal in case of injuries of defects, which otherwise may produce serious degenerative effects on the joint and on life quality.

2.6.4 Osteochondral tissue engineering

Tissue engineering is a multidisciplinary field that joins developments in cell/molecular biology, materials science and engineering, chemistry and medical science towards the development of hybrid substitute combining biodegradable scaffold, cells and signalling molecules such as growth factors aimed at restoring tissue or organs functions⁵. Tissue engineering has the potential to be used in the regeneration of organs or tissues such as articular cartilage and is considered as a potential osteoarthritis treatment strategy superior to the current surgical techniques^{4-6,104}. This is due to limited results of conventional surgery procedure in the long term⁸ and the symptomatic approach, which lead thus a chronic or periodic treatment. Thus, the aim of cartilage tissue engineering is to promote long-lasting, functional repair of defective articular cartilage lesions through the development and ex vivo manufacture of implantable artificial cartilage tissue substitutes⁹.

Conventional tissue engineering is based on three principal elements: (i) scaffolds, (ii) cells and (iii) bioactive molecules such as growth factors or proteins. These three elements combined are placed in a biological environment to produce engineered tissue in vitro or tissue regeneration in vivo (Figure 2.10). These three elements are interdependent and thus the best strategy is to take in account the specific requirement of each element in the development⁶.

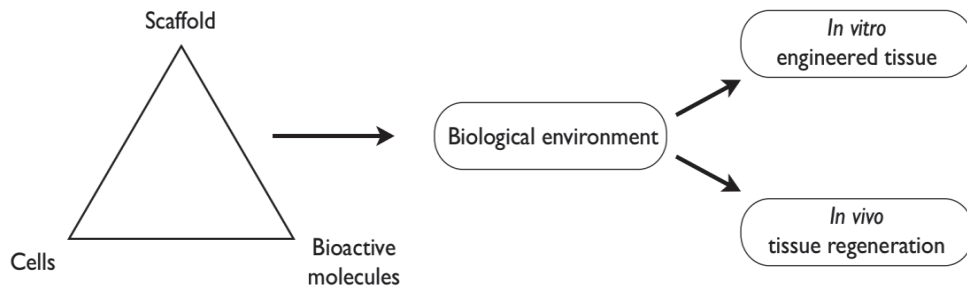


Figure 2.10 The three conventional tissue engineering principal elements^{6,39}.

The role of the scaffold is to provide an artificial matrix that mimic and recreate the structural organization and functionality of the native cartilage and bone structure. The bioactive molecules will act on the cells to promote a desired tissue such as hyaline cartilage rather than fibrocartilage in cartilage tissue engineering.

Tissue engineering approaches may also exclude the presence of a scaffold and are called “scaffold-free”¹⁰⁵. In this technique, cells and bioactive molecules are mixed and injected in the defected area, together with a carrier material. The general idea is to overcome scaffold-seeding procedure, which still shows limitation in cells diffusion and proliferation towards scaffold bulk⁵⁶. However, a limitation in this case is the difficulty to keep cells in place: in most of the cases, cells, migrates towards the tissue instead of proliferating and depositing ECM, leaving to the reformation of a gap region⁵⁶. Lately, the technique has been proposed as an alternative for cartilage regeneration to overcome concerns about long-term scaffold safety. Shimomura et. al⁵⁶ proposed a scaffold-free 3D tissue-engineered construct (TEC) composed of MSCs derived from the synovium and ECMs synthesized by the cells¹⁰. These TECs are developed without an artificial scaffold, and, thus prevent from chemical or biological contamination. Also, they demonstrated to enhance cartilage repair in large animal models^{10,106}.

2.6.5 Requirements for osteochondral tissue engineering

Scaffold for osteochondral tissue engineering operates as load-bearing structures that mimic tissue ECM to ensure the best match possible between surrounding natural tissue and cells seeded within the scaffold, promoting neo-tissue formation^{8,107}. Scaffolds fabricated from biocompatible materials should not elicit immunological or foreign body reactions. Furthermore, scaffolds have to be chosen to be degraded and be resorbed at a controlled rate at the same time as cells seeded into the 3D construct attach, spread and proliferate, e.g. forming new tissue¹⁰⁸. Osteochondral scaffolds should have suitable surface chemistry and topography for cell attachment, proliferation and differentiation, and the mechanical properties of osteochondral scaffolds must be tailored to match those of the host tissues at the site of implantation.

The critical requirements of cartilage tissue engineering are (i) material selection, (ii) scaffold design (porosity: porosity content, pore size distribution and interconnectivity), (iii) the choice of the adequate cell source and (iv) bioactivity (e.g. choice of best growth factors and delivery methods). MultiMaterial scaffolds require interface control between the different materials to avoid delamination. Moreover, properties should change gradually to ensure a smooth transition from soft to strong modulus⁵.

For Ahsan et al.¹⁰⁹ the complete repair of cartilage defects requires two processes in general, namely (i) the integration of the repair tissue with the surrounding host articular cartilage and (ii) the filling of the bulk of

the cartilage defect with tissue that is characteristic of normal articular cartilage. In many cases, the repair fails due to a poor integration of the implant with the host tissue. Interface body/scaffold is a crucial concept in cartilage tissue engineering, because it could represent one of the key of success of the implant. It has been demonstrated that osteochondral plugs induce a layer of necrosis around the defect, leading thus to the impossibility for cells to migrate towards the scaffold, causing then a failure. Some solutions suggest the application of enzymes to relax the collagen fibre mesh around the defect, disrupting part of the ECM and allowing then cells to flow again through the interface ¹¹⁰. Finally, often repaired tissue is closer to fibrocartilage, which has poor mechanical properties compare to the healthy articular cartilage. This drawback is due to a lack of understanding on cells differentiation and mechanical stimuli, which are fundamental for chondrocytes to deposit the correct composition of ECM.

2.6.6 Scaffold design for osteochondral tissue engineering

In tissue engineering, a scaffold is defined as a structure able to guide cells migration, differentiation and proliferation into a desired cell type, layering a new extracellular matrix (ECM) that will eventually entirely substitute the existing scaffold. Therefore, an ideal scaffold is a biodegradable material, which degradation kinetic should match the ECM produced. On top of that, it would be preferred to select a material which degradation products positively interact with the surrounding tissue when released, e.g. acting as a catalyst to enhance ECM deposition or nourishing the cells population. The macrostructure mechanics of a scaffold is therefore the dynamic equilibrium between material degradation and matrix deposition.

Cellular geometries are often required to design 3D scaffolds for tissue engineering, allowing metabolites diffusion, waste transport and cells migration, all essential processes to enhance ECM development. Fundamental parameters to control are therefore pore size and pore morphology. Open porosity and full interconnectivity among the different pores are required in tissue engineering application to allow cells to colonize the maximum surface of the scaffold, allow blood vessel ingrowth (e.g. for bone repair) and allow interstitial fluids to freely flow in and out the structure (e.g. for cartilage repair). Mechanical properties are deeply influenced by the chosen degree of porosity and type of porosity: a highly porous scaffold will show inferior mechanical properties compared to a bulk structure, as a highly porous scaffold with 100% open porosity will perform worse than a 100% closed porosity scaffold with the same degree of porosity. Finally, it has been demonstrated that cells differentiation and proliferation could be directed by changing pores dimension, i.e. modifying stress and strain distribution experienced by the cells in the volume. As an example, Guo et al ¹¹¹ suggest that the target pore size in scaffold for cartilage tissue regeneration should be less than that for bone repair.

The design of osteochondral scaffold is therefore a complex task, which require a good planning in terms of materials and geometries to allow the regeneration of two different tissue, cartilage and bone, with two different cells population, function and mechanical properties.

Single material scaffold

Single material scaffolds are the most straightforward compromise for osteochondral tissue engineering. This solution has been adopted since the very firsts attempt to induce osteochondral regeneration, using one or multiple different methods to process the desired scaffold ^{112,113}. The strategy is to design the desired scaffold and seed osteochondroprogenitor cells or chondrocytes (e.g. the prominent cells population in cartilage) on top of that. The main advantage is indeed the simplicity of the approach, which happens to be also the main

limitation. Cells react differently if exposed to different chemical, physical and biological stimuli. A single material scaffold rarely possesses the property to show different surface properties throughout the thickness. This limitation translates to the impossibility to precisely control cells differentiation into different cell types when the scaffold is seeded with osteochondroprogenitor cells or avoid dedifferentiation of chondrocytes. As specific cells deposit specific ECM, this prevents the possibility to regenerate correctly the required subchondral bone.

Multi-material scaffold

In order to offer different surface chemistry and local mechanical stimuli to induce different cells proliferation and differentiation, alternative solution comprehending two or more materials have been proposed. As an example, two materials shall be coupled in a single structure to provide adequate support to cartilage and bone regeneration. Such a structure would therefore be seeded with two cells type: chondrocytes on top and osteoblast on bottom. The bone-side layer should possess a higher stiffness compared to the cartilage-side, along with the presence of ceramic-like particles for osteoconduction and osteoinduction. The cartilage side requires smaller pores, but also a lower stiffness and an adequate permeability to allow a proper flow of metabolites. This latter point is particularly important in cartilage, given the absence of blood vessels to supply nutrients to the cell population.

The main disadvantage of this approach is the difficulty of manufacturing: current processing methods rarely involve the use of multi-materials and if so, delamination of the two materials is often the main cause of failure. A strategy could be: (i) design two different scaffolds (ii) seed two different cells population in the scaffolds and (iii) joint the two scaffolds before implementing the *in vivo* application. However, delamination might still occur and having to deal with cells-loaded scaffolds and the addition of further different steps could compromise basic requirements. Moreover, delamination induced by sterilization prior the cells seeding (e.g. by heat sterilization in autoclave) might trigger interface degradation between the materials.

A smart solution could be to seed chondrogenic progenitor cells and to design a bioreactor (e.g. a device able to reproduce the desired chemical, mechanical and electrical stimuli to induce cells differentiation into the desired cell type) to stimulate differently the top-side and the bottom-side of the scaffold, inducing cells differentiation and proliferation. An exemplification of the different approaches is shown in Figure 2.11

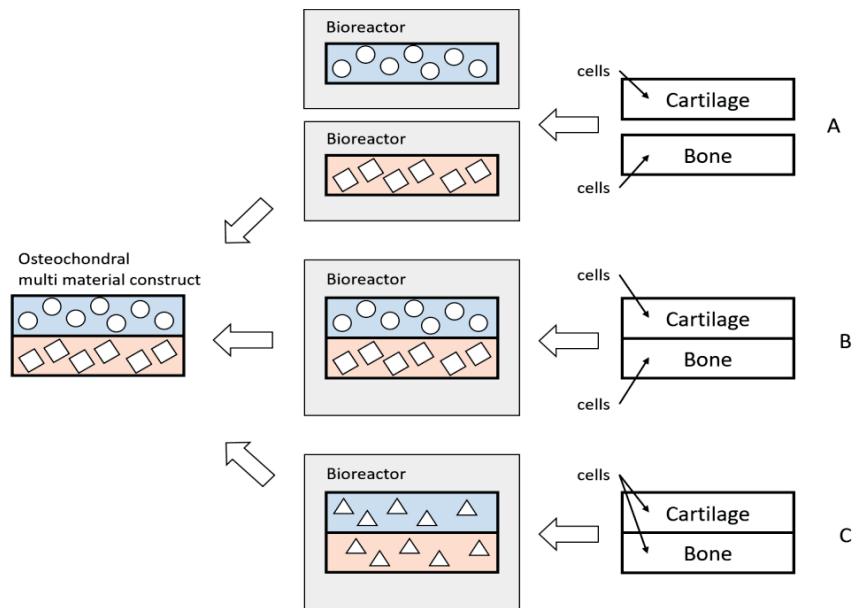


Figure 2.11 Different material can be seeded (i) with two different cells type and joint afterwards (ii) with two different cells type after being joint and (iii) with the same cells type and use a bioreactor to induce a different differentiation⁶⁰.

2.6.7 Mechanical properties of the osteochondral tissue

Looking at cartilage with an engineering frameset, it could be approximated to a fibre reinforced composite material. It provides a bearing surface with low friction, distributing the loads applied to the articulation. Osteoarthritis (OA) arise as a consequence of the loss of such mechanical behaviour of the articular cartilage. This represent one of the first reason why in order to develop a solution to target OA, the mechanics of the tissue should be well understood and reproduced as closed as possible. Different works investigated the zonal mechanical properties of cartilage by mean of optical and acoustic methods, giving insights into the differences that occur between healthy and ill tissues. The biomechanical response of articular cartilage to in vitro compressive loading conditions has been described for indentation^{114–116}, confined compression^{87,116,117}, and most recently unconfined compression^{118–121}. In particular, Poisson's ratio, stiffness and energy dissipation^{4,122,123} and Young modulus¹²⁴ have been object of investigation, even though mostly related to the overall tissue. Viscoelasticity measures have been related to the bulk tissue, mostly relying to theoretical models.

Articular cartilage properties arise from two factors: its multi material composition and the equilibrium between living cells and extracellular matrix composing the tissue. In particular, cartilage extracellular matrix composition and organization are extremely important to understand the tissue mechanics. The most common coefficients used to describe the cartilage properties are the Young's modulus E , the compressive aggregate modulus H_a , the shear modulus G and the Poisson's ratio ν . In this work, we will focus on the compressive response of the articular cartilage, extrapolating the Young's modulus and the aggregate modulus (Table 2).

Table 2 Summary of the mechanical properties measure for articular cartilage in different animal models and harvesting zones.

Coefficient	Estimated value in literature	Reference
Tensile Young's modulus E_t	1-30 MPa	84,125,126
Compressive modulus E	0.01 to 10MPa	127–129
Shear modulus G	0.13 MPa	130,131
Poisson's ration ν	0.1 to 0.4	132–134
Aggregate modulus H_a	0.08 to 2.1 MPa	86,135,136
Permeability k	$1 \times 10^{-15} \text{ m}^4/\text{N}$ (condyle)	137,138
Average thickness (humans)	2.3 mm (condyle), 3.5 mm	139–141

Different studies have been trying to highlight the articular cartilage compressive properties under, carrying out test in confined and unconfined conditions by bulk compression and indentation^{142–144}. The compressive Young's modulus is extracted from the linear region of the stress-strain curve of the tissue under different testing conditions (e.g. compression speed, hydration, etc.), while the aggregate modulus is measured at equilibrium, when the liquid phase has ceased flowing through the material. The compressive properties are mostly influenced by water and proteoglycans content and distribution¹⁴⁵. Proteoglycans influence is explained with the strong repulsive forces developed between groups of proteoglycans in absence of water, which forces the tissue to oppose resistance to the deformation. The aggregate modulus correlates positively with the water content and negatively with the proteoglycans content. Collagen content influence is negligible, influence little to none the compressive stiffness.

2.6.8 Measurements of the articular cartilage local stiffness

The access to study the influence of the different layers in the osteochondral cartilage on the overall tissue behaviour has been limited to technical difficulties, which did not allow investigating precisely the local properties. Donor kind and age and the harvesting site affect the quality of the cartilage, inducing therefore a change. To access to local properties of the different layers, it should be ideally possible to differentiate a point of discontinuity between the different cartilage zones and then apply a method sensitive enough to probe the area of interest. However, as demonstrated for the Young Modulus, a precise model of scaffold able to reproduce the cartilage tissue needs to mimic the dynamic behaviour of the tissue, including the relaxation and creep responses. One of the main reasons why this is particularly important compared to other tissues is the peculiar mechanism adopted by the cartilage to collect nutriment from the surroundings, which relies on the fluid flow through the thickness. Therefore, a new protocol to measure human articular cartilage gradient stiffening by nano indentation was determined in this work. The following results were obtained in collaboration with Jens Antons from the Laboratory of Biomechanical Orthopedics (LBO) at the EPFL and Jiri Nohava from Anton Paar (Peseux, Switzerland). The author contribution was related to the implementation of the testing protocol and mechanical measurements.

Indentation tests were performed by an ad-hoc instrumental indenter developed to measure the mechanical properties of soft materials (Bioindenter™ from Anton Paar, Peseux, Switzerland). Samples were harvested

from six different human donors. The average value was calculated on the base of four out of six indentation lines on six different donors, e.g. excluding donor 1 and 3, with as average $n = 3$ measures per spot. The first indentation was performed 100 μm from the superficial zone towards the bone as indicated in Figure 2.12. Each consecutive indentation was performed at a distance of 100 μm from the previous. Subsequently, 11-40 indentations spaced by 100 μm was performed on cross-sectioned cartilage towards the bone. Each set of measurements from superficial zone to subchondral bone takes the name of indentation line. Three parallel indentation lines with a gap of 800 μm were measured.

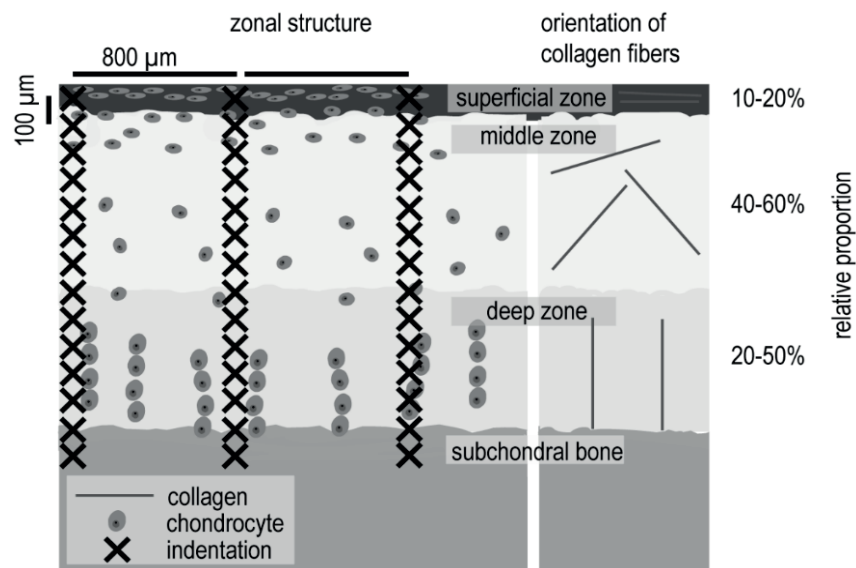


Figure 2.12 Schematic of cell organization (left) and collagen fibres orientation in the extracellular matrix (right) from superficial layer (top layer) through the subchondral bone. An exemplification of the indentation sites is shown through the thickness (X mark)

All of the indentations showed a constant increase of Young's modulus from the top surface of the sample (e.g. superficial layer) to the bottom (e.g. bone). The range of values increases from a minimum of 0.02 ± 0.003 MPa at the superficial layer to a maximum of 6.44 ± 1.02 MPa at the subchondral bone. In Figure 2.13 Depth-dependent Young's modulus of human femoral condyle cartilage. The relative depth corresponds to the distance between the superficial layer (0 %) and subchondral bone (100 %) and was normalized for each sample; $n=3$; standard deviation shown for each sample separately on the right. Figure 2.13 is it possible to appreciate the gradual increase of the tissue Young's modulus compared to the relative depth, meant as the distance between the cartilage superficial layer and the subchondral bone.

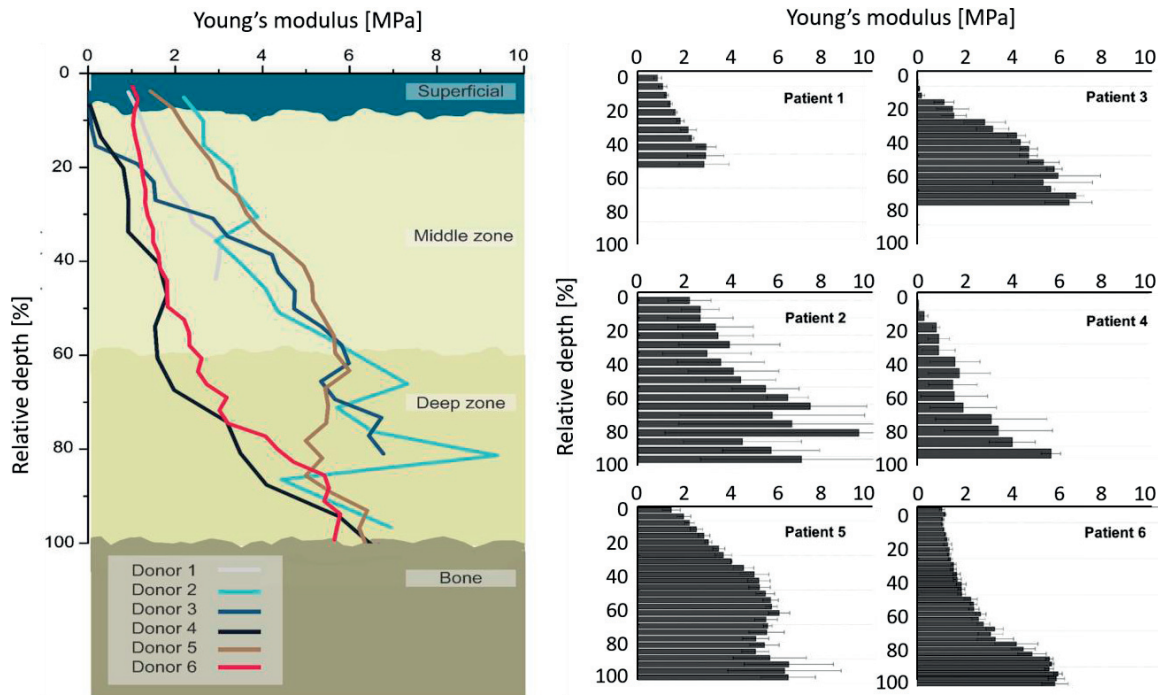


Figure 2.13 Depth-dependent Young's modulus of human femoral condyle cartilage. The relative depth corresponds to the distance between the superficial layer (0 %) and subchondral bone (100 %) and was normalized for each sample; $n=3$; standard deviation shown for each sample separately on the right.

These results well compared to previous works from Chen et al.^{129,146}, where zonal properties were extrapolated from bulk compression measurements. In this study, a constant increasing gradient from the superficial layer to the subchondral bone was highlighted as well. Moreover, even though their measurements were performed on the cartilage femoral head, the range of Young's modulus was comparable to our results. They reported an equilibrium confined compression modulus between 1.16 ± 0.20 MPa in the cartilage superficial layer to 7.75 ± 1.45 MPa in the deep layer while we measured between 0.020 ± 0.003 MPa and 6.44 ± 1.02 MPa from cartilage superficial zone towards the subchondral bone by nanoindentation. The main difference discriminating our approach compared to Chen et al. was the side of indentation: while in our study we performed indentation lines from the cross-section of the tissue (e.g. side to side), the latter mentioned study lead all the analysis from the transversal section (e.g. top to bottom). Our hypothesis is that it would be possible to relate the two measurements between them. As a matter of fact, previous studies discovered that measuring local mechanical properties by atomic force microscopy from the cross-section or the top of porcine articular cartilage samples only made a small difference in Young's modulus (superficial: 20% lower, middle: 14% lower, deep: no difference)¹⁴⁷.

2.7 Conclusions and challenges

In spite of the variety of methods investigated to produce hierarchical polymer cellular structure, none of the presented technologies offer the possibility to create macro and micro porous structures with controlled 3D shape. Many of the most applied methods from the state of the art allow to control the micro porosity within a range from hundreds to few micro meters, as particulate leaching and freeze drying^{27,90,90,148–150}. What they still miss is the possibility to precisely shape the 3D structure, producing complex geometries with a tuneable

macro porosity. On the other hand, additive manufacturing offers the possibility to precisely reproduce a 3D geometry without incurring into the processing limitations of mold-based and subtractive methods. However, the smallest reproducible feature by additive manufacturing methods is defined by technological limitations, as the nozzle diameter in FDM/FFF. This prevents the possibility to design a micro porosity within the 3D structure and limits the structure porosity, often producing geometries with up to 80% porosity. This is particularly crucial in medical applications, where a high degree of porosity to promote cells growth and proliferation is required.

Scaffold-based osteochondral tissue engineering is one field where hierarchical cellular structures find an ideal application. The anisotropic mechanics of this tissue derives from the progressive modification in tissue composition and organization. As previously seen, the local stiffness gradually increases from the superficial cartilage layer to the subchondral bone, creating therefore a mechanical gradient. A lot of effort has been put in research to design the ideal solution to repair osteochondral defects, with many groups actually working on different approaches, materials and technology. However, today no tested solution fits the ideal result of complete tissue regeneration and function recovery in the long period. The notable amount of works produces an intrinsic difficulty to compare all the results, since each solution is tested on different materials, animal models, conditions, cells and anatomic section. A general guideline can be however drawn from the literature analysis:

- Scaffold mechanical properties should match the one of the target tissue (e.g. human articular cartilage and bone). This is obvious from all the implant failure due to poor scaffold integration into the host tissue and the common problem of production of under-performing cartilage due to unnatural mechanical stimulation. The correct approach would require to retrieve the target properties of the tissue and use them to design the desired scaffold.
- Osteochondral implants as opposed to cartilage implant should be preferred, allowing therefore a better integration of the graft within the tissue. The presence of the subchondral bone in the osteochondral implant would guarantee a better fixation in the articulation, both during the surgery and in the first weeks after the implant. The latter is particularly true because of the fastest regeneration occurring in the bone phase of the articulation, as opposed to the slowest of the cartilage tissue. Such a regeneration, also happening within the implant, would help steadily fixing the graft to the tissue.
- Biomaterials with proven biocompatibility, low inflammation promotion and active or low-impact degradation products should be considered for this application. Given the structure of the articular cartilage, hydrogels are appealing materials because of their high hydration state that promotes cells adhesion, proliferation and differentiation. However, they do not possess the mechanical strength to reproduce the tissue mechanics.

To summarize, the ideal scaffold should closely mimic the bio-mechanics of the target osteochondral tissue, providing a smooth transition from the top layer of the articular cartilage to the subchondral bone. It should be tailored to describe mechanical properties differences across the thickness as the natural tissue, to induce a mechanical stimulation dependent on tissue thickness. Discrete regions of the scaffold are optimized for selective growth of the desired tissue by utilizing different material types, material properties, internal architectures (such as the porosity and the pore interconnectivity), cells and biological factors. It should be composed by at least two different materials seeded with different cell types, one for the articular cartilage

and one for the bone. Finally, it should be composed of degradable materials, possibly tuned or easily tuneable to optimize the different degradation kinetics to ECM deposition in order to guarantee a constant load bearing function over time. The ideal scaffold could be constituted by a multi material polymer structure with a dual degree of porosity to match tissue mechanical properties and the local deformation required to induce cells differentiation and growth. This multi material scaffold could therefore be impregnated with a bioactive hydrogel to promote cells adhesion and seeding.

Additive manufacturing has the great potential to manufacture a complex geometry that would be able to mimic the desired stiffness gradient. Filament Fusion Fabrication (FFF) would represent the best technology in this sense, having a broader range of available materials and having the possibility to combine them into a single geometry. This solution has already been investigated ^{151–153}, showing good results for bone regeneration. A further step would be required to adapt the technology to cartilage application, where a softer material or a more porous geometry would be required to reduce scaffold stiffness and match the mechanical properties shown by the tissue at each constituting layer. Supercritical CO₂, could represent an interesting choice to allow increasing the scaffold porosity by inducing the foaming process to occur within the 3D geometry previously created by FFF. This approach will be investigated in this project to produce hierarchical scaffold with a controlled micro and macro porosity within the range of 2 – 4 mm thickness.

Chapter 3 Materials and Methods

3.1 Materials

Two classes of materials were considered. Natureworks Poly(lactide) was selected as model material to validate extrusion, foaming and characterization methods. The same protocols were then applied to process different medical grade biopolymers. Five materials were processed: a medical Poly-L-lactide (Evonik Resomer L207s), two medical copolymers (Evonik Resomer LC 703s and LG 855s) and two in-house medical blends (Evonik Resomer L 207s/10wt% PEG35000 and L207s/10wt% β -TCP). A resume of selected materials and related properties is shown in Table 3.

Table 3 List of the materials used in this study.

CLASS	SUBCLASS	ABBREVIATION	COMPOSITION	COMPANY / COMMERCIAL NAME	STATE
MODEL	Neat	PLAm1	Poly(lactide)	Natureworks / PLA d2002	Granules / Filament
	Neat	PLAm2	Poly(lactide)	Natureworks / PLA d4043	Granules / Filament
MEDICAL	Commercial Polymer	PLLA	Poly(L-lactide)	Evonik / Resomer L207s	Flakes
	Commercial Copolymer	PLAPCL	Poly(lactide-co- ϵ -caprolactone) Molar ratio 70:30	Evonik / Resomer LC 703s	Flakes
		PLAPGA	Poly(lactide-co-glycolide) Molar ratio 85:15	Evonik / Resomer LG 855s	Flakes
	In-house Blend	PLAPEG	Poly(L-lactide)/10 wt% Poly(ethylene glycol)	Evonik / Resomer L207s Aldrich / PEG Mn 35,000 g/mol	Flakes / Flakes
	In-house Composite	PLABTCP	Poly(L-lactide)/20wt% β TCP	Evonik / Resomer L207s Cambiaceramics	Flakes / Particles

3.1.1 Model materials

Thanks to its good stability, low price and limited shrinkage/warping during the printing process Poly(lactide) (PLA) is one of the most used materials in Fused Filament Fabrication / Fused Deposition Modelling 3D printing. Furthermore, PLA is a degradable biopolymer often applied to create packaging and degradable devices. PLA degradation has been intensively investigated in the past and it can be easily tailored to the desired kinetic and lifetime. Also, the PLA degradation product, the lactide acid, is a native compound in nature and can be processed by physiological cycles.

Two different grades of Poly(lactide) were chosen as model materials: PLAm1, specifically designed for extrusion/thermoforming applications and PLAm2, often used as a reference material for FFF/FDM 3D printing applications.

3.1.2 Medical materials

The first explored medical grade material was a Poly(L-lactide) (PLLA), reported to be an ideal candidate among medical Poly(lactide) for foaming and bone replacement^{39,154}. From the very same polymer, two materials were produced: a polymer/ceramic composite (Poly(L-lactide)/10wt% β -TCP) and a blend Poly(L-lactide-co-ethylene glycole 35k). They will be referred as PLABTCP and PLAPEG.

Poly(ethylene glycole) (PEG) has been widely used as a plasticizing agent to increase flexibility, damping properties, impact resistance, deformation and resilience, all being interesting properties to justify the use of PLAPEG constructs in cartilage repair^{155,156}. PEG (Mn=35'000 g/mol, Aldrich) was used for the blending with PLLA owing to its relatively good stability in human body condition^{39,157} and its glass transition temperature of approximately 34°C (below the normal body temperature) implying the amorphous content to be in the rubbery state *in vivo*³⁹. However, the molar mass of the PEG was limited to values below 40'000 g/mol, higher values being reported to induce problems with PEG excretion from the body¹⁵⁸.

Beta-Tricalcium phosphate (β -TCP) as ceramic particles have been widely used in blended systems for bone tissue engineering^{159,160}. They have been recognized as an attractive biomaterial because of their similar chemical composition to the mineral component of the bone and their osteoinductivity. β -TCP is thus a good candidate to be used in the subchondral bone part of the osteochondral defect to promote osteogenesis¹⁶¹.

Finally, other medical grade copolymers, a Poly(lactide-co-caprolactone) (PLAPCL) and a Poly(lactide-co-glycolide) (PLAPGA) were investigated to enlarge the range of medical grade material suitable for the production of filament for FDM 3D Printers. PLAPCL is a soft thermoplastic material often applied to manufacture vascular devices¹⁶². The presence of Poly(caprolactone) allows higher deformation to the copolymer compared to the pure Poly(lactide), offering an interesting range of mechanical properties in soft tissue engineering application. PLAPGA is a stiff copolymer largely applied in orthopaedics applications, especially to manufacture bone and cartilage grafts¹⁶³.

3.2 Processing methods

PLA polymers are hygroscopic and are thus susceptible to thermal degradation during processing. The water can come from different sources such as inadequate storage and handling that can considerably affect the quality of the end-product. This justified the necessity to dry the polymer before carrying any tests. Absorption of moisture by the polymer feedstock is reported to induce significant problems due to water vaporization during extrusion and foaming processes. Morphological changes in the material, blockages of the print nozzle and/or formation of bubbles and bulges on the surface of the printed road of material have been reported¹⁶⁴.

For that reason, the polymer granules were dried overnight at 80 °C prior to use and then placed in a desiccator to decrease the moisture content and avoid triggering polymer degradation during the extrusion.

3.2.1 Filament extrusion

Firstly, filament extrusion processing window of the model material (PLAm1) was determined using a Noztek Touch extruder, selecting the temperature and motor speed of the extruder to produce 1.75 mm diameter filament without degrading the polymer and remaining in the extruder working limit. The lowest possible temperature above the material melting temperature and motor speed were used and progressively increased until the produced filament met the set requirements (Appendix II).

The same procedure was then applied to the medical grade materials listed in Table 1. In order to find at least two extruding conditions (temperature and motor speed) permitting to produce good quality filaments, 200 g of medical grade PLA was used for each extrusion run.

PLLA, PEG and β -TCP were dried separately at 80 °C (PLLA and β -TCP) and 35 °C (PEG) overnight. Blends of PLAPEG and PLABTCP were produced with weight ratio of 90:10, mixing 20 g of PEG/ β -TCP to 180 g of PLLA. The systems were then hand-mixed for 5 min to ensure homogeneous distribution. Homogeneity of the β -TCP particles were therefore confirmed by SEM and TGA investigations.

3.2.2 FDM /FFF 3D Printing

An Ultimaker Original+ (Ultimaker, Netherlands) (feeding filament (\varnothing 2.85 mm) and Makerbot Replicator 2 (MakerBot Industries, USA) (\varnothing 1.85 mm) were used to melt and deposit the filaments (Figure 3.1). The 3D model was created in Sketchup Student (Google, USA), with this dimensions: heights: 4mm, beams size: 0.5 mm, pore size: 1 mm, cylindrical shape with diameter: 4 mm. Cura (Ultimaker, Netherlands) was used as slicing software to determine the printing properties.

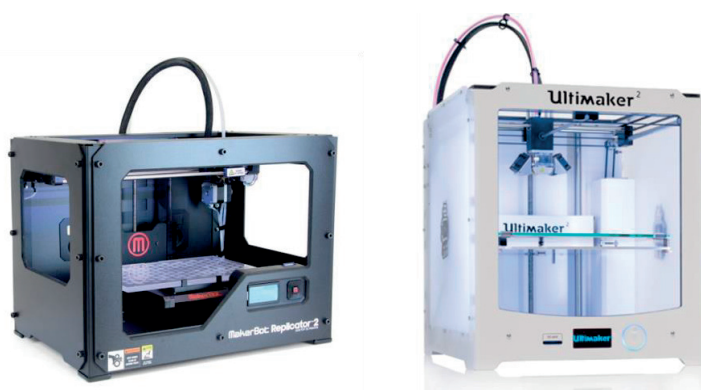


Figure 3.1 A Makerbot Replicator 2 (left) and a Ultimaker 2 (right) were used to print all the 3D structures.

Filament of PLAm1 and PLAm2 were acquired from TreeDFilaments (TreeDFilaments, Italy) and FiloAlpha (FiloAlpha, Italy) as 1.75mm and 3.00 mm. All the filaments were dried and stored in a desiccator prior to printing to ensure a dry state and avoid polymer degradation. For the multi material scaffolds, the printing run was stopped at a building progress of 50 %, permitting to place the second material to finish the second part of the scaffold.

All saturated filaments were extruded by a Markebot Replicator 2, using a set of nozzle size between 0.4 and 1 mm, at extrusion speed from 10 to 100 RPM and hot-end temperature from 180 to 250 °C. All the parameters are monitored by Simplify3D (Simplify3D, USA).

3.2.3 Supercritical CO₂ Foaming

All the processes discussed in the result sections involving supercritical carbon dioxide foaming were performed using a high pressure and high temperature autoclave certified for medical applications (SITEC-Sieber Engineering AG, Switzerland) (Figure 3.2). This GMP medical autoclave operates with maximum pressure and temperature of 300 bars and 300 °C respectively. The pressure chamber is designed in a way to have a spiral heating coil providing homogeneous heat transfer inside of the vessel. Three thermocouples at the top, middle and bottom of the vessel control the processing temperature. Pressure entry is located on the back side of the vessel. To reach high pressure, a CO₂ in liquid state is pumped from a tank into the vessel up to 90 bars at 50 °C. Then, the vessel is isolated and the pressure is controlled by increasing or decreasing the temperature. If the pressure exceeds the set point value while the temperature set point is still not

reached, two valves provide a controlled CO₂ release by an exhausting line. To allow precise monitoring and reproducibility of the experiments, temperature, pressure, depressurization rates and saturation time are programmed before the experiment using EURO THERM software (Eurotherm, Switzerland). A computer monitors the experimental values during the experiments, while data is recorded as function of time for further analysis.

The main parameters that were studied in this work were the saturation temperature T_{sat} , the saturation pressure P_{sat} , the saturation time t_{sat} and the depressurization rate dP/dt . All the samples were positioned on a support cylindrical mold. The mold dimensions were 10 cm diameter by 4 cm height. The typical foaming cycle started with a ramping phase at 90 bars and 50 °C, followed by the reaching of the set point values investigated.



Figure 3.2 EPFL high pressure high temperature autoclave designed by SITEC-Sieber Engineering AG. The autoclave is divided in different working areas separated by lateral windows. The whole process, from material weight to post processing happens under a ventilated hood.

3.3 Characterization methods

3.3.1 Dynamic Calorimetric Scanning (DSC)

A thermal analysis differential scanning calorimeter (TA Instrument, DSC Q100) was used to analyse the thermal transition temperatures and enthalpy changes of the samples during melting. The crystallinity fraction at the stage of raw pellets (before extrusion), melt-extruded filament (after extrusion) and printed scaffold were determined. For each measurement, approximately 5-10 mg of material was used. The scanning conditions were 0 to 220 °C (1st heating), 220 to 0 °C (1st cooling) and 0 to 220 °C (2nd heating) at a rate of 10 °C/min under nitrogenous atmosphere 50ml/min, with an isothermal step of 1 minute between the scans. Measured parameters consisted of glass transition temperature T_g , melting temperature T_m , crystallization temperature T_c .

The degree of crystallinity λ_c [%] was calculated using (eq.6) ¹⁶⁵:

$$\lambda_c = \left(\frac{\Delta H_m - \Delta H_c}{\Delta H_m^0 (1 - W_{add})} \times 100 \right) \quad eq (6)$$

where

ΔH_m [J/g] melt crystallization enthalpy

ΔH_c [J/g] cold crystallization enthalpy

ΔH_m^0 [J/g] corresponds to the theoretical value of the heat of fusion for a 100% crystalline analogue material, taken to be $\Delta H_m^0 = 93$ J/g for 100% crystalline PLLA, as reported by ¹⁶⁶.

For blended systems, W_{add} corresponds to the weight fraction of the added element to the main material. In case of pure systems, $W_{add} = 0$.

Since the previous thermal history of the PLA granules is unknown and considerably affects the measured degree of crystallinity, the granules were evaluated as received and after being subjected to an annealing cycle designed to impart the thermal history. Consequently, the degree of crystallinity of the granules was calculated from the 2nd heating cycle, the 1st heating cycle permitting to remove the thermal history of the material. For the filaments/ scaffolds, the degree of crystallinity was calculated from the 1st heating cycle to see directly the influence of the extrusion/3D Printing process respectively on the change in the degree of crystallinity.

3.3.2 Thermogravimetric Analysis (TGA)

During processing and especially during the extrusion process, the material is exposed for few minutes (residence time) to a constant high temperature before being extruded. In order to verify that no degradation is occurring under typical extrusion/3D printing temperature and material residence time, isothermal tests were carried out respectively on the granules, filaments and scaffolds to investigate the thermal degradation in time. The temperature at which the thermal degradation starts T_D and the degradation rate r_D , were determined for

- temperature ramp from 30 °C to 500 °C at 20 °C/min, air atmosphere 20.0 ml/min was applied. This test permits to determine T_D and r_D , and to study the influence of the extrusion and printing parameters. The scanned conditions were an isotherm at 30.00°C for 1 min, heating from 30 °C to 500 °C at 20.00 °C/min, isotherm at 500 °C for 5 min
- isotherm at 220 °C during 10 min under air atmosphere (20 ml/min) was imposed to the material

3.3.3 Foam density and porosity

The material expansion rate was evaluated using an apparent density ρ^* determined by weighing a sample of known volume. This method was applied to estimate foam density and porosity of homothetic and 3D foam printed structures. From this value, sample porosity ϵ^* is calculated using eq. 7 ²¹.

$$\epsilon^* = 100 \times \left(1 - \frac{\rho^*}{\rho_s} \right) \quad eq (7)$$

Where ρ^* is the density of the foamed structure and ρ_s is the density of the solid material. For Poly(lactide) (PLAm1, PLAm2) $\rho_s = 1.245 \text{ g/cm}^3$, Poly(lactide-co-caprolactone) (PLAPCL) $\rho_s = 1.215 \text{ g/cm}^3$ and for Poly(lactide- β TCP) (PLABTCP) $\rho_s = 1.240 \text{ g/cm}^3$. Each porosity value expresses the mean value on a set of $n = 3$ measurements. The mass was acquired by mean of a precision scale to the second significant digit.

3.3.4 Compression behaviour of 3D printed structures and foams

The compression tests in air were performed in air medium using a traction-compression testing machine (UTS, TestSysteme, Germany), equipped with a loadcell of 1 kN. The setup is shown in Figure 3.3.

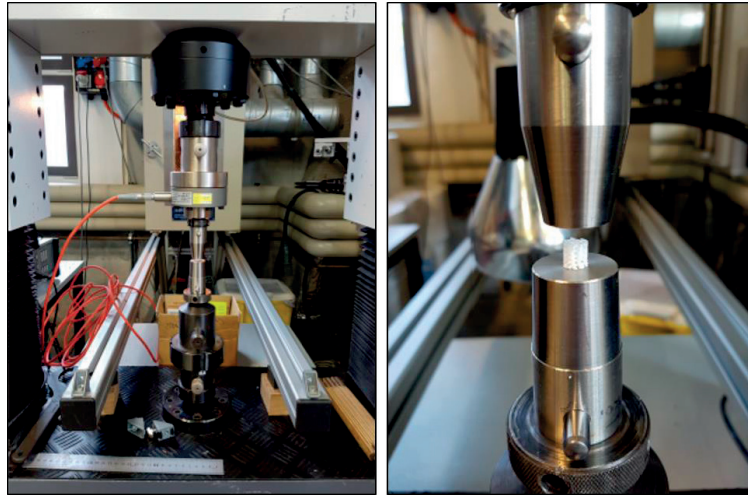


Figure 3.3 Image of the UTS machine (left) and the setup for compression mechanical testing in air (right).

Cylindrical specimens of 8 mm x 4 mm were extracted from the samples and compressed to a 60 % deformation with a cross-head speed of 0.5 mm/min, as shown in Figure 3.4. The compressive modulus E was extracted from the linear elastic region of the stress-strain curve. For each specimen, $n = 3$ samples were measured.

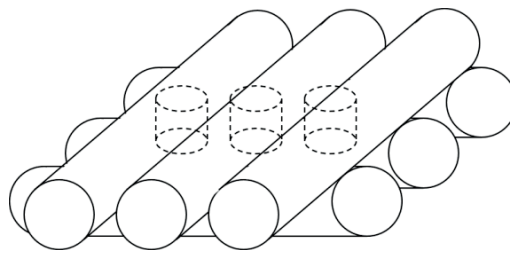


Figure 3.4 Cylindrical samples of 8 mm diameter x 4 mm height extracted from the samples for the compression tests.

The compression tests in phosphate-buffered saline solution (PBS) were performed using an Electropuls Dynamic Test System (Instron E1000) in displacement control at 0.5 mm/min up to 60 % deformation. Cylindrical specimens of 8 mm x 4 mm were extracted from the samples and was saturated in PBS at ambient temperature for 2 h prior the measurements. The compressive modulus E was extracted from the linear region of the stress-strain curve. For each specimen, $n = 3$ samples were measured.

3.3.5 Fracture mechanics

Compact tension (CT) samples are designed to test the fracture toughness of a material under a given geometry. Fracture is commonly understood as the state at which a material breaks after irreversible catastrophic crack advance, despite the fact that stable growth mechanisms exist such as sub-critical crack growth. Different approaches to fracture analysis exist, mainly differing on the assumptions made for the material's properties. A stress intensity factor K_q is used for quantitative analysis because of its direct deduction from sample properties and test results. It completely describes the stress field close to the crack tip.

Poly(lactide) is considered here as an elastoplastic solid since mathematical analysis of ideally elastic samples predicts an infinite stress state at the crack tip. The stress leading to the solid's fracture is significantly smaller than the one to plastically deform the whole sample, excluding the case of a completely ductile material. The model for this test is designed to study PLA samples under small-scale yielding, a necessary condition for meaningful K_q measurements and displaying plastic behaviour in the crack tip vicinity.

Mode I testing was chosen to determine the fracture toughness of two continuous layers in 3D printed specimen. Mode I (or opening mode) corresponds to the most common mode as most fracture occurs by this dynamic. In this mode the load is applied perpendicular to the crack plane. Simple calculations of K_q are performed with the formula below

$$K_q = Y \cdot \sigma \cdot (\pi \cdot a)^{\frac{1}{2}} \quad eq (8)$$

where

$Y [-]$: geometrical factor

$\sigma [Pa]$: stress at rupture

$a [m]$: crack length

When applied to the specific geometry selected for the test, the equation can be expressed as:

$$K_Q = \frac{P}{B \cdot W^{\frac{1}{2}}} \cdot f\left(\frac{a}{W}\right) \quad eq (9)$$

where

$$f\left(\frac{a}{w}\right) = \sqrt{\pi} \cdot \left(16.7 \cdot \left(\frac{a}{w}\right)^{\frac{1}{2}} - \dots\right) \text{ only the first term in the series solution is conserved}$$

$P [N]$: maximum load

$B [m]$: sample thickness

$W [m]$: sample relative width

$a [m]$: crack length

The production by 3D printing of compact tension specimen followed the ISO 13586:2010 (Plastics -- Determination of fracture toughness (G_{IC} and K_{IC}) - Linear elastic fracture mechanics (LEFM) approach) to study the fracture toughness at the interface between two different deposited layers.

The specimen design is shown in Figure 3.5. The dimensions of the samples were B (thickness) = 3.00 mm, W (length) = 5.04 mm and a (initial crack length) = 1.42 mm. The dimension constraints were dictated by the cartilage-bone interface size, long print times and the material cost. The standard notch present in CT samples was directly incorporated within the geometry to reduce result deviations due to human imprecision (depth and orientation). All the specimens were fissured at the designed interface by a medical scalpel (0.4 mm thickness) to accentuate the pre-existing notch. For each test condition, $n = 3$ specimens were tested.

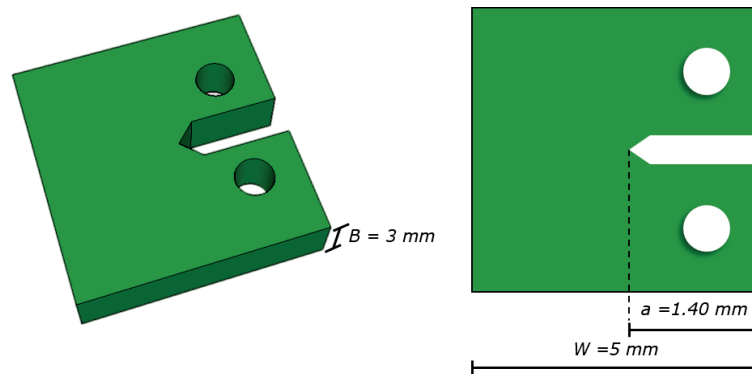


Figure 3.5 Compact Tension 3D printed specimen used for fracture toughness measurements.

The mechanical testing is performed by mean of a traction machine (Minimat™) equipped with a force cell of 1 kN. The setup for the CT test is shown in Figure 3.6.

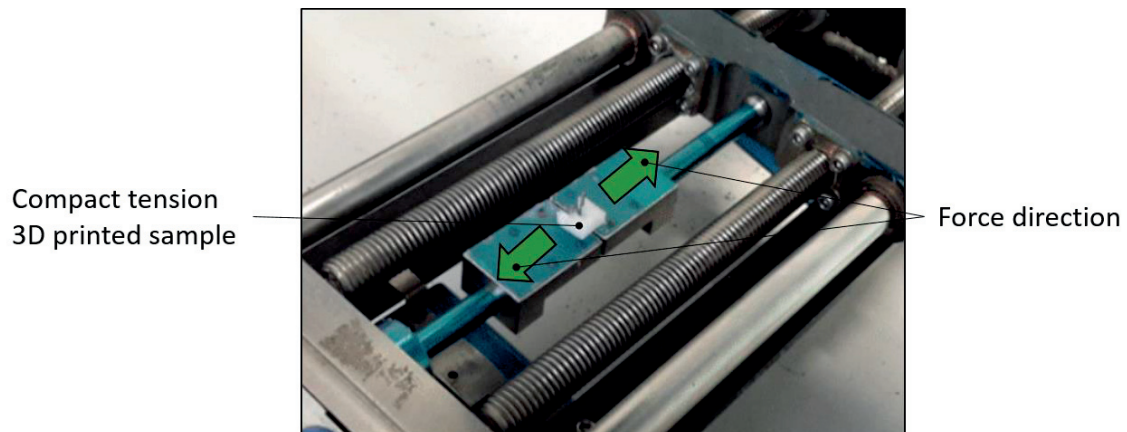


Figure 3.6 Illustration of the CT set up mode I testing on 3D printed specimen.

Chapter 4 Homothetic Foaming of 3D Printed Structures

4.1 Introduction

Cellular structures of PLA have been produced by different methods for applications as packaging, tissue engineering and insulation panels ¹⁻³. The pore morphology in such structures is especially relevant in medical applications, where the pore size and pore distribution influence the performance of the final product ⁴⁻⁶. A widely investigated method to process PLA into controlled cellular structures is by supercritical carbon dioxide foaming (ScCO₂). PLA foams produced by ScCO₂ shows a wide range of properties depending on the racemic mixture of L- and D- lactide that influences the crystallinity of the material ⁷. In average, high porosity, up to 93 % ², and a range of pore size from 0.02 to 0.1 mm are shown by these structures ^{8,9}, with an elastic modulus ranging from 6 to 70 MPa ¹. ScCO₂ is an excellent method to process biopolymers, due to the total absence of solvents during the process. However, major limitations shown by such PLA foams is the limited percentage of interconnectivity between the pores ¹⁰, the presence of an impermeable layer of material (called "skin") on the outer edge of the structure ¹¹ and the presence of an uncontrolled porosity gradient within the structure ¹². Fused Deposition Modelling / Fused Filament Fabrication (FDM/FFF), solvent-free as well as ScCO₂, solves these issues. It provides a manufacturing method to produce 100 % interconnected porosity, with high permeability and full control on the porosity gradient. PLA is one of the most used polymer in FDM/FFF and cellular structures with a reported range of porosity up to 60 - 80 % ^{13,14} and Young's modulus from 40 to 700 MPa ¹⁵⁻¹⁸ have been previously reported. The main limitation of FDM/FFF is the impossibility to increase the porosity over a certain threshold, given by the minimum strand diameter extruded by the machine. This strand diameter is function of the printer nozzle size, which however cannot be decrease below 0.1 mm without scarifying too much processing speed and print quality.

This chapter will discuss how to combine ScCO₂ with FDM/FFF, producing PLA cellular structures with all the advantages of the two techniques. This new process will involve two steps: the 3D printing of a cellular structure with a macro porosity (from 1 to 0.2 mm) and the consequent foaming of this structure to add a micro porosity (from 0.1 to 0.01 mm). At first, the influence of ScCO₂ processing parameters (e.g. saturation temperature, pressure, time and depressurization rate) on the porosity of single PLA granules will be investigated. Then, this knowledge will be applied to 2D and 3D structures, investigating how 3D printed cellular shapes and pore morphology are influenced by the foaming conditions. Finally, the mechanical properties of 3D printed structures with different porosities will be evaluated. Those will be compared with the mechanical properties of the same structure after having been foamed under the conditions defined in the previous investigations. This new process of foaming for expanding in 3 directions a given 3D printed structure take the name of homothetic foaming.

4.2 Materials and methods

4.2.1 Materials

Two Poly(lactide) in granulate form from Natureworks were investigated, as described in Chapter 3 Table 3. These materials were chosen as model materials for the preliminary studies given the well-known foaming processing windows, mechanical properties and availability both as granules and filaments for Fused Deposition Modelling/Fused Filament Fabrication ^{1,19,20}. PLAm1 was used in form of granules and 1.75 mm filament for all the foaming and printing tests, while PLAm2 was applied only in form of 3.00 mm filament in the second part of this study.

PLAm1 and PLAm2 granules and filaments were stored in a desiccator and in a freezer at -30 °C to prevent humidity sorption and ageing. Prior to use, all the polymers were dried under vacuum at 70 °C for 8 h to minimise the water content ^{1,21}.

4.2.2 Foaming processing conditions

Each of the four main processing parameter in supercritical foaming (saturation temperature, pressure, time and depressurization rate) was varied on three different levels (low, medium, high) while keeping the others constant. As the aim of this study is to investigate the set of parameters that allows foaming the granules without totally melting them, the saturation temperature was the first investigated. The medium value was chosen as the PLAm1 reported melting temperature in presence of CO₂ ¹, while the minimum and maximum value were chosen at ± 5 °C from this value.

The foaming conditions for 2D and 3D structures were chosen on the base of the results collected for granules foaming.

4.2.3 3D printing

The setup used to produce all the 3D printed structures is described in Chapter 3.2.2. PLAm1 and PLAm2 samples were printed at 210 °C and 50 mm/s. The slicing of the structure was performed by Simplify 3D®, while all the 3D models were produced using Sketchup Make®.

4.3 Processing cellular structures

The conceptual workflow to produce cellular structure by homothetic foaming is shown in Figure 4.1. A 3D printed template with a macro porosity of 0.3 – 0.5 mm is placed in a high temperature high pressure autoclave vessel. Then, the vessel is saturated with CO₂. Pressure and temperature are increase above the triple point calculate from the CO₂ phase diagram (Figure 2.5Figure 2.5), namely at T = 50 °C and P = 90 bars. Finally, selected processing conditions are applied, creating a micro cellular structure within the bulk 3D printed strands and increasing the overall porosity.

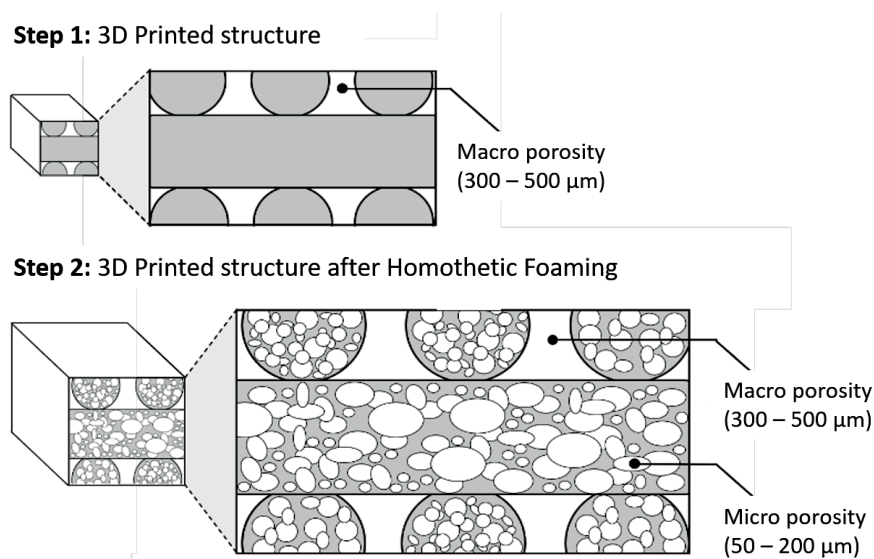


Figure 4.1 Concept of a hierarchical cellular scaffold produced by homothetic foaming of a 3D printed structure.

4.3.1 Partial foaming

In order to assess the idea of partial foaming and demonstrate the feasibility of the homothetic foaming, PLAm1 was selected as testing material. Granules of PLAm1 were tested to determine the influence of the principal foaming parameters (saturation temperature, pressure, time and depressurization rate) on the process.

In the first step, different melting temperatures were investigated in order to keep the 3D structure of an object and produce a partial melting. For 1-dimentional granules, the goal is to allow granules to bond each other, while preserving their spherical structure. From the work of Carole Boissard ¹ on PLAm1 foaming, it has been observed that the material foams completely at 140 °C. Given the reported PLAm1 melting temperature T_m in presence of CO₂ of about 130 °C ²², the desired working temperature was investigated between 135 °C and 125 °C. Gradual steps of 5 °C saturation temperature reduction were considered, at constant saturation pressure (200 bars), saturation time (10 min) and depressurization rate (1 bar/sec) (Table 4).

Table 4 Saturation temperature (left) and relative capability of the material to melt at reference temperature.

	<i>Saturation temperature</i>	<i>Melting</i>
<i>T1</i>	135 °C	Partially molten
<i>T2</i>	130 °C	Partially molten
<i>T3</i>	125 °C	Not molten

A single granule was cut in half before and after the foaming at T1 condition. A self-reinforced structure, constituted by a hard bulk core surrounded by a soft foam shell, is originated from the foaming of the molten surface of the granule. Same results were observed under T2 condition. Figure 4.2 shows the macroscopic morphology of the self-reinforced foam surrounding the core bulk material.

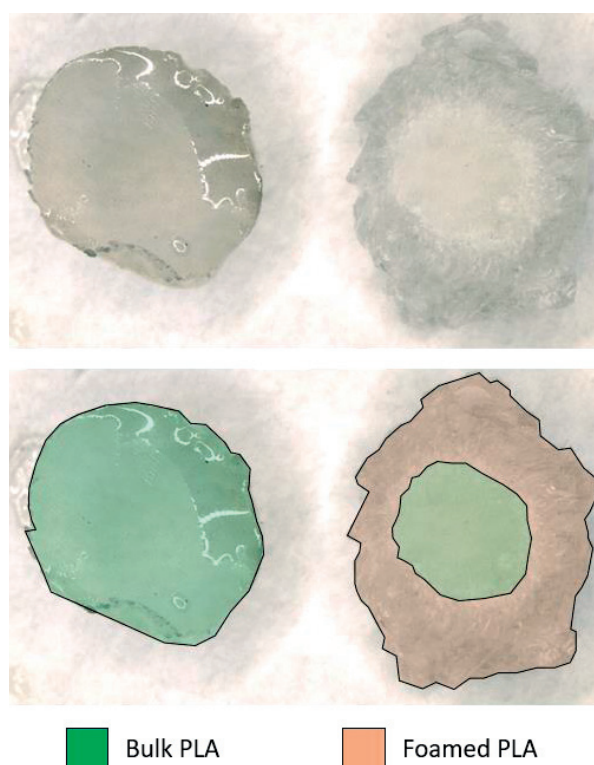


Figure 4.2 Single PLAm1 granule used as template of 3D structure before (left) and after (right) foaming. The bulk PLA granule (green area) expands due to the foaming process, creating a shell of foamed PLA (orange area) around the remaining PLA core.

T1 and T2 were chosen for further analysis with a Scanning Electron Microscopy to investigate pore size and morphology. In Figure 4.3 it is possible to appreciate the impact of a slight change on the saturation temperature during the process. While both show a preserved PLA granule core surrounded by foam, granules morphology and pores distribution change sharply. T1 sample as expected shows a smaller core granule and drastic changes between granule edge porosity and inter-granules porosity. It is interesting to notice the difference between these two pore size: while inter-granules porosity is kept in the standard range of 200 μm -800 μm , granule edge shows a micro porosity in the range of few μm (Figure 4.3). Similar observation comes from T2 sample, which however keeps granule shape and dimension, while introducing in the same fashion a porosity gradient of few μm to hundreds of μm (Figure 4.4).

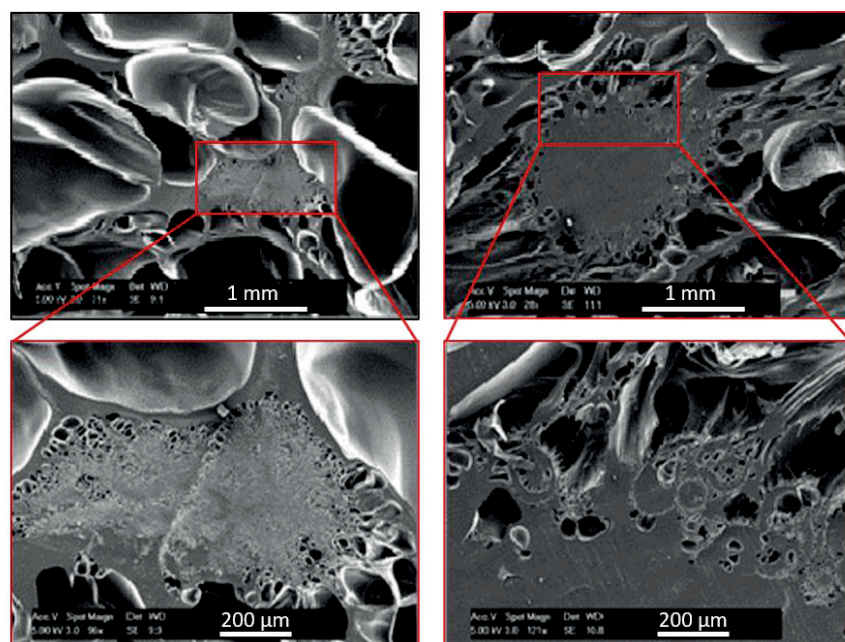


Figure 4.3 Comparison between T1 (left) and T2 (right) foaming conditions on PLAm1 granules.

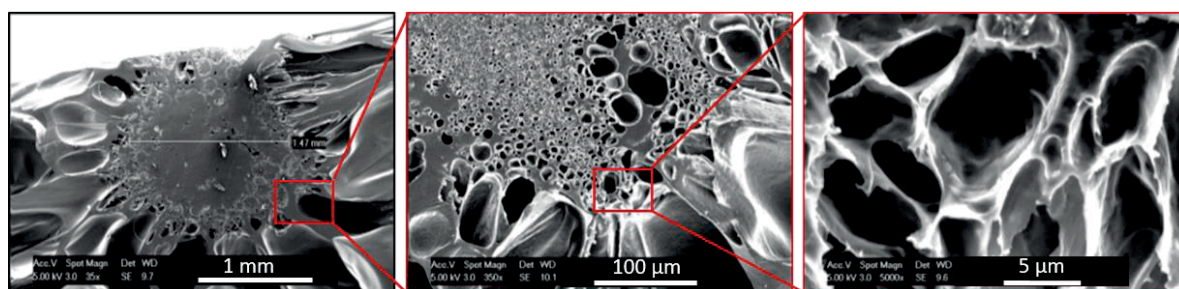


Figure 4.4 Porosity gradient produced by T2 foaming conditions on a PLAm1 granule.

To continue the investigation on the influence of the remaining foaming parameters on PLAm1, a processing temperature of 130 °C was selected. This saturation temperature allows keeping the core of the granule, producing a self-reinforced foam. The influence of saturation time and depressurization rate on foam morphology are therefore required to build a processing window for PLAm1. From now on, an ensemble of PLAm1 granules will be used instead of a single granule, in order to understand the inter-expansion effect of the foamed structure.

As described in Chapter 3, three levels of intensity were investigated for each parameter. They were chosen as representative of standard value adopted in batch foaming of PLAm1 in previous works^{1,23}. A schematic representation of the foaming cycles applied is shown in Figure 4.5.

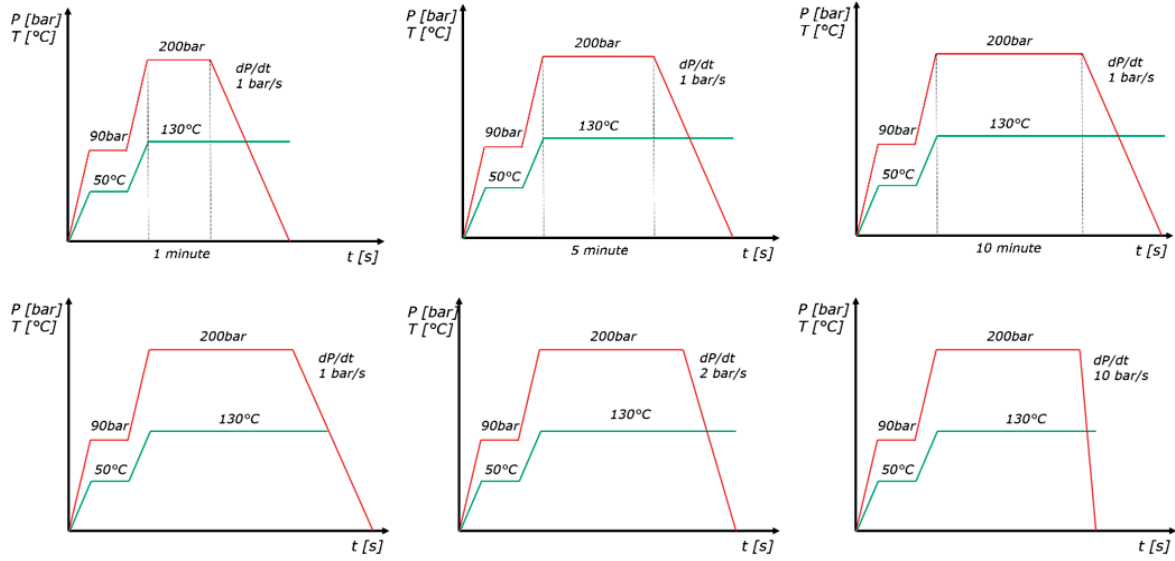


Figure 4.5 Schematic of the foaming cycles applied to investigate the influence of saturation time (top) and depressurization rate (bottom) on three different intensity level for each condition.

Porosity was measured as described in Chapter 3. It showed a significant increase between 1 minute and 5 minutes, growing from 65% to 83%. No significant differences were found between 5 minutes and 10 minutes. Thus, it is possible to reduce the material processing time by optimizing the CO₂ saturation step (Figure 4.6).

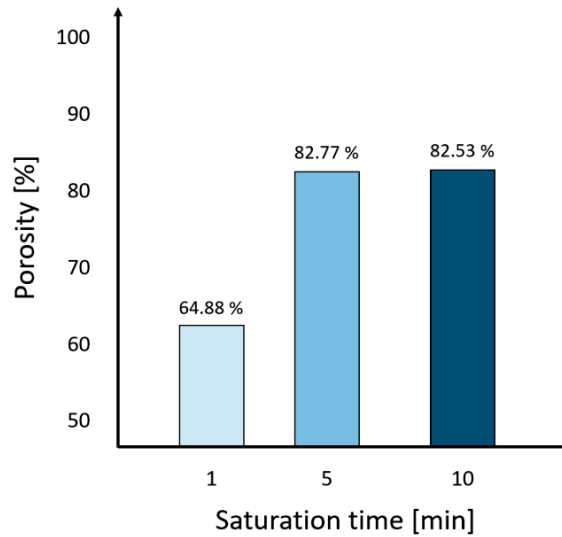


Figure 4.6 Effect of saturation time on foam porosity.

The depressurization rate was then investigated. As it is known from previous investigations on Poly(lactide) foaming, dP/dt has an important influence on foam expansion and pore morphology²³. As described in Figure 4.7, the depressurization rate is positively correlated with the foam porosity of single granules. When the same set of conditions are applied to different granules, it is demonstrated that the higher dP/dt , the more accentuated is the presence of an “arch shape” effect. This effect is due to the force applied to the central

granules in the mold during the depressurization. Increasing the depressurization rate, higher nucleation is promoted and a higher degree of porosity is achieved at the end of the partial foaming.

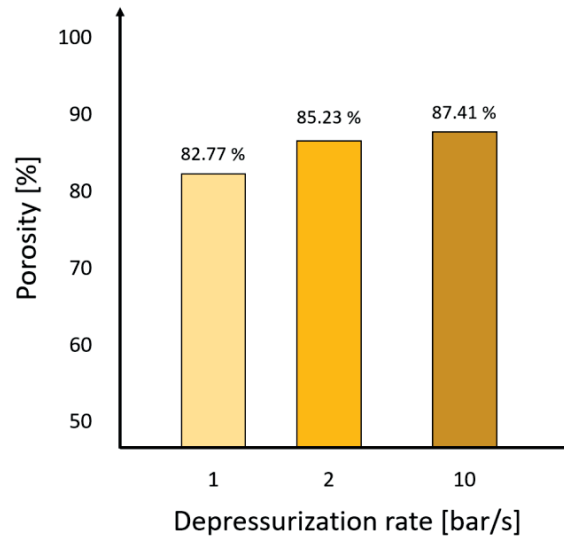


Figure 4.7 Effect of depressurization rate on foam porosity.

By controlling the foaming parameters, it was possible to create partial foaming of Poly(lactide), resulting in structures with un-molten core surrounded by shell of porous structure. The non-foamed core will constitute a stiff reinforcement of the final structure. The low foaming temperature is a key point of interest, which allows to minimize the material degradation during the processing. When applied to several Poly(lactide) granules, partial foaming allows producing self-reinforced structures with a characteristic “arch shape” related to the chosen depressurization rate. A schematic of the process is shown in Figure 4.8

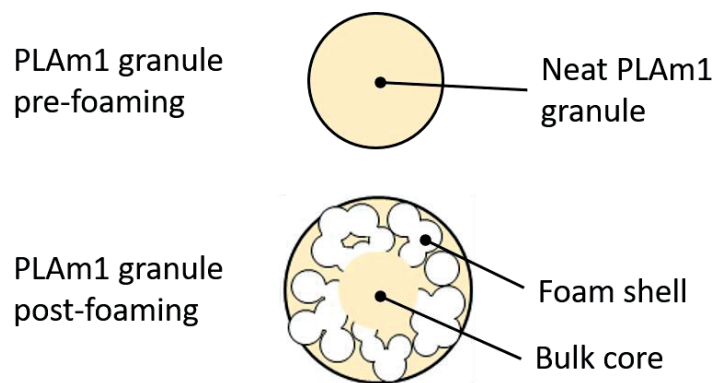


Figure 4.8 Schematic of the effect of homothetic foaming on a PLAm1 granule.

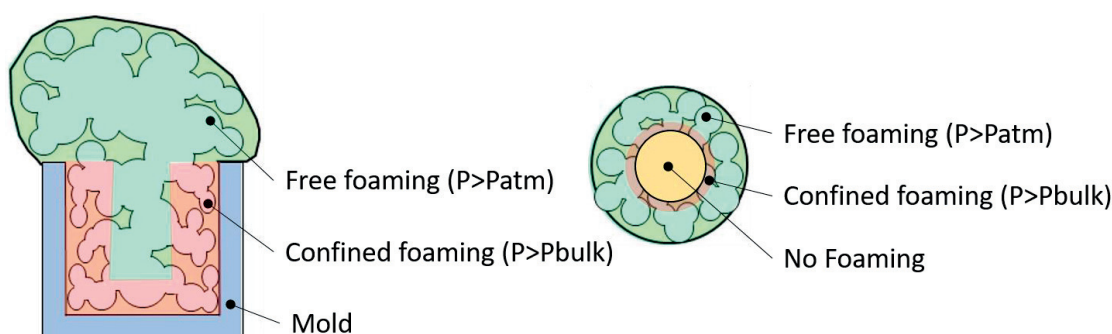


Figure 4.9 Schematic of the free foaming (green area) and confined foaming (red area) influences in batch foaming (left) and homothetic foaming (right). In batch foaming, the presence of the mold influences the foaming phenomena, which is dominated by the confined foaming. Smaller pores are formed as result of this process. In homothetic foaming, free foaming is the driving phenomenon, thanks to the absence of molds. Larger pores are formed homogeneously in the material.

From these results, it is possible to compare homothetic foaming with batch foaming, which represents the standard method to process thermoplastic materials with supercritical foaming (Figure 4.9). In batch foaming, the material is processed in forms of granules or powder. Those are collected into a metallic mold that helps keeping the granules or powder in place and gives the final shape to the foam. The mold presence is mandatory here, as otherwise the material would be dispersed in the autoclave vessel. However, the presence of a stiff material influences the foaming process, creating a supplementary resistance to foam expansion. This phenomenon, called confined foaming, is due to the difference between the pressure of the mold (P_{∞}) and the pressure built by the CO_2 within the material (P_{CO_2}). On top of the mold, P_{CO_2} drives the pore growth as long as $P_{CO_2} > P_{saturation}$, which occurs during the depressurization. The foam here has no precise shape, but expands freely in the space. This phenomenon takes the name of free foaming. Batch foaming is a confined foaming dominated process, as most of the material expands within the constraints given by the mold. Homothetic foaming represents an innovation from this point of view, as being dominated mostly by free foaming due to the absence of a mold. As seen from Figure 2.6, porosity is influenced by two parameters occurring during the depressurization phase: pore nucleation and growth. A parallel can be drawn between confined foaming and free foaming. Pore growth happens when the local pore pressure is higher than the external pressure, driving the pores and therefore the overall material to expand. Free foaming can be described as a growth-dominated phenomena while confined foaming with its higher external pressure is nucleation dominated.

From the knowledge acquired for the homothetic foaming of single granule, the process can now be extended to 2D and 3D structures. One of the best current technology to produce complex tridimensional structures in Poly(lactide) is FDM/FFF. In the next paragraph, homothetic foaming will thus be investigated on a 2D window and a 3D cellular structure, both produced by FDM/FFF as described in Chapter 3.

4.4 Homothetic foaming of 2D and 3D printed structures

A 2-dimensional window was designed in Sketchup. The main objective was to create a thin structure in order to neglect possible deformation induced by the foaming process. The structure is considered 2-D as the thickness is comparable to the minimum layer height printable. A schematic of these structures is shown in Figure 4.10. The 3D cellular structure was designed by Sketchup. A circular 3D shaped with 0.5 mm beams homogeneously spaced by 1 mm was designed.

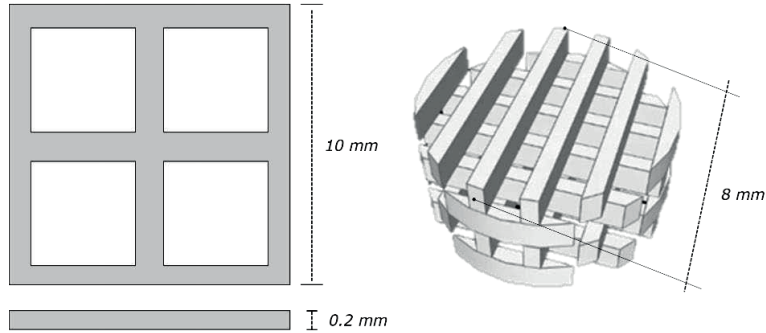


Figure 4.10 Schematic of the 2D and 3D structures.

4.4.1 Morphology and porosity

From the knowledge acquired in the previous chapter on the influence of the foaming parameters on partial foaming, it was then possible to process 2D and 3D structures into hierarchical cellular structures by the same principles. The printing and foaming protocol followed the methods described in Chapter 3.

Examples of obtained 2- and 3-dimensional homothetic foamed structures are shown in Figure 4.11 for the foaming cycle: 130 °C, 140 bar, 5 min, 10 bar/s except Figure 4.11E, where $dP/dt = 1$ bar/s. Table 5 is a schematic of the foaming conditions used for PLAm1 3D printed structures

Table 5 Foaming conditions to tailor the micro porosity within the 3D printed structures of PLAm1.

NAME	Tsat [°C]	Psat [bar]	tsat [min]	dP/dt [bar/s]
S1	130	140	5	1
S2	130	160	5	1
S3	130	140	5	50
S4	130	160	5	50

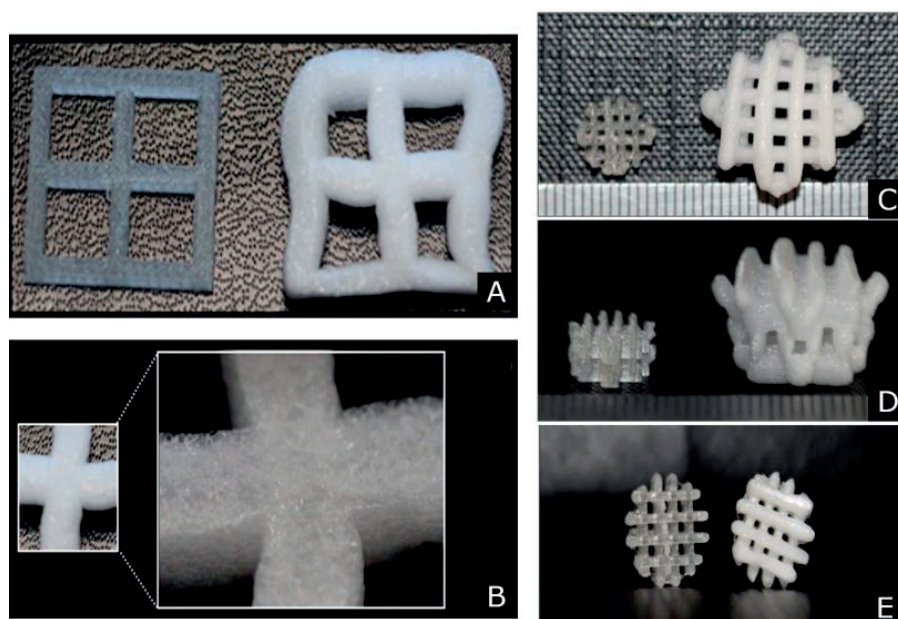


Figure 4.11 (A) the 2d structure before (left) and after foaming; (B) the micro-cellular structure can be observed within the foamed strands of the 2D structure; (C)(D) effect of the foaming on the 3D structure (top view and lateral view, S4 foaming conditions from Table 5) (E) influence of the low depressurization rate on the foaming (S1 foaming conditions from Table 5).

The deformation of the 2D structure in the x-y plane as consequence of the high depressurization (10 bar/s) can be observed in Figure 4.11A. The PLAm1 beams composing the structure are completely foamed. This micro porosity originates from the expansion of the original 3D printed beams composing the 2D structure (Figure 4.11B). Nevertheless, some deformation is observed in the 2D structure, the overall shape is kept. The rudiments of homothetic foaming by which the foaming should occurs only within the 3D printed material is therefore here proven. Moreover, the homogeneous foaming of the 2D structure opens the possibility to test the same processing conditions with a 3D structure.

When applied to a 3D structure, the homothetic foaming produced a higher expansion compared to the 2D structure. The observed expansion is homogeneous in each direction, producing an overall homothetic transformation of the material. As previously seen for the partial foaming of single granules, the bulk material is expanded as a consequence to the creation of a micro porosity. This expansion is generated by the diffusion and nucleation of CO₂ during the saturation and depressurisation phases of the foaming. As it could be appreciated by these images, the overall 3D shape is kept, along with the distance between the beams delimiting the macro-porosity of the 3D structure. The expansion in the x-y plane and z plane, as measured on n=3 samples, has less than double the size of the original 3D printed structure due to the creation of the micro-porosity within the bulk strands.

Reducing the depressurization (dP/dt) from 10 bar/s to 1 bar/s a more conservative 3D structure is produced (Figure 4.11E). Expansion is observed, confirming the results previously obtained on the influence of the depressurization rate. In order to quantify and qualify the micro porosity produced during the homothetic foaming, SEM analysis in a cross-section of these structures is required. Homothetic foaming was applied to PLAm1 as well as to PLAm2 to understand the reproducibility of the process with different Poly(lactide) grades. The

SEM analyses provide detailed information on the dimensions and scales of the obtained cellular structures as illustrated in Figure 4.12 and Figure 4.13 for the two investigated grades of PLA.

The deposition of filaments offered homogeneous beam elements respecting the initial selected dimensions. There are no large defects into the multifilament beams. Nevertheless, the beam surface has a roughness given by the diameter of the deposited filaments. The beams are assembled to build a multi layered structure; the distance between the beams will dictate the macro porosity size, distribution and orientation. Beam surface filaments might be deformed during the process and bent into the macro porosity.

Foaming of the printed structure successfully leads to porosity into the filaments and thus porous beams were obtained. The beams are still connected after foaming and the 3D morphology is intact. The foaming process is isotropic and thus produces expansion of the structure in each direction. The obtained structures demonstrate the feasibility of the chosen processing steps and parameters to obtain cellular scaffolds with dual porosity at macro and micro levels. The tuning of the processing parameters could still offer more morphologies for different applications.

Confined foaming and free foaming, discussed in Figure 4.9, have a notable influence in the development of the micro porosity during the homothetic foaming of the 3D structures. As seen in paragraph 4.3, homothetic foaming is driven by free foaming phenomena or pore growth phenomena, allowing the creation of a micro-porosity within the beams composing the macro-porosity. Given the pore growth dominance in this process, larger pores freely expand up to a maximum dimension, above which consequent pores collapse into forming a bigger pore. This is observable in Figure 4.12F, where a larger pore is formed at the center of the beam, where the free foaming is maximum. Confined foaming is still observable in these hierarchical cellular structures, especially at the intersection of the beams. As seen in Figure 4.12C and Figure 4.12E, smaller pores are formed towards the edges of the 3D structure.

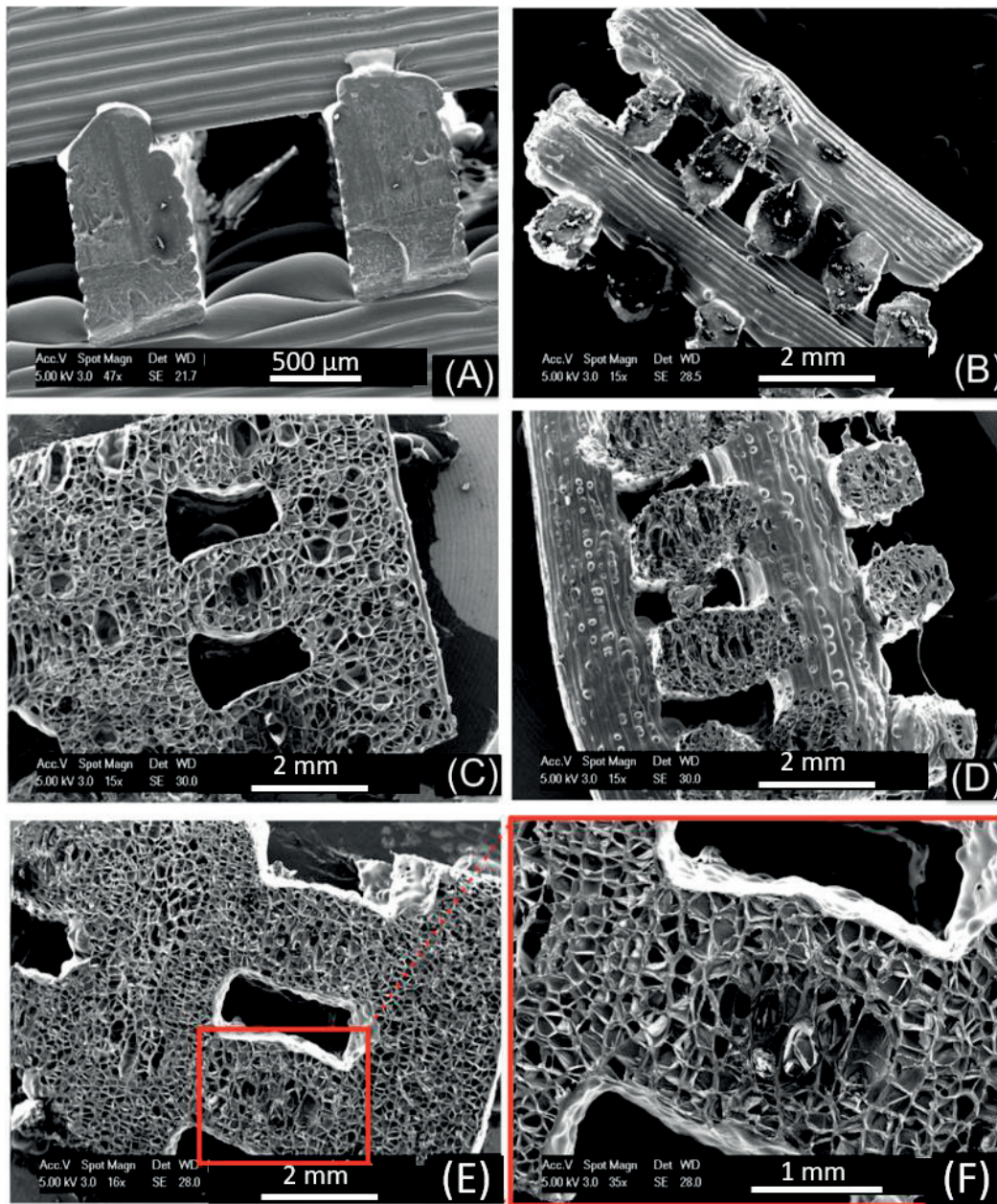


Figure 4.12 (A) neat PLAm1 polymer, (B) 130 °C 140 bar 1bar/s (S1 Table 5), (C) 130 °C 140 bar 50bar/s (S2 Table 5), (D) 130 °C 160bar 1bar/s (S3 Table 5), (E) 130 °C 160bar 50bar/s (S4 Table 5), (F) detail of the beam micro porosity.

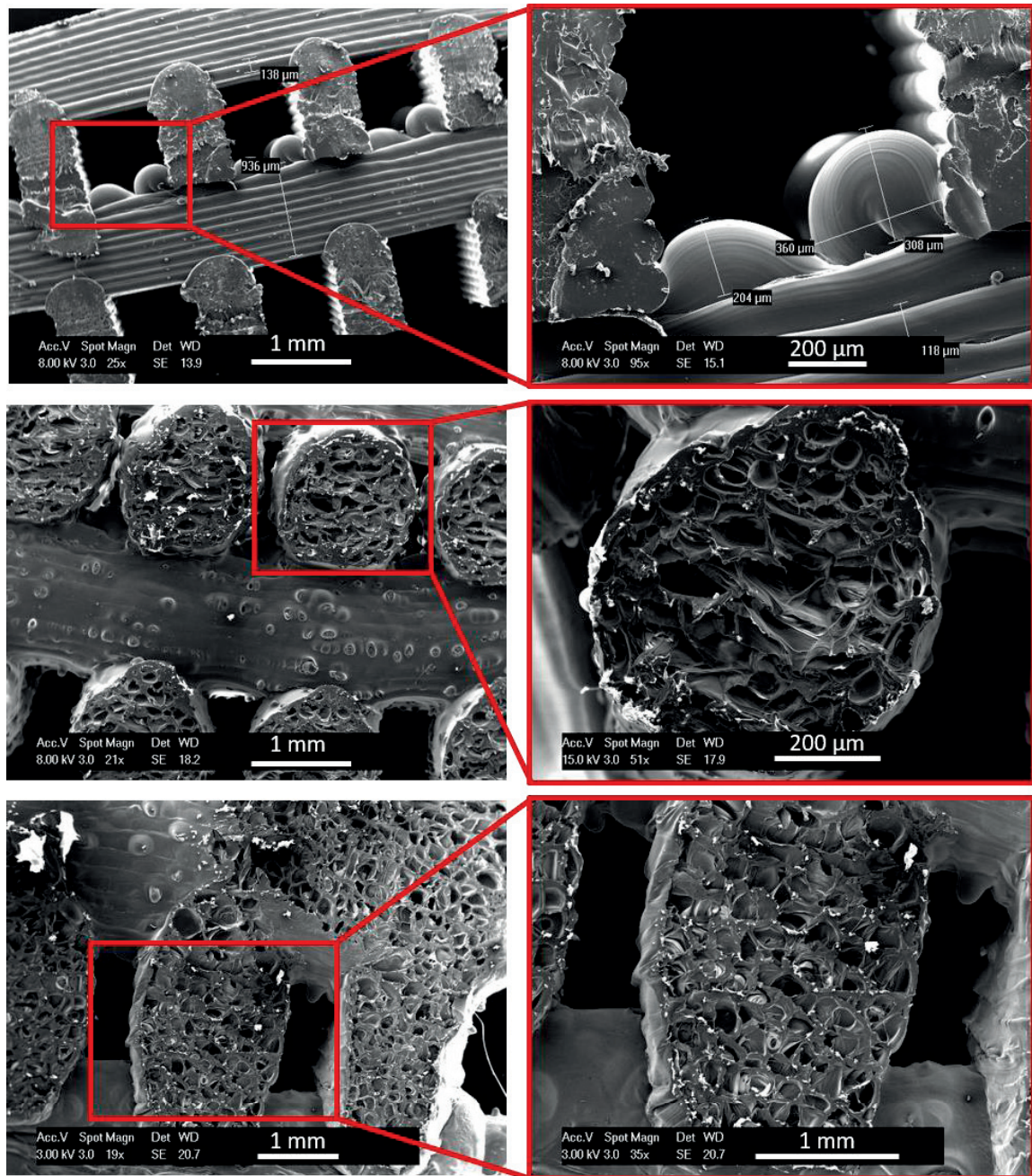


Figure 4.13 (A) Neat PLAm2, (B) detail of the neat polymer, (C) 120 °c 130 bar 1bar/s, (D) detail, (E) 120 °c 130bar 50bar/s, (F) detail of the beam micro porosity.

4.4.2 Properties of cellular structures

Homothetic foaming has been proven to be applicable to PLAm1 and PLAm2 cellular structures. The mechanical properties of the final structures are therefore deriving from the mechanical properties of the original 3D printed structure (representing the maximum achievable value for a given geometry) and from the creation of a micro-cellular porosity in place of the bulk material. As seen in Chapter 3, an increase of porosity produces a decrease of density, this decreasing the overall stiffness of the structure. The aim of this paragraph is to understand the range of mechanical properties achievable with this process starting from different cellular structures. In particular, two cellular structures were selected: one with 40% porosity (e.g. thicker and closer beams) and one with 60% porosity. Figure 4.14 and Figure 4.15 illustrate the influence of the beam macro porosity on the compression performance of the structure.

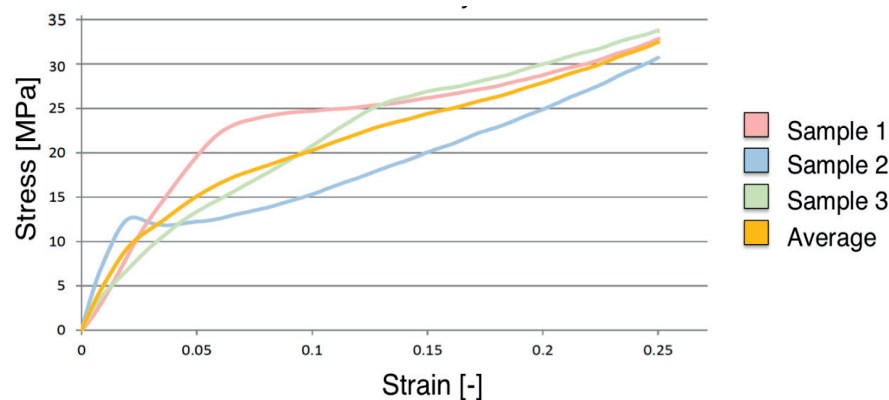


Figure 4.14 Compression behaviour of a 3D printed cellular material with 40% interconnected macro porosity.

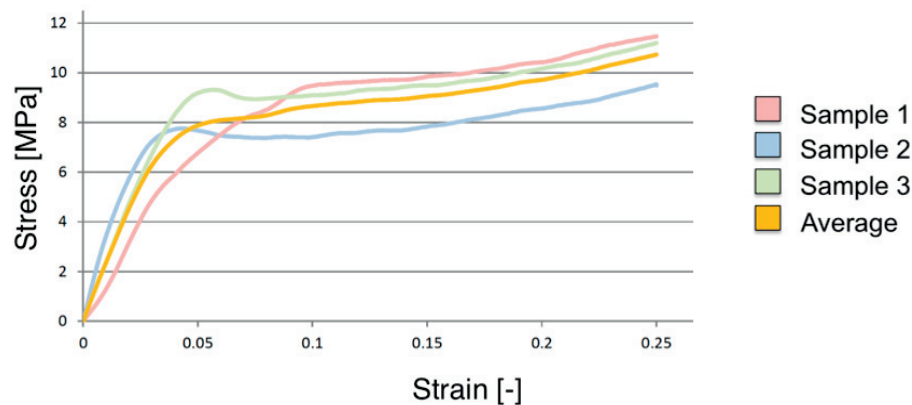


Figure 4.15 Compression behaviour of a 3D printed cellular material with 60% interconnected macro porosity.

Mechanical properties of the initial 3D printed structures are affected by the model design, e.g. the beams size, the distance between the beams and their height. It is important to notice the classical S shape of the stress-strain curves, which reflect the response of a cellular structure with open pores in compression.

After the demonstration of the ease of tuning of the printing parameters to produce the desired compression response, the effects of different foaming parameters were analysed. The foamed structures were obtained by inducing micro porosity during supercritical foaming in the 3D printed beams. The mechanical properties

of the initial structure are then considered as the standard to study the effect of the micro porosity, as showing in Table 5.

Figure 4.16 shows the influence of the investigated foaming conditions on the compressive response of the obtained structures in comparison with the original 3D printed structure. The preliminary observations drew from observing the material morphology at SEM (Figure 4.12 and Figure 4.13) were here confirmed. By increasing the porosity inside the beams, the structure stiffness becomes smaller and smaller, reducing both strength and modulus. The depressurization rate has more impact on the final structure than the saturation pressure, as it is inferable observing S1 and S2 response (dP/dt constant, P_{sat} from 140 to 160 bars) compared to S1 and S3 (dP/dt from 1 to 50 bar/s, P_{sat} constant). S1 shows a poor porosity of the beams (Figure 4.12B) and therefore a limited expansion. On the other hand, high depressurization induces more porosity in the beams, with larger pores. This porosity produces the softening of the 3D structure, as observable for S3 and S4. The material response to compression is almost flat when compared to the 3D printed structure. The deformation mechanisms for these hierarchical cellular structures are shown in Figure 4.17 as opposed to the classic buckling of cellular structures with cubic cells shown in Figure 2.3. Under compression, the 3D printed structure shows an elastic behaviour up to about 0.1 strain, followed by a buckling plateau between 0.1 and 0.25 strain. Above 0.25 strain, the densification starts and the overall stress grows linearly with the strain. In all the 3D structures further processed by homothetic foaming, the buckling plateau is much less pronounced in the stress-strain curve. After an elastic response up to 0.15 – 0.3 strain, the corresponding to the compression of the foamed beams, the cells of the micropores collapse and at the same time the macropores disappear inducing a densification. The buckling plateau does not really appear in these structures as the creation of the micro-porosity creates a “deformation buffer” as opposed to the deformation mechanism of the only 3D printed structure. The amount of micro porosity induced by homothetic foaming thus withstands a part of the progressive compressive load, the pore cells deforming along with the progressive loss of macro-porosity. The foaming clearly allows to tailor the stiffness of a given printed cellular structure.

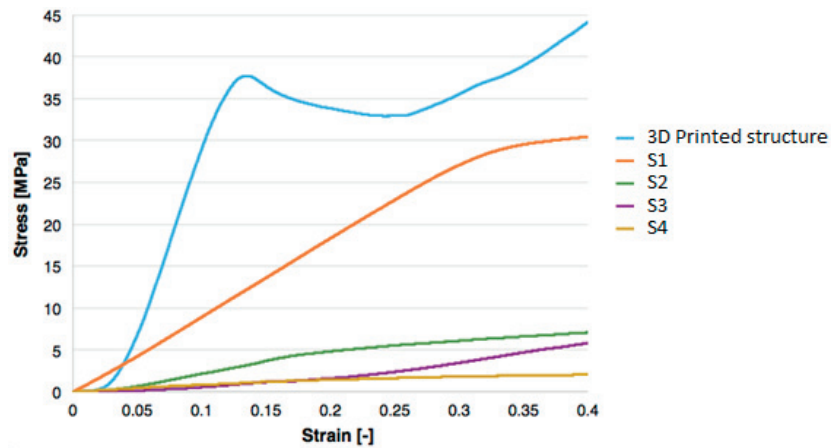


Figure 4.16 Tailoring of mechanical properties by foaming a 3D printed structure (PLAm1).

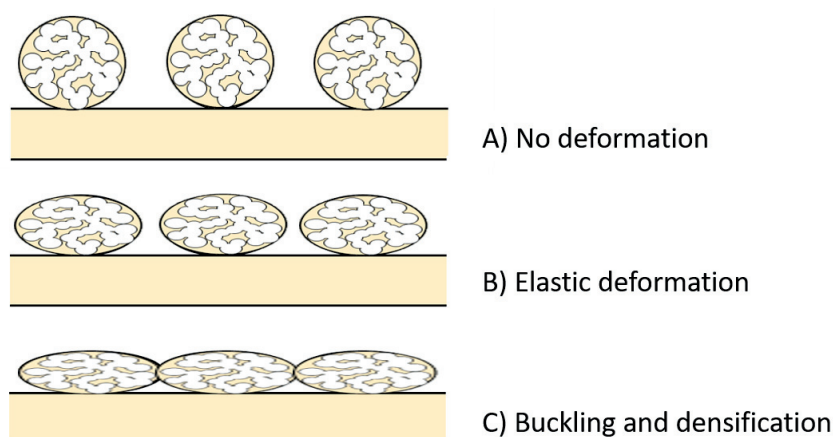


Figure 4.17 Deformation phenomena in 3D cellular structure with a macro and micro-porosity. A cross-section of the original structure is shown in A), where no deformation is applied. In B), the beams start deforming under the compressive load, following an elastic behaviour. Following the stress-strain response, a densification by loss of the macro porosity and collapsing of the micro-pore cells occur at high strains.

Indeed, two dominant processing parameters were thus identified: saturation pressure and depressurization rate, confirming thus the previous results obtained on the PLAm1 single granules. The other foaming parameters e.g. saturation temperature and time were neglected given the results obtained in the previous granule homothetic foaming section. Indeed, foaming temperature and saturation pressure showed a crucial role to keep the 3D structure integrity during the foaming process, but they do not strongly contribute to micro porosity creation within the bulk material. This is supposed to be principally related to the low influence of these parameters on CO₂ nucleation and expansion in homothetic foaming, compared to their role in standard batch foaming. The depressurization rate however strongly influences the development of a micro porosity within the bulk material. High dP/dt is required to produce a highly micro-porous cellular structure. However, the higher the micro porosity, the higher will be the foam expansion, incrementing up to three times the volume of the original 3D printed structure. The mechanical properties of such macro and micro porous cellular structure can therefore range from hundreds of MPa to few MPa. This capability to produce 3D structures with tailored mechanical properties derives from the density reduction of the original 3D structures, which leads to softer cellular structures as described in Chapter 2. This behaviour is respected for the two studied model materials, PLAm1 and PLAm2. Young's modulus was extracted on Figure 4.18 and Figure 4.19 from the linear region stress-strain regions of all the structures processed with the conditions of Table 5. Starting from about 400 MPa for the reference 3D printed structure, E decreases to 279 MPa for the structure barely foamed (e.g. low micro porosity, Figure 4.12B) and drops to 29 MPa with the increase of the dP/dt . The difference between the average stiffness value between the two Poly(lactide) 3D printed structure before foaming (398 MPa vs 415 MPa) is due the small difference between their Young's Modulus (3.5 GPa for PLAm1 vs 3.6 GPa for PLAm2). This initial difference in the stiffness of the 3D printed structure is thus shown in all the consequent foamed samples, i.e. PLAm2 structures after foaming are always stiffer than PLAm1 samples after the same foaming cycle. The minimum stiffness measured is 8 MPa, about x50 times softer than the original 3D printed structure.

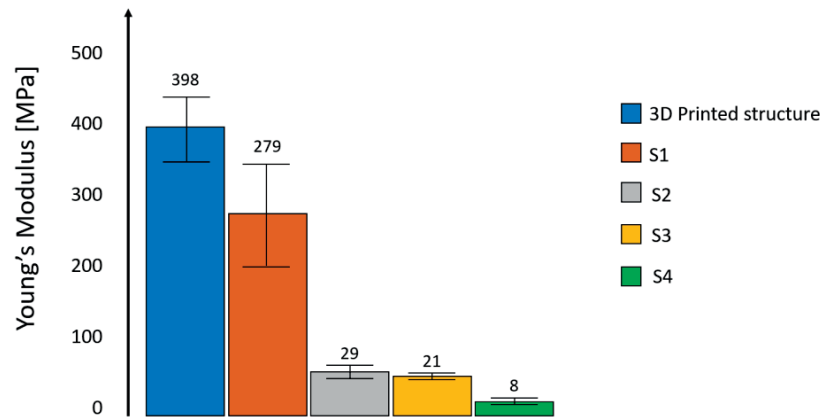


Figure 4.18 Effect of the different foaming parameters on the Young's Modulus, PLAm1

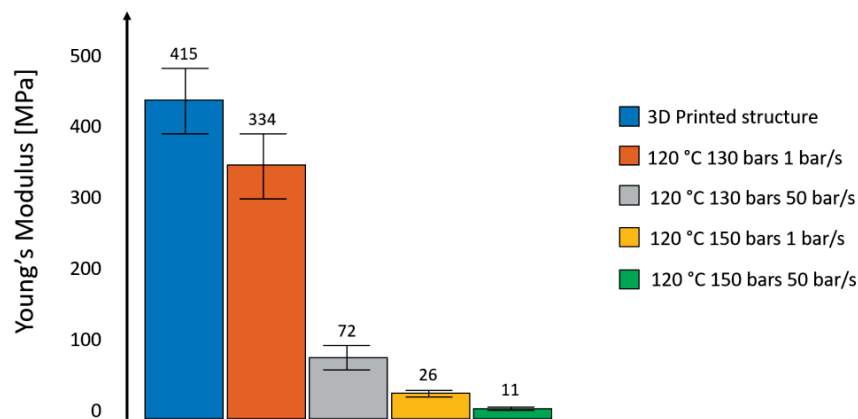


Figure 4.19 Effect of the different foaming parameters on the Young's Modulus, PLAm2

4.5 Conclusions

The process to create a dual porosity into a 3D polymer structure was established. First the influence of the foaming parameters on simple PLA granules was investigated to determine whether a controlled partial foaming is possible. It was shown that supercritical foaming could be exploited to create a self-reinforced polymer material composed by a solid bulk core surrounded by a foamed porous surface. The control of a low foaming temperature and a short saturation time was key to generate such morphology by homothetic foaming on PLA granules. The effect of foaming parameters, such as saturation temperature, saturation time, pressure as well as of depressurization rates were investigated on a model PLA material. Compared with confined batch foaming, homothetic free foaming was shown to be controlled by the depressurization rate more than other parameters and is more driven by pore growth than nucleation. This promote a foam expansion with larger pores and subsequently more coalescence of pores and thus higher interconnectivity⁸.

The second part of the study explained how to tailor the process to produce dual porous materials in complex 3D structures. Filaments of model PLA materials were deposited by Fused Deposition Modelling to form beams and thus build layered structures composed of those oriented beams. The structures were then foamed. The process was proven to be applicable first to a 2D structure and then to a 3D cellular structure

or scaffold. A macroporosity is created between the deposited beams and a micro-porosity inside the beams upon the foaming.

Scanning Electron Microscopy was used to investigate the quality and limitations of the process by analysing the porosity morphology before and after the processing. Pores distribution and shape changes were observed. As example, it was shown that while the saturation time do not strongly influence the foam expansion and the average porosity, the depressurization rate showed a remarkable positive influence on both properties.

The final cellular morphology is sensitive to the processing parameters. The saturation temperature should be chosen at the beginning of the melting peak of the material in order to avoid complete melting of the structure during the foaming. It has been then shown how at low foaming temperatures, the process is driven by the depressurization rate. The higher the dP/dt , the higher is the structure expansion by more porosity induced in the beams and walls of the 3D printed structure. Secondly, saturation pressure had an effect on the morphology. At higher pressure, more CO_2 diffused in the material, leading to a more porous 3D structure. The combination of 3D printing with supercritical CO_2 foaming allows producing cellular structures with well-defined macro porosity and homogeneous micro porosity. The fine tuning of these dual porosities allows controlling as well different structure properties as the local and overall stiffness and obviously the permeability. A wide range of mechanical properties was measured when considering the non-foamed and foamed 3D printed structures. The elastic deformation of the micro-porous beams coupled with the disappearance of macro-porosity upon deformation explain the stress-strain behaviors. The determined processing windows offer the possibility to vary the Young's modulus of a 3D printed structure up to 50 times.

These results suggest that the combination of 3D printing and supercritical foaming could be applied to tailor complex hierarchical structures with a dual macro-micro porosity. The process potential was studied for two PLA model materials widely used in FDM/FFF 3D printing for various applications. However, medical grade PLA filaments are not available in commerce. Following the idea to apply homothetic foaming to produce hierarchical cellular structures for osteochondral repair, the knowledge acquired on the model materials will be applied to different biomedical grade polymers. The approach will be to process a single material 3D printed structure into a set of micro-macro porous structures at first, determining the processing windows for such materials. In a second phase, homothetic foaming will be applied to multi-material structures, producing 3D structures with only macro porosity in one material layer but macro and micro porosity in an other material and layer.

Chapter 5 Homothetic Foaming of 3D Printed Multi-Material Structures

5.1 Introduction

The processing of a material into a cellular structure is relevant in many fields of application, as discussed in Chapter 2. Some of these applications require a further step: the processing of different materials into multi-material structures. This is particularly true when designing scaffolds for the tissue engineering of osteochondral defects. The osteochondral tissue is composed by articular cartilage and subchondral bone. The ideal osteochondral scaffold for tissue repair requires therefore a multi material structure to mimic the properties of these two tissues, offering different stimuli for cells growth. Moreover, the progressive stiffening of the osteochondral tissue from the superficial cartilage layer to the subchondral bone should be reproduced.

Homothetic foaming was successfully applied to process Poly(lactide) into controlled macro and micro porous structures, as described in Chapter 4. The present chapter will describe how to apply homothetic foaming to medical polymers and selectively foam one material of a multi material structure, creating a dual porosity hierarchical scaffold. At first, FDM/FFF of medical filaments is discussed, investigating how to successfully print cellular structures from a set of medical materials. The mechanical properties of such 3D printed structures will be investigated in a buffer solution (PBS) to better reproduce the environmental conditions and compared with the results obtained in air. Then, these medical materials will be combined into multi-material structures by FDM /FFF, investigating the mechanical properties of such structures compared to the single material structure. Finally, homothetic foaming will be applied to a selection of these multi-material structures of medical polymers, describing how to tune the foaming parameters to selectively foam part of the material and explore novel cellular architectures. From these results, two materials will be selected to be combined into a hierarchical cellular scaffold for osteochondral repair.

5.2 Materials and methods

5.2.1 3D Printing

Medical filaments for Fused Deposition Modelling / Fused Filament Fabrication (FDM / FFF) are today not available on the market. All the results shown in this chapter were gathered using in-house produced filaments of medical materials, as discussed in Annex I. Table 5 resumes the main extrusion parameters (temperature and motor speed) used to obtain the filaments. At a first time, single layer scaffolds were printed. Then, the possibility to combine two materials to create a 3D multi-material structures was investigated Figure 5.1.

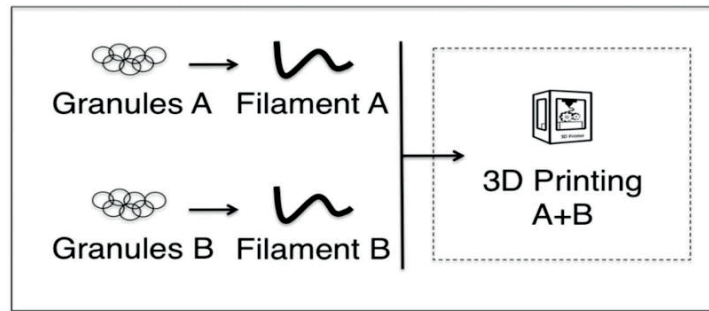







Figure 5.1 Schematic of the process to create a multi material structure.

A filament of each material was chosen for the printing of the single layer scaffolds. For the production of multi material scaffolds, five combinations of the medical grade materials were tested as shown by the five colour codes in Table 6. A letter is assigned to each color code (e.g. A = purple, B = red, C = blue, D = yellow, E = green) and identifies a specific multi-material structure. As example, PLAPCL/PLABTCP corresponds to combination E.

Table 6 List of the materials, filaments production parameters and combination in multi-material structures. Combination letters (A = purple, B = red, C = blue, D = yellow, E = green) correspond to materials coupled into a multi-material structure (e.g. PLAPCL/PLABTCP corresponds to combination E)

CLASS	MATERIAL	COMBINATION	TEMPERATURE [°C]	MOTOR SPEED [rpm]
MODEL	PLAm1	A B C D E	185	30
MEDICAL	PLLA		230	10
	PLAPCL		170	30
	PLAPGA		170	30
	PLAPEG		170	60
	PLABTCP		190	50

Different models have been developed with CAD software (i.e. Sketchup). The objective was to create scaffolds with different macro porosities respecting the printing limits such as: nozzle diameter (0.4mm), resolution and bending of the structure. Cylindrical geometries were designed with porosity: 75 %, 67 %, 50 %, 34 %, 20 % and 0 %. As shown in Figure 2.2, the pore size is determined by the distance between two contiguous beams. Even if FDM/FFF is able to reproduce complex geometries, it still suffers some of the limitations of the extrusion of a viscous material. Bridging and overlapping of the strands are two of the main concerns when designing and printing a cellular material. These defects are illustrated in Figure 5.2.

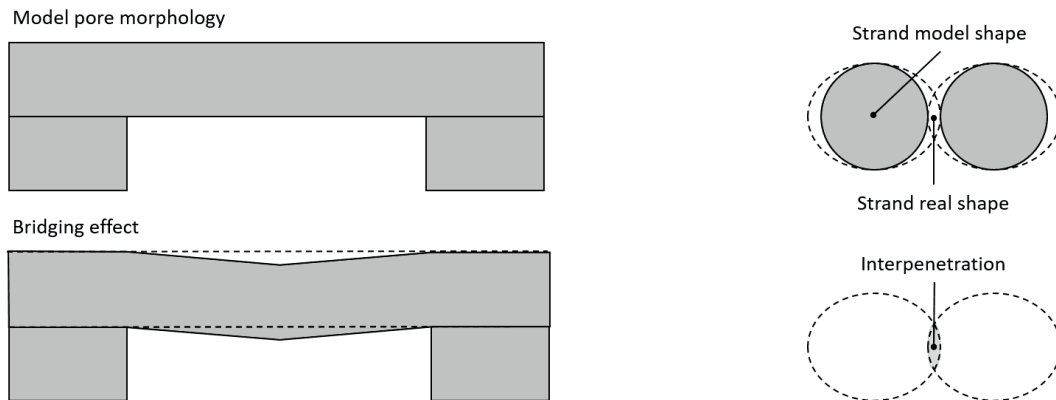


Figure 5.2 The porosity in a 3D printed object obtained by FDM/FFF is limited by two main phenomena: bridging (left) and overlapping (right). Bridging occurs when the polymer viscosity is too low to correctly connect two points, introducing a deformation in the extruded strand. Overlapping is due to the compression introduced by the contact of the polymer with a surface, which alters the radius of the strand. When two points are too close, they might connect and prevent the creation of a pore in the between.

The bridging effect happens when a strand is extruded from a point to another without the proper support. When the distance between the points exceeds a critical value (determined empirically from material viscosity), the strand bends under its weight, introducing an error in the structure (Figure 5.2, left). On the other hand, when two strands are too close, an undesired overlapping might occur as consequence of the constrained free volume between the nozzle tip and the surface beneath (Figure 5.2, right). These two phenomena shall be taken into account when designing and slicing a 3D object and are the main accountable of the limited range of porosities achievable within a cellular material. In Figure 5.3 some examples of models designed avoiding bridging and overlapping effects are reported:

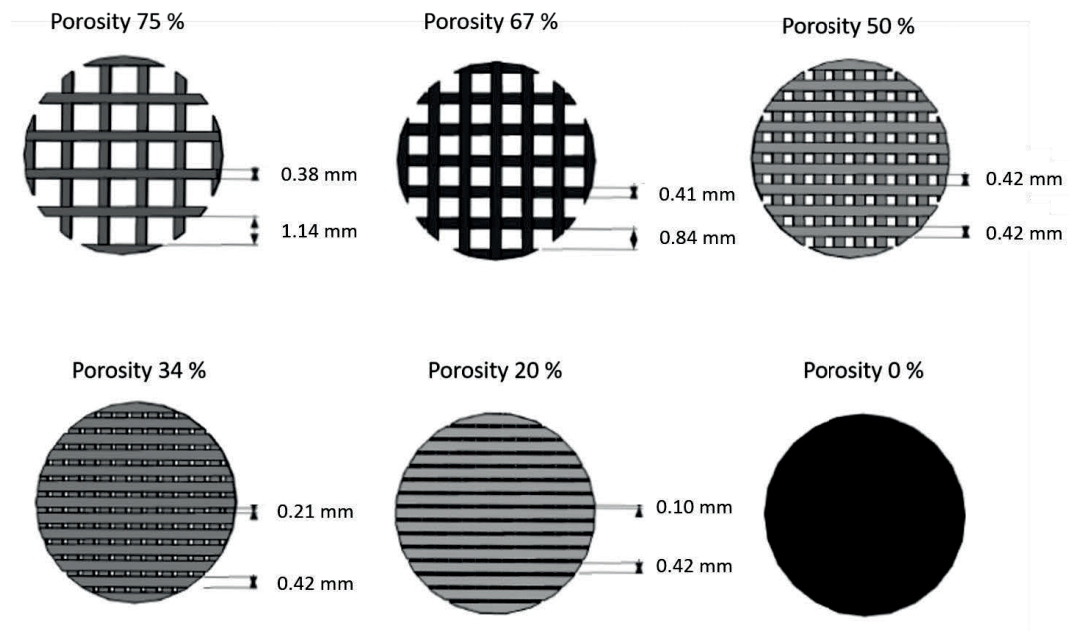


Figure 5.3 Examples of the 3D models designed to have different strand spacing to produce a range of porosity.

Moreover, these geometries need supports on the edges, due to the circle shape that prevent each strand of one layer to have a full contact, this lead to imperfections on the edges. This problem limits the porosity of the scaffold, because if the strands are too far apart from each other the structure will not bridge. This is a principal limitation when using FDM/FFF to produce cellular structure. Some improvements can be obtained by tuning the printing speed and the printing temperature to increase the viscosity. Also, the model can be as well optimized for the printing process. In this case, a discretized shape has been developed to overcome the limitation posed by the bridging effect. This simplified geometry allows printing easily high definition scaffold without any extrusion problems. The dimensions are the one showed in Figure 5.4 and the porosity is 62 %.

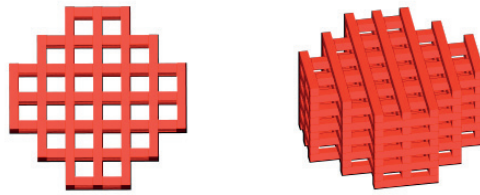


Figure 5.4 Optimized 3D geometry to minimize printing defects, as overhanging, bridging and strands bending. The structure has a theoretical porosity of about 62 % for 8 mm diameter and 4 mm height.

From now on, this geometry will be kept as reference for all the future mechanical and biological tests. Once the models were defined, all scaffolds were printed with the same geometry and porosity, varying only the materials. In particular, three different materials were involved: PLAm1, PLLA and PLABTCP. As previously shown in Figure 5.2, material viscosity influences the printing quality of a cellular structure. For this reason, different sets of printing parameters (e.g. temperature and speed among all) were selected to optimize the final result:

- PLAm1 is easily printable with temperatures ranging from 200 °C to 230 °C, as discussed in Chapter 4 and Annex II.
- PLAPCL has been selected among all the materials as the ideal candidate for cartilage substitution, thanks to its great flexibility, low hardness and its viscoelastic properties. Due to that, printing PLAPCL structures requires attention to avoid overbridging of the strands and buckling of the structure. Thus, it was necessary to lower the printing speed and temperature to obtain a more regular geometry. The quality of the printed scaffold is therefore directly affected, leading in some cases to under-extrusion phenomena. Satisfying printing quality was achieved for different systems, producing a well-shaped 3D structure. The printing temperature was set at 185 - 190 °C.
- PLABTCP is a medical grade composite. The ceramic particles did not influence particularly the printing process and it was possible to produce high quality 3D structures. Printing temperatures ranged from 200 °C to 220 °C.

5.3 Mono material scaffolds

5.3.1 Morphology

The obtained single layer printed scaffolds for each of the different materials listed in Table 6 are displayed in Figure 5.5.

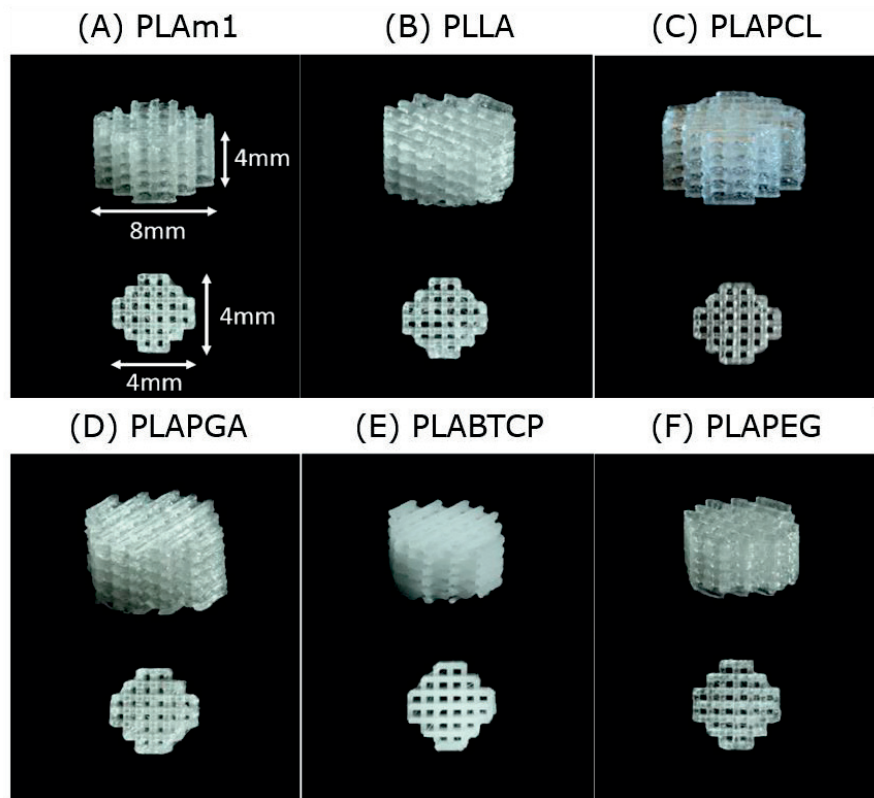


Figure 5.5 3D Printing of mono material scaffolds, lateral and top view.

A good printing quality was achieved for the different materials maintaining the structure and porosity of the constructs. Soft filaments, as PLAPCL, might jam in the feeding zone of the printer due to an increasing back-pressure at the back of the heating zone. This phenomenon, called “buckling” of the filament, leads to under-extrusion phenomenon and prevent the 3D structure to be correctly printed. In case of severe buckling of the filament no extrusion was achieved due to the complete obstruction of the nozzle. This effect was limited by decreasing the printing speed and thus indirectly the flow rate by increasing the printing temperature. In the latter case, it should be kept in mind that the process might lead to degradation of the deposited material.

Three materials were selected to continue the analysis towards the application for osteochondral tissue engineering: a soft PLAPCL, a composite PLABTCP and the model PLAm1. The PLAPCL scaffold was chosen as being the softest polymer degradable material available for FDM/FFF. The PLABTCP was chosen because its composite nature, recalling the bone composition. This material was also investigated in previous works for bone repair^{39,154}. Finally, the PLAm1 was chosen to continue the analysis on a well-known Poly(lactide)-based material. The next step is to determine the mechanical properties of such 3D printed structures, either as single materials and as 50:50 multi material.

5.3.2 Mechanical properties of the printed cellular structures

All the 3D printed structures of PLAm1, PLAPCL and PLABTCP were tested in air as described in Chapter 3. The same testing protocol was applied to unconfined uniaxial compression in PBS medium to better mimic the environment conditions. The scaffolds were left soaking in PBS for a day to ensure liquid saturation prior

the tests, which were conducted at starting temperature of 25 °C. The two compressive responses in air and in PBS were then compared for each material.

Under static compression at 0.5 mm/min PLAm1 structures showed a linear elastic behaviour from 0 to 7 % in strain, with a steep linear deformation. The average Young's modulus is equal to 386 MPa. A small plateau of buckling is shown from 7 % to 15 % of strain, after which densification of the pores happens and the stress rises up to 140 MPa at 60 % strain (Figure 5.6).

PLAm1 structures tested in PBS have a less visible and distinguishable linear region from the buckling deformation plateau, showing a progressive stiffening up to 130 MPa at 60 % deformation. The Young's modulus extrapolated is about two times higher from the test in air, accounting for 604 MPa (Figure 5.6, right). This stiffness increase for a cellular structure saturated with a fluid can be explained by the hydrostatic effect. As liquids are incompressible, when a deformation is applied to a saturated structure the fluid tend to flow out of the porosity. If the fluid flow is slower than the applied strain rate, the liquid will start to offer a resistance to the compression. When the fluid completely leave the structure, the compression response of the biphasic structure will fit again the expected compression response of the pure material.

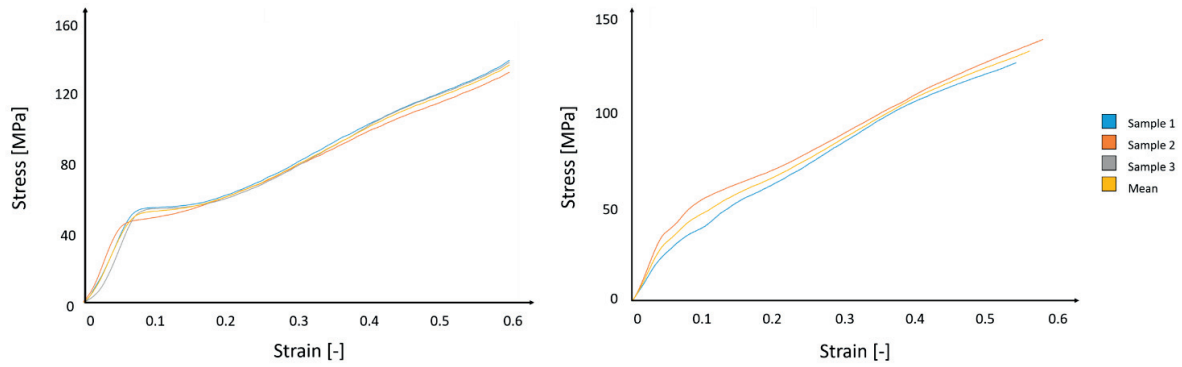


Figure 5.6 PLAm1 response in unconfined compression in air (left) vs in PBS (right).

PLABTCP structures showed an overall similar behaviour, having an elastic deformation up to 5 % and a long plateau from 5 to 30 %. The average Young's modulus is slightly higher than PLAm1, accounting for about 428 MPa. The stress experienced at 60 % deformation is 80 MPa (Figure 5.7, left). This increase in structure stiffness is expected from the addition of ceramic particles in the Poly(lactide) matrix, creating a composite material. The lower strength of PLABTCP structures compared to PLAm1 is explained also by the nature of the Poly(lactide) matrix of the PLABTCP composite.

In PBS, PLABTCP showed a similar behaviour compared to the previous tests in air medium (Figure 5.7, right). The linear elastic zone is unvaried, while the maximum stress is reduced from the previous value of 80 MPa to 60 MPa. The average Young's modulus is slightly increased from the previous value of 428 MPa to about 434 MPa. In this range of lower stiffness, it seems that the hydrostatic effect has a less remarkable influence. The walls can certainly deform more while still providing structural resistance. This effect will mask the compressive response of the fluid flowing out of the cellular structure.

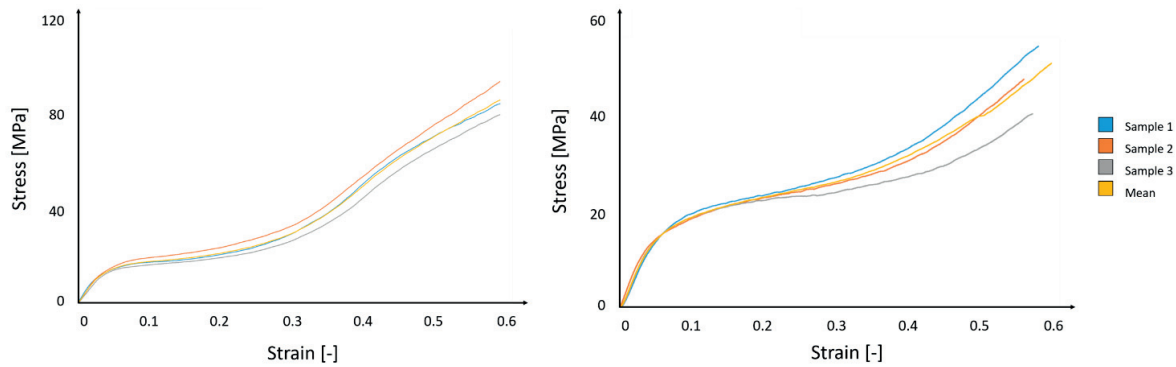


Figure 5.7 PLABTCP response in unconfined compression in air (left) vs in PBS (right).

As expected PLAPCL showed a completely different behaviour compared to the previous materials. The linear deformation region is almost indistinguishable from the wall plateau, due to the bending of the cell walls under compression. This effect is due to the intrinsic low stiffness of the neat material, which offers low resistance to the constant compression. Stresses are therefore distributed in the structure, which does not occur in any buckling up to 60 % deformation. A recap of the expected mechanics of cellular structure can be found in paragraph 2.2. The average Young's modulus is as low as 20 MPa. After densification at 60 %, the maximum stress is about 19 MPa, almost 20 times smaller when compared to previous materials (Figure 5.8 left). The role of the PCL to soften the PLA in the copolymer is clearly expressed here and transmitted to the stiffness, deformation and strength of the final 3D printed structure.

PLAPCL expressed the most important changes in PBS medium, showing at 60% strain stress three times higher compared to air medium. The linear elastic region is still indistinguishable from buckling and densification, confirming the hypothesis that the first two phenomena occur at the same time, given the softness of the material (Figure 5.8 right). The Young's modulus was calculated to be three times the value in air, rising from the original 20 MPa to about 60 MPa. Given the softer nature of PLAPCL compared to PLAm1 and PLABTCP, the compressive response of such a cellular structure saturated in water medium will be dominated by the hydrostatic effect. This explains the remarkable difference of PLAPCL structures' compressive response when tested in air or PBS medium.

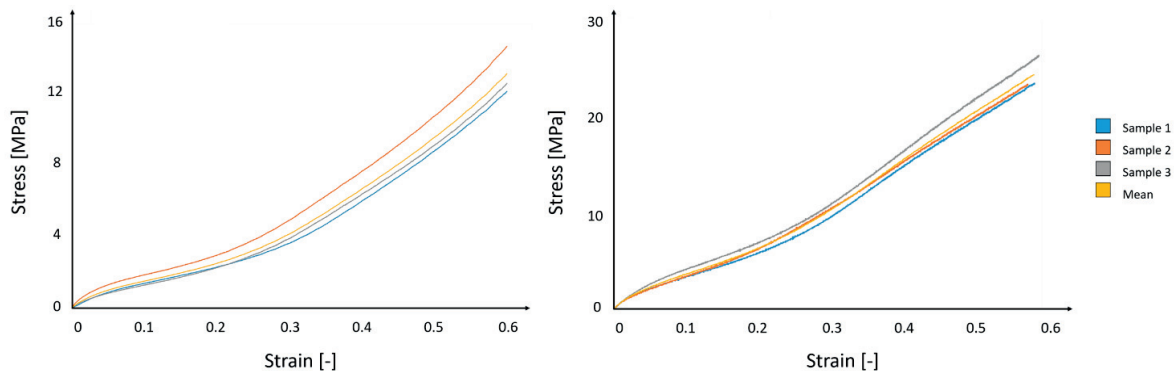


Figure 5.8 PLAPCL response in unconfined compression in air.

A summary of the scaffolds Young's modulus in air and PBS is shown in Table 6, while the scaffold response in air is compared in Figure 5.9.

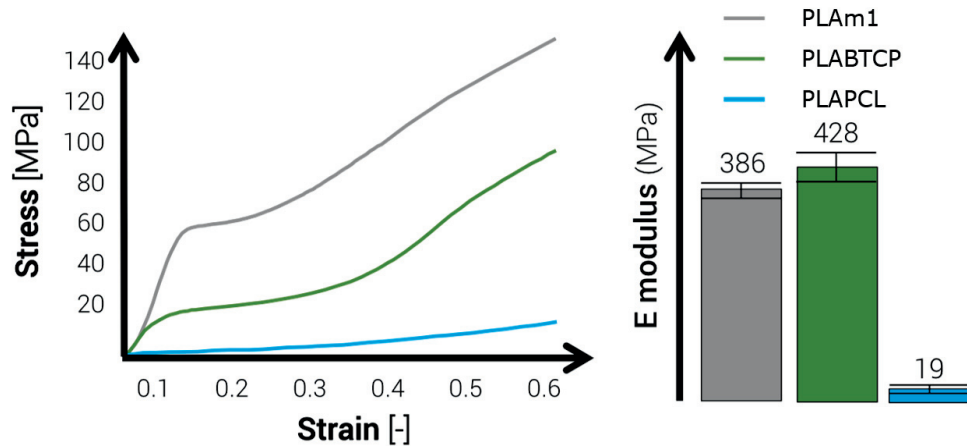


Figure 5.9 Comparison of PLAm1, composite PLABTCP and PLAPCL 3D printed structured compressive response in air.

Table 7 Young's modulus comparison of unconfined tests PLA, PLAPCL and composite PLLA scaffolds in air and PBS

MODULUS [MPa]		PLAm1	PLAPCL	PLABTCP
Mono Material Scaffold	AIR	386.2	19.2	428.4
	PBS	603.5	61.5	438.1

The increased Young's modulus from air to PBS was observed for all the material tested. The composite PLABTCP is the only scaffold expressing no significant changes in mechanical response while being tested in the different media. The soft blend PLAPCL shows the highest increase in Young's modulus, tripling the value in PBS. This behaviour might be explained by the hydrostatic effect of the PBS during compression. A cellular material saturated with a fluid shows two responses under compression: the response of the structure to the load and the response of the fluid. If the compression speed is high enough to do not allow the steady flow of the fluid out of the cellular structure, part of the load is taken by the fluid. This effect is called "hydrostatic effect". In these 3D printed structures, the hydrostatic effect is due to the water infiltration inside of the macro-porosity, which is slowly forced by the compressive load outside cellular material, generating an additional resistance to compression. This further compressive resistance offered by the flowing PBS outside of the 3D structure explains the sharped difference between the value collected in air and in PBS medium. The hydrostatic effect is particularly important in the cartilage, as it represents the capability of the tissue to retrain water is the principal responsible for the great mechanical properties under compression of such a thin tissue.

5.3.3 Fracture toughness at the interface of mono material structures

The mechanical properties of 3D printed structures strictly derive from the quality of the interlayers bonding interface. Understanding how the printing parameters effect the bonding strength between contiguous layers is therefore fundamental to improve the reproducibility and the overall mechanical properties of

FDM/FFF printed structures. This is particularly true for multi-material structures, where the printing parameters (e.g. temperature and speed) are few the controllable variables to improve the fusion bonding of the inter materials interface. In order to improve the mechanical properties of FDM/FFF printed parts, two approaches were followed. The first is the development of new materials tailored for this process, having superior characteristics compared to the conventional material adapted to this technology. The second is to investigate the influence of the process parameters during fabrication stage so that properties may improve. Literature reveals that this latter approach provides significant improvements, leading to the production of 3D printed specimen of superior quality^{185–188}.

As an attempt to assess the role of the printing parameters on interlayer fusion bonding, a study on the influence of printing temperature and speed on the quality of the layer-to-layer interface was performed. Different compact tension (CT) specimens were printed with two different orientations compared to the direction of the stress propagation, one at 0/90 ° and the second at 45 °. PLAm1 was used for this investigation. Tests were conducted as described in Chapter 3 to measure the toughness K_{Ic} . An example of the produce specimen from 3D model to 3D printed structure is shown in Figure 5.10

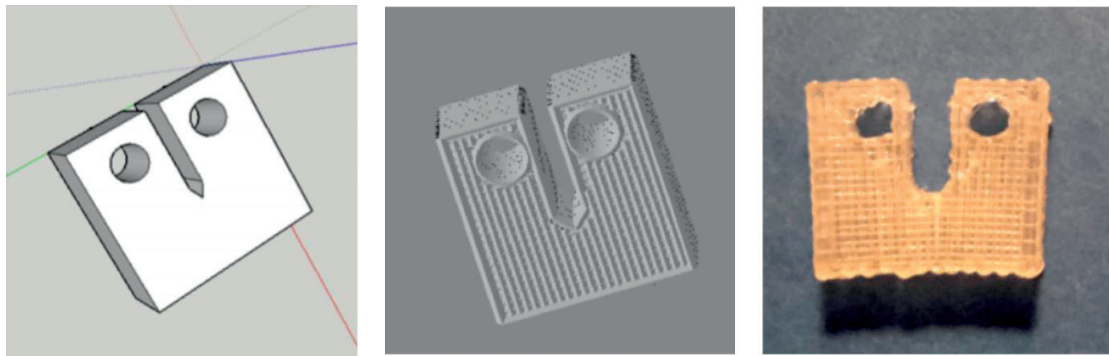


Figure 5.10 From 3D model to 3D printed structure. On the left, the 3D model obtained in Sketch up. The centre image shows the 3D model during the slicing phase, determining the layer configuration. The final 3D printed piece is shown on the right.

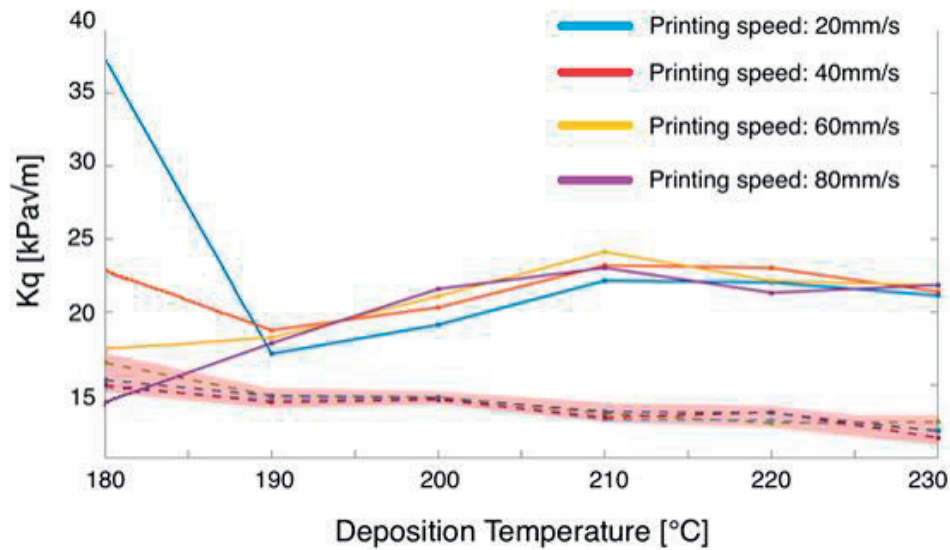


Figure 5.11 Influence of printing parameters (deposition temperature and printing speed) on the crack propagation in two different directions (0/90 and 45 °). On the y axis, K_q represents the energy required to propagate a fracture in the structure. On the x axis, the process temperature at which the specimens were 3D printed. Different colors were used to differentiate the speeds at which the samples were 3D printed.

Figure 5.11 shows the response K_q in function of the temperature of deposition (y axe) at a given printing speed. As expected, a significant different was found between the 45° (white background) and 0/90° (red background) configurations. With the 45° configuration, the layer disposition offers a higher resistance to the crack propagation due to the geometrical organization, while in the latter case half of the layers offer low resistance. An example of crack propagation for a 0/90° configuration is shown in Figure 5.12.

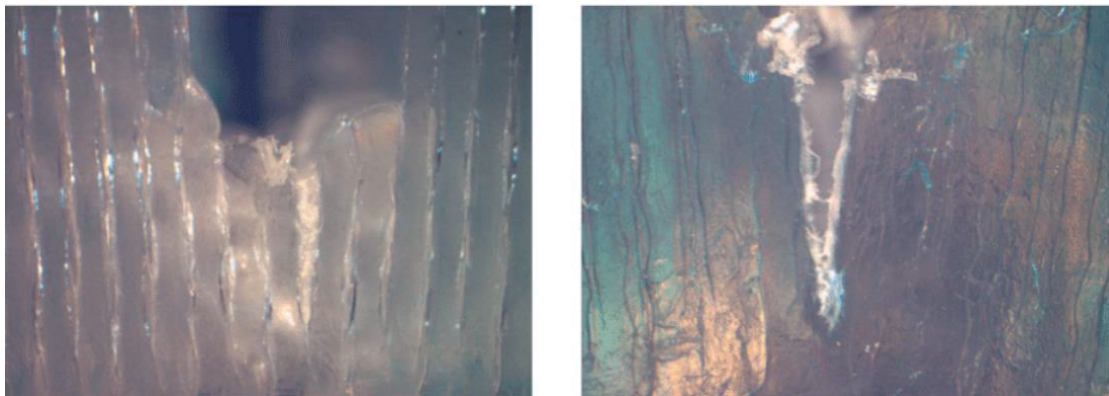


Figure 5.12 Example of crack propagation in a 0/90° configuration of PLAm1 3D printed CT specimen.

No significant differences were observed between different printing speed with the 0/90° orientation, which is stable between 16 and 13 $\text{kPa}\sqrt{\text{m}}$. An effect of printing speed is observed at low temperature, where K_q is decreasing with higher printing speed (from 36 $\text{kPa}\sqrt{\text{m}}$ at 20mm/s to 14 $\text{kPa}\sqrt{\text{m}}$ at 80mm/s). This result is in good agreement with what is expected from the physical modelling of the phenomenon. Fusion bonding

includes phenomena as intimate contact and molecular interdiffusion¹⁸⁹, which are time-temperature dependant. At low temperature, the two layers are required to stay in contact for a longer time to consolidate the interface. As seen in Chapter 3, Poly(lactide) is normally printed at a minimum temperature of 180 °C. For temperatures below 190 °C it would be then required to reduce the printing speed to maximize the interlayer bonding strength. Overall, the best condition to print PLAm1 is at 210 °C, which happens to be the temperature indicated by filament manufacturers for Poly(lactide) printing. The printing speed has then an influence on the interface, even though the maximum value for bulk PLA produced with high-pressure processes is far from the best Kq value found here (about 0.1 MPa \sqrt{m} vs 36 kPa \sqrt{m}). The impossibility to reach the maximum Kq value is an intrinsic limitation of FDM/FFF when compared to high pressure manufacturing methods, as compression molding. Among all the processing parameters, bonding strength of the material is function of the working pressure¹⁹⁰. While conventional manufacturing technologies offer the possibility to control such processing pressure, FDM/FFF offers poor control on this parameter. As a matter of fact, the pressure developed at the nozzle tip during the deposition of a molten layer is a fraction of the pressure built in methods as compression molding. This strongly limits the possibility to avoid the formation of a porosity at the interface between two continuous layers, jeopardising the bonding strength. Another limitation is the temperature profile of two continuous layers. FDM/FFF is a non-isothermal process, as the material starts cooling to room temperature as it is extruded from the nozzle tip. Nozzle temperature, fan cooling rate and ambient temperature determine the temperature at which the first layer will be when a second one will be deposited to bond together. The strength of this bond will be determined by the temperature of both layers, as they will contribute to the molecular interdiffusion at the interface. High molecular interdiffusion will be promoted by high interface temperature, producing elevated bonding strength. FDM/FFF offers poor control over layers' temperature, being able only to control the extruded temperature and the ambient temperature (e.g. by using 3D printers with a heated chamber or, less effective, with a heated bed). In conventional manufacturing methods, the molten polymer has a homogeneous temperature during the process, maximizing therefore the molecular interdiffusion during the consolidation phase.

As described in Chapter 4, homothetic foaming conditions will be applied to such 3D printed structure. Even though the maximum bonding strength reached by FDM/FFF during this analysis was about 1/3 of the maximum Poly(lactide) reported value in literature, the foaming step will help consolidating the interlayer fusion bonding. During homothetic foaming, the 3D structure is not molten, but has a temperature above the glass transition temperature (T_g). This temperature can be considered homogeneously distributed in the vessel volume, allowing to conclude that the material is homogeneously heated at this processing temperature. This first phenomena will help consolidating the 3D printed structure interfaces. Moreover, the expansion induced by the creation of a micro porosity within the bulk printed strands will increase the interlayer pressure during this consolidation phase, improving the bond strength at the interfaces while foaming the material. While being an important remark for single material structures, these two phenomena are fundamental to build a strong interface in multi-material structures where only one material is foamed.

5.4 Multi material scaffolds

The obtained multi material printed scaffolds for the different combinations listed in Table 6 are displayed in Figure 5.13. As for the single layer scaffolds, satisfying printing quality was achieved. All the printed scaffolds showed good model fidelity compared to the 3D model and 100% interconnected porosity.

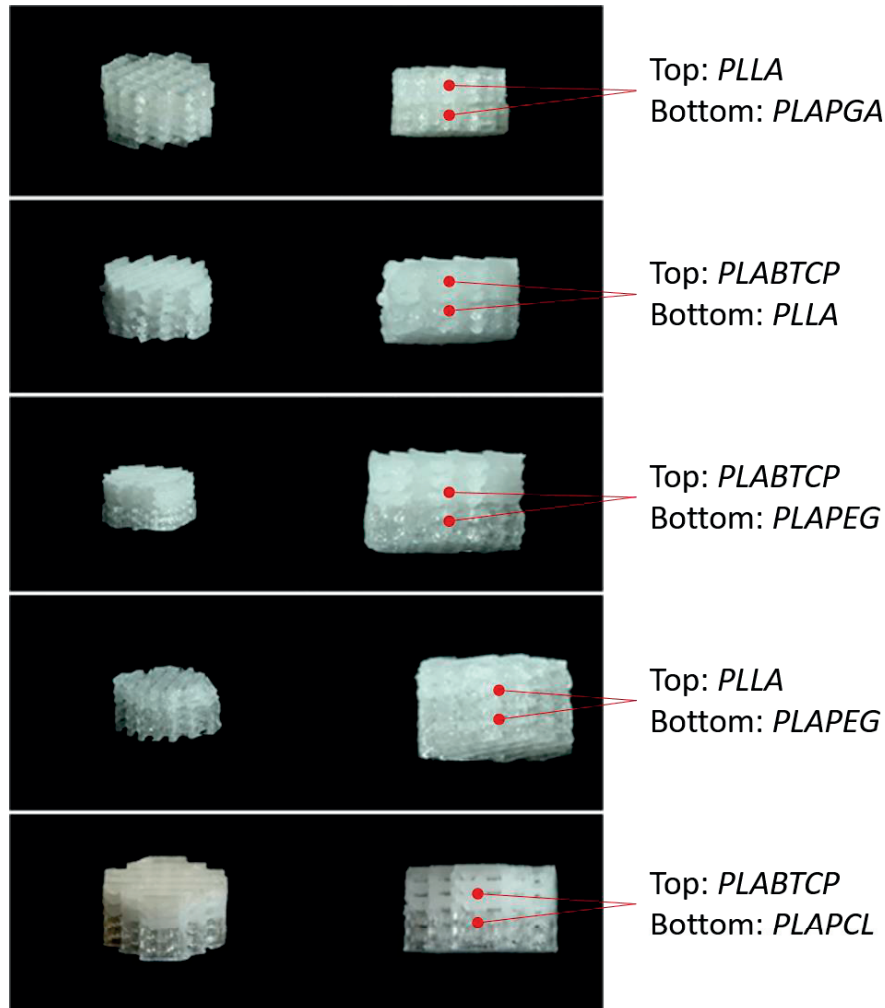


Figure 5.13 Multi material printed scaffolds at $T_{\text{print}} = 220\text{ }^{\circ}\text{C}$.

Microscope analysis has also permitted to study the dispersion of the β -TCP ceramic particles in PLABTCP composite filament and printed scaffold. Figure 5.14 shows that the ceramic particles diameter range is between 2 and 10 μm . The obtained processing conditions for the extrusion of the filaments and for their deposition allow to disperse and even improve the distribution of particle during the induced shear flows.

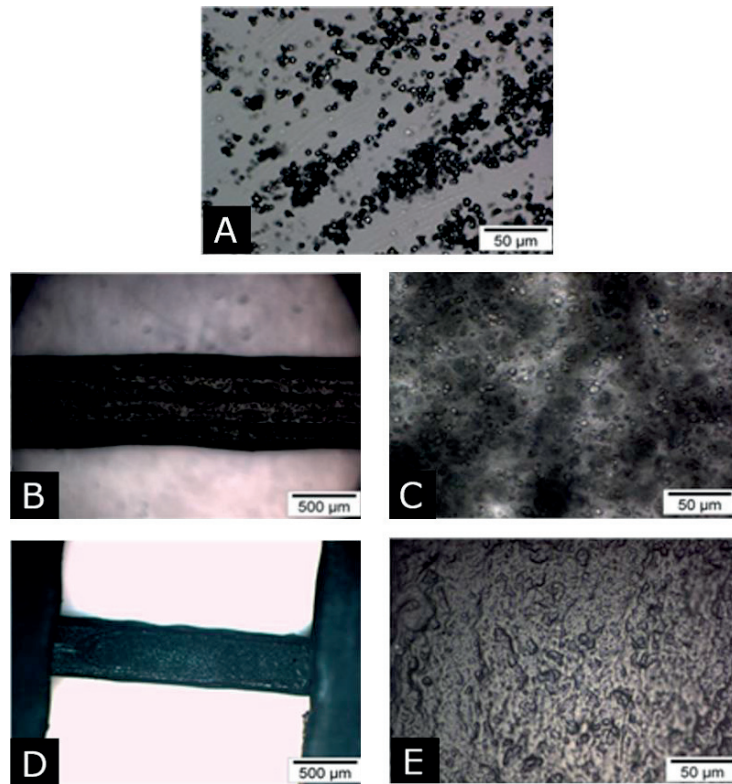


Figure 5.14 (A) β -TCP ceramic particles, (B), (C): dispersion of β -TCP ceramic particles within the PLABTCP composite filament; (D), (E) within the PLABTCP 3D printed scaffold.

As demonstrated in the previous paragraph it is now possible to produce medical filaments to deposit them by a FDM 3D printer. A test batch of PLAPCL and PLABTCP was produced in form of such a filament, printed and foamed subsequently to create a 3D structure. The structure was cut in half and analysed by SEM to investigate the quality of the interface between the two materials. Figure 5.15 shows a schematic of the approach.

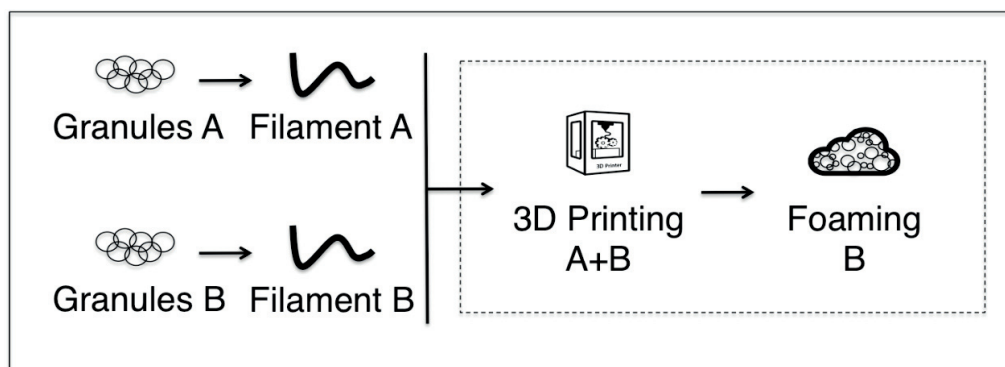


Figure 5.15 Schematic of the process to create a multi material composed by a 3D printed structure and a 3D printed and foamed structure.

The produce material shows a good resistance to shear stress while being manipulated, without signs of delamination. The interface is clearly visible and remarks sharply the boundary between the two materials (Figure 5.16). The print is net, without sign of imperfection due to an inconstant filament diameter.

SEM analysis from the top confirms the printing quality, with the cell walls of well-spaced and with a constant beam diameter. Looking at the interface from the inside of the structure no sign of defects is visible between the materials. The printing windows of the two materials are compatible and printing multi-material structures was thus achieved.

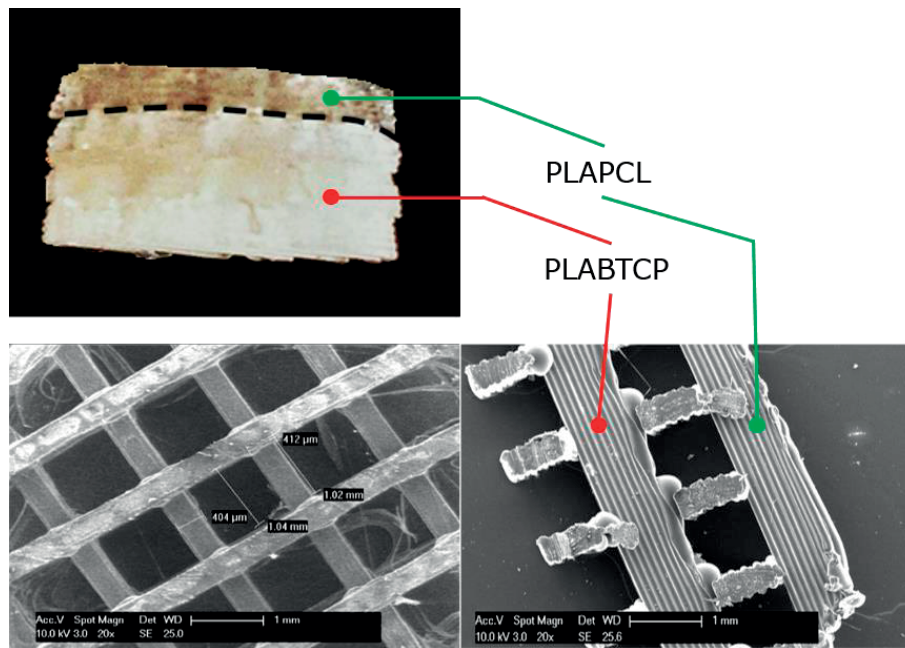


Figure 5.16 Multi material scaffold printed from PLAPCL and PLABTCP. SEM pictures from above and the side are shown. No evidence of macroscopically differences is appreciable, sign of the good integration between the materials and its blend.

Multi-material structures were tested under the same conditions shown in the previous paragraph for single material scaffolds. The mechanical response of the multi material scaffold was then compared to the one of the single materials to show the influence of such a structure on the mechanical response in uniaxial compression.

Three multi material scaffolds were produced from the combination of the three materials, but only the PLAPCL-PLABTCP was selected for the final application (Figure 5.17).

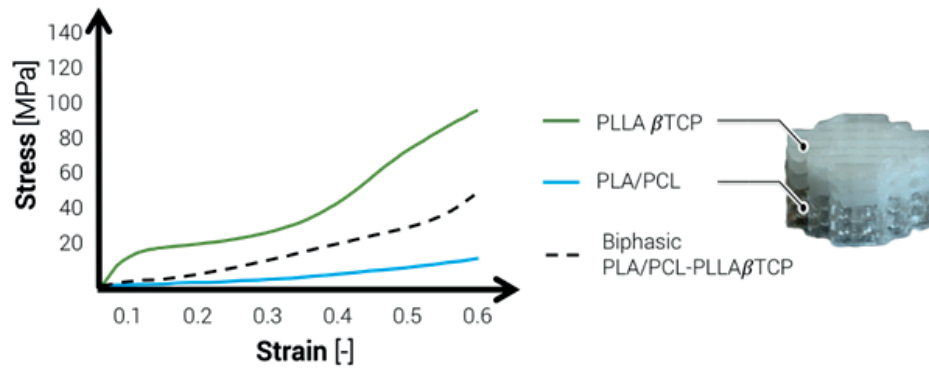


Figure 5.17 Compression response of PLAPCL-PLABTCP structures in unconfined compression in air.

The multi material scaffold response fits the expected region between the lower and upper range delimited by the neat materials. The mechanical behaviour is similar to the one observed with PLAPCL scaffolds, where the elastic linear region is hidden by buckling effects from the beginning of the test. The average Young's modulus was calculated to be about 108 MPa for a 50:50 Multi material scaffold. From the curve in Figure 5.17, it is possible to extrapolate the behaviour of PLAPCL-PLABTCP multi-material structures under compression. At low strains, the influence of the PLAPCL dominates. All the stress is transferred to the softer region of the multi-material structure, represented by the PLAPCL layers. This soft layers start deforming, with a densification of the porous areas like explain in chapter 4, up to a critical value, at which the stress is progressively transferred to the stiffer layers of the structure, represented by the PLABTCP. At high strains, the PLABTCP response dominates, as observed by the sharp increase between 0.25 and 0.3 strain. This observation reflects the 50:50 ratio of PLAPCL and PLABTCP in the multi-material structure. For structure with a higher amount of PLAPCL (e.g. 80:20), it is expected to see an overall softening of the multi-material structure, resulting in a stiffness closed to the value of pure PLAPCL. Moreover, such a structure would show a compressive response similar to the PLAPCL curve, with a slope gently westwarding, without signs of loss of the macro-pores. by densification. A multi-material structure more imprinted towards stiff materials, as a ratio 10:80 of PLAPCL and PLABTCP, would present a shorter elastic region, followed by a more accentuated plateau. Densification would appear at lower strains as compared to a 80:20 structure where the PLAPCL deforms at first and progressively.

5.5 Multi material foamed scaffolds

The process of foaming a 3D printed structure to obtain a macro and micro porosity, explained in Chapter 4, can be applied to a multi-material structure to produce a dual porosity. In particular, the multi material structure could be designed to exploit the low temperature foaming processing window to induce porosity only in one of the two materials (Figure 5.18). This would lead to an interpenetration of the foamed material in the second thermoplastic phase, enhancing the interface between the two.

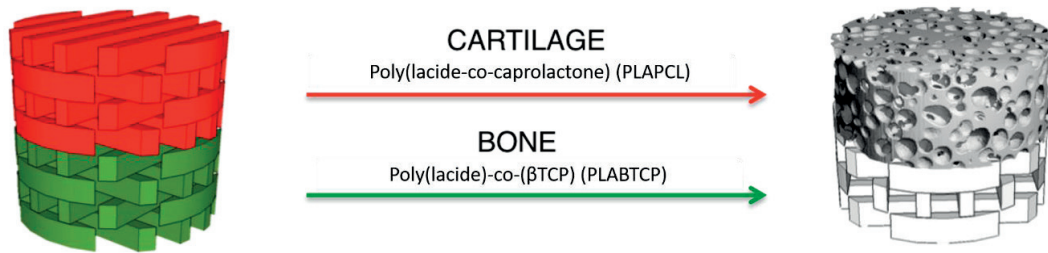


Figure 5.18 Schematic of the approach to produce a multi material multi-porosity cellular material. A 3D structure composed of two different materials (top red for cartilage and bottom green for bone) is printed (left) and foamed at process conditions that allow only one material to foam.

PLAPCL was chosen as the ideal candidate to extend the study on this selective foaming. As discussed in paragraph 5.2.1 PLAPCL is the softest medical grade filament. Table 8 shows the investigated processing conditions.

Table 8 PLAPCL conditions tested to produce homothetic foaming from a 3D printed biomaterial template.

Sample ID	Temperature [°C]	Pression [bar]	Saturation t [min]	dP/dt [bar/s]
1	125	150	60	50
2	125	180	5	50
3	130	180	5	50
4	135	180	5	50
5	135	185	5	50
6	135	180	5	60
7	125	180	5	0.1
8	135	180	5	0.1
9	125	180	5	0.1
10	135	180	60	0.1
11	135	180	60	0.1
12	135	180	5	60

A processing window was determined from the best foaming conditions in relation to the final obtained morphology, as shown in Figure 5.19. The red area shows all the pair of temperatures and pressure at which homothetic foaming does not occur. This is explained by the low concentration of CO₂ in the material, an excessive high temperature melting the 3D geometry or an excessive pressure preventing the foaming to happen. The yellow area represents all the sets of parameters at which the foaming occurs, but the 3D structure does not respect the original 3D shape. This is due to the same phenomena described for the red area and it is considered as a transition zone to better samples. Also, defects in this region may involve porosity occlusion due to strand collapse and partial foaming of a wide area of the structure. The black and white strips area represents the conditions at which homothetic foaming occurs, but some minor defects are still observable. These may include local deformations and partial foaming of a minor area. Finally, the green area

represents the conditions at which homothetic foaming occurs and it shows reproducible results (e.g. homogeneously foamed samples were obtained on an average of $n=3$ samples). The processing windows can be explained also referring to the result of Chapter 4 for PLAm1. A low saturation temperature is required to keep the 3D printed structure without melting the geometry. Above 135 °C, saturation time higher than 1 minute induces a partial or total melting of the structure and are therefore rejected. Temperatures lower than 110 °C can be rejected as well, as they do not allow the mobilization of PLAPCL chains, preventing CO₂ diffusion within the 3D structure and the foaming. The saturation pressure is responsible of CO₂ diffusion within the polymer. In batch foaming, a high pressure is desirable to increase the carbon dioxide absorption, promoting cell nucleation. However, it was observed that without maintaining a proportion between pressure and temperature, the increase of saturation pressure induces the 3D structure to collapse. This might be explained by the plasticiser effect of carbon dioxide on Poly(lactide) materials: the higher the content of CO₂ in the polymer matrix, the lower will be the glass transition temperature (T_g) and the polymer viscosity. This effect might therefore soften the cellular structure to the collapse point, producing similar effects as a high saturation temperature. Increasing the temperature with the saturation pressure helps promoting cell nucleation and growth, creating thus a counter force to balance the collapsing behaviour. A high depressurization rate is required to increase foam expansion and pore size. This information has been already reported for batch foaming³⁹, but the influence of this parameter is crucial in homothetic foaming. Low depressurization rates do not produce any foaming, leaving a non-homogenous structure as demonstrate by SEM analysis on PLAm1 in Chapter 4. For PLAPCL, depressurization rates above 40 bar/s are required to produce a well homogeneous structure.

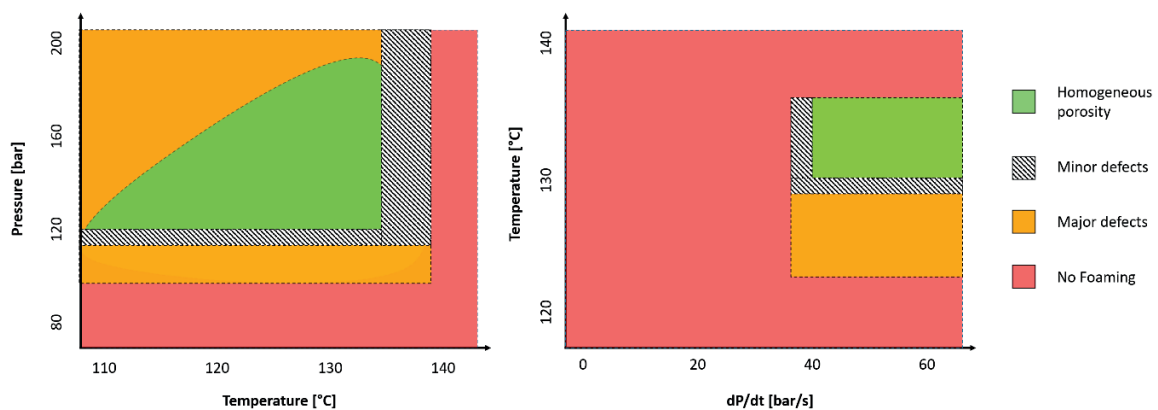


Figure 5.19 Processing windows for PLAPCL scaffold to produce a micro porosity from 3D templates.

The application of the seen foaming conditions to multi material PLAPCL-PLABTCP scaffold led to the production of hard and soft multi-material scaffold with a controlled macro/micro porosity, as shown in Figure 5.20 and Figure 5.21.

The influence of depressurization and saturation time is shown in Figure 5.20 and Figure 5.21. A longer saturation time allow more time to the carbon dioxide to saturate the structure, increase the CO₂ content in the matrix. Given a high depressurization rate, the structure will expand more, producing defects and deforming the macro porosity.

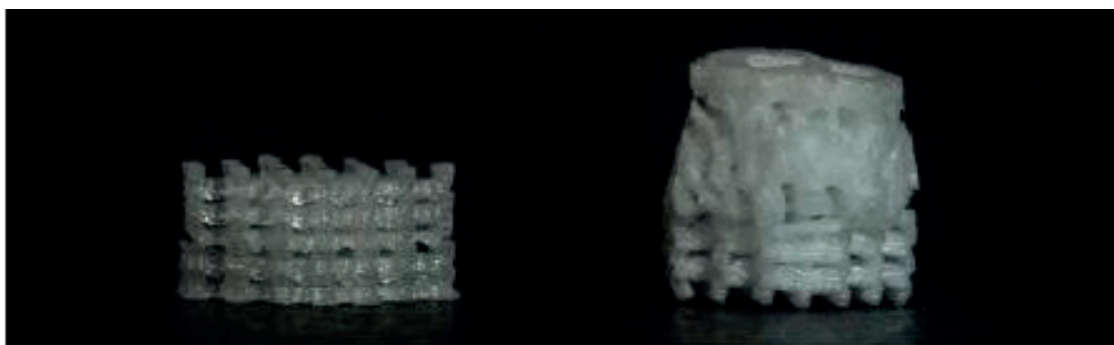


Figure 5.20 Example of foamed multi material scaffold (right) from a 3D printed template (left) with selective foaming of one material (condition 6 Table 8).

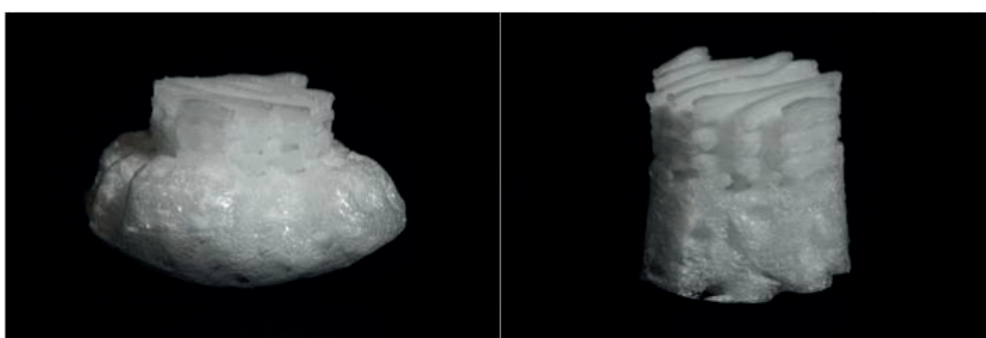


Figure 5.21 Example of material expansion in multi-material scaffold during selective foaming (condition 6 Table 8).

5.5.1 Mechanical properties of 3D printed and foamed multi material scaffolds

Finally, mechanical properties in compression were compared with the literature value of aggregate modulus of articular cartilage and average the Young's modulus measured on human articular cartilage in Chapter 2, as shown in Figure 5.22. The neat solid PLAPCL with a Young's Modulus assessed at 1 GPa from the literature¹⁹¹, was processed at first into a multi material cellular structure with a PLABTCP by FDM/FFF, as previously described in this chapter. The average porosity determined from the CAD model and compared with the printed structure was about 66%, with a Young's Modulus of about 90 MPa. The decrease of stiffness from the neat material to the cellular structure derives from the porous nature of the geometry, as described by the Gibson-Ashby model described in Chapter 2. This 3D model was determined after the mechanical testing of mono material and multi-material structures in Chapter 4 and previously in this chapter. The processing windows of PLABTCP and PLAPCL homothetic foaming (Figure 5.19) were compared to find a third processing window to process the PLAPCL layers without foaming the PLABTCP. Given the lower melting temperature of the PLAPCL ($T_m \approx 160^\circ\text{C}$) compared to the melting temperature of the PLABTCP ($T_m \approx 180^\circ\text{C}$), it was possible to process the multi material 3D printed scaffold into a foamed multi material scaffold. The compressive modulus reported in Figure 5.22 was obtained by foaming the PLAPCL-PLABTCP scaffold at 120°C , 170 bar, 5min and 60 dP/dt. The Young's Modulus of this structure is about 2.44 MPa. As demonstrated in Chapter 4 for PLAm1, homothetic foaming increases the overall structure porosity by foaming the bulk beams composing the 3D printed cellular structure. This increase of porosity induces a decrease of density, therefore decreasing the overall structure stiffness. A multi porous material with macro porosity in the PLABTCP layers (defined by the FDM/FFF) and a macro and micro porosity in the PLAPCL layers

(defined by the FDM/FFF and homothetic foaming of the structure) is produced as result, with a stiffness reduced by about 100 times the value of the neat polymer.

From the processing window of PLAPCL, shown in Figure 5.19, multi-material structures with different stiffness were obtained by tuning the foaming parameters. In particular, three PLAPCL/PLABTCP structures were selected as representing of the average low, medium and high induced microporosity. All the PLAPCL scaffolds were design to have 4 mm thickness after foaming, but different geometries are achievable to meet the desired scaffold thickness, up to a minimum of 0.4 mm. The minimum PLAPCL scaffold thickness is limited by the number of layers constituting the structure, corresponding to two of about 0.1 mm thickness. Under this condition, a minimum of two layers per beam is deposited, providing sufficient mechanical stability and stiffness to be safely handled.

The compressive response of the foamed PLAPCL/PLABTCP structures were then compared with the value of the cartilage aggregate modulus from the state of the art and the gradient stiffness measuremeasured by nanoindentation. The aggregate modulus represents the extra cellular matrix response of the articular cartilage to compression, e.g. without the influence of hydrostatic forces. As shown in Figure 5.22, the three multi-material structures fall in the range of the cartilage modulus reported from literature (references in Table 2, Chapter 2).

These results show the range of mechanical properties achievable by tuning the micro and macro porosity, processing structures with stiffness comparable with the gradient properties of the three layers composing the articular cartilage. Three values were reported for the structures: 2.44 MPa, 4.23 MPa and 11.03 MPa. The original 3D printed structures shown a range of stiffness from 24 MPa (PLAPCL 90-10 PLABTPPLABTCP) to 394 MPa (PLAPCL 10-90 PLABTCP). By tuning the ratio of PLAPCL-PLABTCP, the geometry of the 3D printed structure (e.g. strands thickness, pore size, layer orientation, layer thickness, porosity) and the foaming conditions a variety of structures with average stiffness between 2.44 MPa (highest foaming porosity) to 11.03 MPA (lowest foaming porosity) could therefore be obtained.

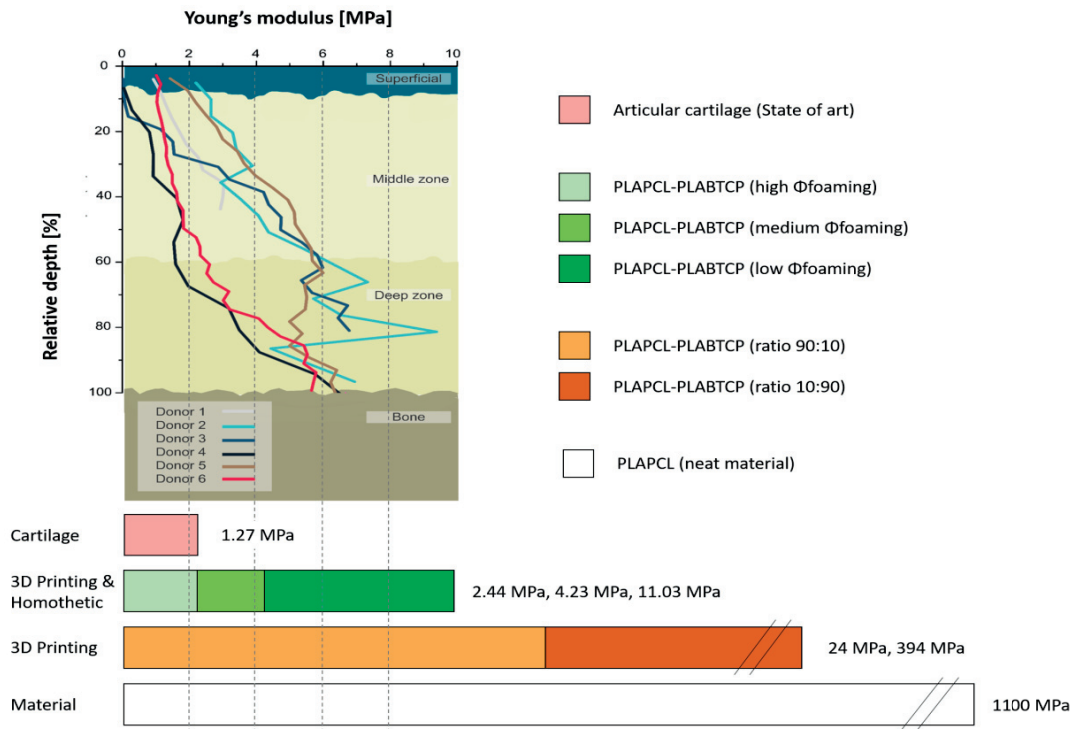


Figure 5.22 Schematic of the stiffness of the multi-material structures obtained by homothetic foaming compared to the 3D printed structures and articular cartilage. Articular cartilage Young's modulus was obtained from literature (references in Table 1). Φ foaming indicates the microporosity induced by the foaming of the PLAPCL layers, as described in Table 1. The ratio of PLAPCL and PLABTCP shows the proportion of the two materials in the multi-material structure.

5.6 Conclusions

This chapter described how homothetic foaming, presented in Chapter 4 for a neat Poly(lactide), could be applied to process 3D printed multi-material structures into hierarchical micro/macro porous cellular structures. In particular, the homothetic foaming was demonstrated to be tunable to achieve different mechanical properties, mimicking the local stiffness of the articular cartilage measured in Chapter 2.

In order to understand the influence of the printing parameters on their fracture toughness, effect of printing temperature and speed were investigated by mean of a compact tension test (CT). While the first orientations showed no significant differences while varying the printing parameters, the second showed higher fracture toughness and a tendency to increase the toughness while decreasing the printing speed at low temperature. Indeed, the slower the deposition of the filament the better the heat transfer for non-isothermal local fusion bonding and higher fracture toughness. These results were therefore exploited to better control the 3D printing of cellular structures selected for further testing.

Different medical grade of neat polymers were processed into 1.75 mm filaments for FDM/FFF machines (details in Annex II). Three classes of filaments were produced: neat polymers (PLAm1, PLLA), copolymers (PLAPCL, PLAPGA) and blends (PLAPEG, PLABTCP). These filaments were 3D printed into cellular structures and then PLABTCP and PLAPCL were considered for further analysis. The average stiffness of such geometries was assessed by unconfined uniaxial compression testing in air and PBS. PLAm1 and PLAPCL showed a sharp increase in stiffness when tested in different medium. In particular, they expressed a higher stiffness in PBS,

which was hypothesized to be related to the hydrostatic effect of the PBS flowing out of the macro-porosity in the 3D cellular structure. PLAPCL structures' average stiffness of 19.2 MPa showed to be still far from the target range of value of 0.01 – 10 MPa of the articular cartilage. The principal limitations, represented by the Young's modulus of the neat material and the maximum porosity achievable by 3D printing, were targeted by adding a further step of homothetic foaming.

PLAPCL and PLABTCP were printed in a 50:50 multi-material structure to mimick the cartilage and bone layers composing the osteochondral tissue. The average stiffness of such 3D printed structure was assested at 108 MPa. This value falls within the range of the two neat materials of 19.2 MPa and 428.4 MPa as expected. Interestingly, the deformation under load of such a structure was observed to be dominated by two different phenomena. At first, the load is withstood by the PLAPCL, inducing a deformation in the softest region of the multi-material structure. The yield point observable in Figure 5.7 for the PLABTCP structure is no longer distinguishable from the buckling region. This phenomenon is due to the progressive deformation of the PLAPCL strands and consequent progressive densification of the macro-porosity in the softest region of the multi-material structure. PLAPCL densification continues up to a given stress value, observed slightly above 20 MPa, at which the stress begins to be transmitted to the PLABTCP layers. At this point, the measured stress in the multi-material structure follows the PLABTCP slope previously observed for the mono-material structure.

PLAPCL layers in the 50:50 multi-material structure were successfully foamed into three different range of induced micro-porosity, showing an average stiffness of respectively 2.44 MPa, 4.23 MPa and 11.03 MPa. By tuning pressure, temperature and the depressurization rate as discussed in Chapter 4 it was possible to control the homothetic foaming for PLAPCL. Moreover, by processing a multi-material structure of PLAPCL-PLABTCP to selectively foam only one material (PLAPCL) the advantage of homothetic foaming was demonstrated.

Compared with other manufacturing technology, homothetic foaming was able to meet the original objective of this thesis to mimic the articular cartilage local stiffness with a polymer hierarchical cellular structure. In particular, this was possible applying homothetic foaming to a 3D printed multi material PLAPCL-PLABTCP structure. This scaffold represents therefore a good candidate for osteochondral repair. Further biological tests will be required for the final application and will be described in Annex I.

Chapter 6 3D Foam Printing

6.1 Introduction

Hierarchical cellular structures have been successfully produced by different methods¹⁹, including homothetic foaming as described in Chapter 4 and Chapter 5. A key feature that is still missing in all these approaches is the possibility to shape the desired cellular structure into an object with a complex 3D structure. Homothetic foaming was developed to fill this gap, combining Fused Deposition Modelling / Fused Filament Fabrication with Supercritical carbon dioxide Foaming to offer a better control over the structure 3D geometry, the macro porosity (1 – 0.2 mm) and the micro porosity (0.1 – 0.01 mm). The natural evolution of this technique is the integration of all the processing steps in a single process. This would simplify the current processing of such hierarchical cellular structures.

This chapter will describe how to produce hierarchical cellular structures by 3D printing of cellular micro porous polymer strands into a macro porous object with a controlled shape. 3D foam printing (abbreviated in 3DFP) principle is straightforward: a thermoplastic material is saturated with carbon dioxide (CO₂), which is therefore released during the deposition phase, creating a porous strand. This technology is a step forward from the homothetic foaming shown in Chapter 4, as it introduces a higher degree of design freedom by controlling the strands micro porosity online during the deposition. At first, the principle of 3D foam printing will be investigated, considering the deposition of porous strands with a model Poly(lactide) material. Two levels of insight will be given: how to control filament saturation achieving the desired concentration of CO₂ and the correlation between printing parameters (e.g. nozzle temperature and printing speed) with strand porosity and pores morphology. The influence of the saturation conditions on the CO₂ content in the filament will be studied. Then, the work will focus on the possibility to control the processing parameters to tune the micro porous strands structure. In particular, the influence of printing speed and temperature on strand foam expansion, porosity and pore morphology will be investigated. Finally, the possibility to apply 3D foam printing on medical materials will be evaluated, showing how to apply the knowledge acquired on the model material to process hierarchical cellular structures with polymer and composite materials.

6.2 Materials and methods

6.2.1 Material selection

Commercial PLAm1 filaments, diameter 1.75 mm, were bought from TreeD Filaments. PLAPCL and PLABTCP filaments were produced in-house with a Noztek Extruder as described in Annex II.

6.2.2 Filament saturation

A high temperature high pressure autoclave described in Chapter 3 was used to saturate the filaments. Prior to the saturation, each filament was dried at 90°C for 8h. Filaments were kept at a constant temperature, ranging from 25 to 120 °C, and constant pressure, ranging from 50 to 150 bars, for a given saturation time (from 1 to 24 hours) to induce the diffusion of carbon dioxide into the filaments. The vessel was then depressurized to 1bar at different rates (from 0.1bar/s to 70bar/s).

The content of CO₂ (%wCO₂) diffused into the filaments was determined by a precision scale, weighting the filaments before and after the saturation phase (resolution 1mg).

The %wCO₂ was measured by

$$\%wCO_2 = \frac{w_{sat} - w}{w} \quad (10)$$

where w_{sat} is the weight of the saturated filament immediately after the process and w is the weight of the same filament prior the saturation.

6.2.3 Printing 3D foams

All saturated filaments were extruded by a Markebot Replicator 2, using a 1mm nozzle size, at extrusion speed from 10 to 100 mm/s and hot-end temperature from 180 to 250°C. All the parameters were monitored by ReplicatorG.

6.2.4 Strands expansion and porosity

Foam morphologies were investigated by scanning electron microscopy (SEM, Philips Xlf-30). Specimens were sliced and therefore coated with a 20nm thick carbon layer using a carbon coater (Cressington Carbon Coater 108 carbon).

Strands expansion rate from the expected diameter (set as the nozzle size) was determined from precision calliper measurements and image comparison at Image J ^{192–194}.

6.2.5 Mechanical properties

Strands mechanical properties were measured by indentation tests by an instrumental indenter (Ultra Nanoindenter Tester™ from Anton Paar, Peseux, Switzerland). All indentation tests were performed in displacement control mode using a Berkovich indenter tip (ø 500 µm) made of ruby. The maximum displacement of 100 µm was attained at a displacement rate of 120 µm/min. The loading was followed by a 30 s hold-time and an unloading phase at 120 µm/min. On each strand, six indentations were performed. The first line of indentation was performed every 300 µm along the longitudinal axe, while the second line of measurements was performed parallel to the first at a distance of 200 µm.

The mechanical modelling values were obtained applying the Gibson-Ashby model described in Chapter 3, equation 2 and 3. The strand density was measured by weighting the samples by a precision scale and calculating the average volume by measuring strand diameter with a precision calliper. Each strand was cut to a fixed length of 10 mm.

6.3 Results

A schematic of the approach followed to saturate the FDM/FFF filaments with carbon dioxide and deposit porous strands into a 3D object is described in Figure 6.1. The process consists in two phases: filament saturation and printing. During the filament saturation, a 1.75 mm filament is positioned in the autoclave vessel and exposed to a pressure-temperature cycle to allow the carbon dioxide diffusing in the material. Low temperature and depressurization rates were adopted to prevent unwanted filament foaming during this stage of the process. At the end of the cycle, the %wtCO₂ present in the filament was quantified. In the second phase, the filament was fed into a FDM/FFF machine. The heat transfer from the hot-end of the 3D printer induces the cells growth and nucleation of the CO₂ in the molten polymer, as described in Chapter 3 for batch supercritical foaming. A porous strand is therefore produced at the nozzle exit as result of the process.

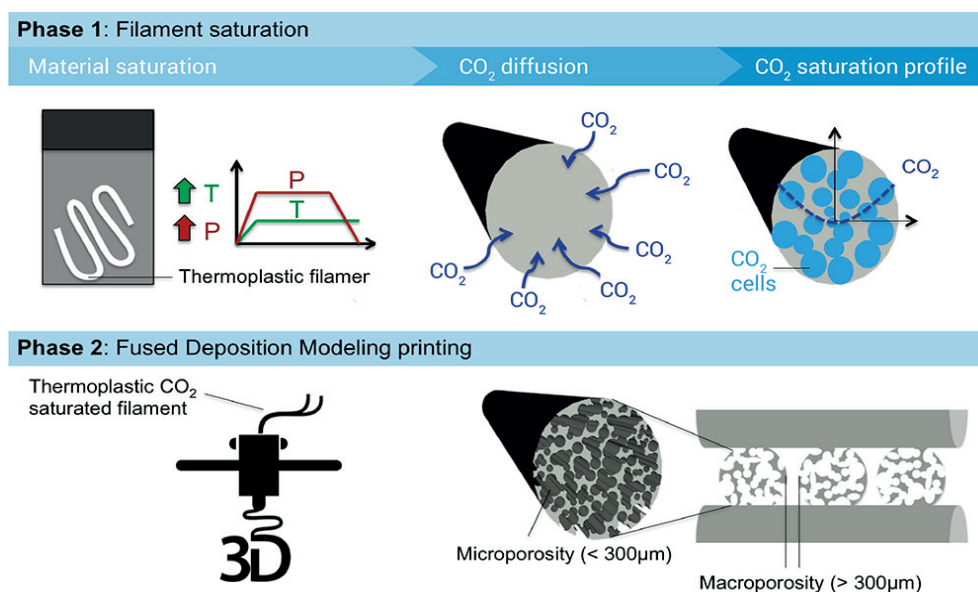


Figure 6.1 Schematic of the approach to produce 3D printed foams. The process starts by a gas saturation step of a thermoplastic filament to induce CO₂ diffusion into the material (Phase 1). During a 3D additive manufacturing process such as the Fused Deposition Modelling (FDM) the filament is deposited in smaller strands (from 0.4 to 2 mm). Spacing the strands during the deposition a macro porosity (0.4 to 10 mm) is created. Additionally, CO₂ nucleate and escape from the strands, leaving a controlled micro porosity (1 µm to 300 µm) during the printing.

6.3.1 Filament saturation

Table 9 illustrates the different conditions investigated to optimize filaments saturation and foaming. Influence of CO₂ states (gas, liquid and supercritical) was tested in different combinations. The best processing condition to maximise the carbon dioxide content was having CO₂ at gaseous state, leaving the filaments saturating for about 2 hours at 10 °C and 45 bars. In the optic to apply the saturation step priori to printing in an ad-hoc machine, the minimum saturation time is required while maximizing the CO₂ content. Saturating the filament at 60 °C for 5 minutes, at a pressure of 80 bars showed a very similar CO₂ tenor in the material, also being a good candidate to shorten the saturation phase. Liquid CO₂ at 10 °C, 79bars left saturating for 10 minutes gave excellent results as well, producing a CO₂ tenor of about 20 %. We decided to proceed with liquid CO₂, in the optics to reduce as much as possible the processing time, while keeping low temperature and low pressure.

Table 9 Influence of carbon dioxide phase on filament saturation at different processing conditions. Variation of the saturation temperature, pressure and time different carbon dioxide dissolution into a PLA 1.75mm filament was evaluated. The best conditions adopted were the ones maximizing the carbon dioxide content in the shortest time at the mildest possible conditions.

N° run	Temperature [°C]	Pressure [bar]	Sat. time [min]	CO ₂ phase	CO ₂ density [kg/m ³]	Saturation [%wt]
14	50	75	240	supercritical	195.60	5
6	25	70	60	liquid	700.95	8
9	25	40	5	gaz	93.63	8
5	25	60	5	gaz	258.40	9
7	25	70	60	liquid	700.95	9
2	25	70	60	liquid	700.95	10
3	60	80	60	supercritical	191.60	10
1	25	70	60	liquid	700.95	11
4	60	80	60	supercritical	191.60	11
13	40	70	30	gaz	198.00	11
11	60	65	30	liquid	737.50	13
18	10	55	10	liquid	875.10	14
15	10	45	120	gaz	135.09	17
12	25	65	45	liquid	737.50	18
8	25	70	30	liquid	700.95	19
17	10	68	10	liquid	890.82	20
10	60	80	5	supercritical	192.60	22
16	10	45	120	gaz	135.09	23

6.3.2 Strand expansion

Figure 6.2 gives a visual overview on the obtained results. At 250 °C and 200 °C strands diameter increases constantly from 2.13 mm ± 0.07 mm to 2.57 mm ± 0.07 mm with the increase of printing speed in the first case and from 1.79 mm ± 0.05 mm to 2.12 mm ± 0.06 mm in the latter. T-test indicates a statistical difference with $p < 0.01$. Interestingly, at 180 °C the positive trend switched to a negative correlation between temperature and printing speed, with the strands diameter decreasing from 1.84 mm ± 0.13 mm to 1.64 mm ± 0.06 mm. No statistical difference ($p > 0.1$) has been shown between printing at 10 mm/s at 180 °C (1.84 mm ± 0.13 mm) and at 200 °C (1.79 mm ± 0.05 mm). The negative correlation at 180 °C between strands diameter and printing speed can be explained by the heat exchange between the heating block and the material. At 180 °C the heat transfer to the polymer is insufficient to produce a large expansion rate, given the low chains mobility and thus a low cells growth leading to smaller pores. When increasing the printing speed, the material will experience a lower residence time in the heating block and thus an even lower growth of cells. Pore size and strands diameter decreased to the minimum value observed of 1.64 mm ± 0.06 mm. Viscosity, which has a minor influence here due to the insufficient heat transfer, has an important role to explain the strands diameter positive correlation with temperature and printing speed for heating temperature above 200 °C. As demonstrated by rheological analysis¹⁹⁵, material viscosity decreases exponentially with the increase of printing temperature and speed. High printing temperature leads also to a more uniform heat distribution experienced by the material in the heating block, allowing a fast cell growth and thus higher porosity and strands expansion during the depressurization at the exit of the nozzle. The same behaviour is shown for printing speed: PLA has well known shear-thinning properties, meaning that at higher shear stresses the viscosity will decrease. A decrease of viscosity, keeping constant nozzle diameter and temperature, is expected to lead to

an easier CO₂ nucleation and therefore higher expansion rate, as observed with the increase of strands diameter.

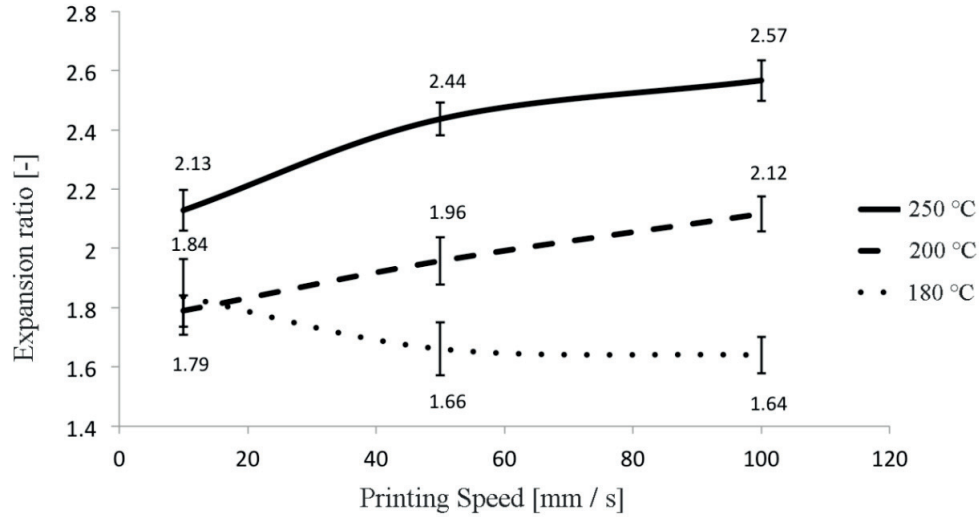


Figure 6.2 Influence of printing temperature and printing speed on strands expansion at the nozzle exit. Three temperatures were tested: low (180 °C), medium (200 °C), and high (250 °C). At 200 °C and 250 °C strands diameter and printing speed are positively correlated ($p < 0.01$). At 180 °C the heat transfer is insufficient to triggers pores growth, reducing strand expansion. T-test conducted with $n = 12$.

6.3.3 Pores morphology and porosity distribution

The cross- section of a non-saturated 3D printed filament is shown in Figure 6.3 for comparison. Influence of processing parameters, as extrusion temperature and speed on strand morphology and pores distribution, investigated in the range of 180 to 250 °C and from 10 to 100 mm/s, are shown in Figure 6.4. Nozzle size was set to 1 mm and CO₂ concentration to 14 %w, which represented an optimal saturation condition in terms of strand expansion, saturation time and temperature. On the left column (a, c, e, g) the overall morphologies are shown (scale bar 1 mm, scale bar 0.5 mm in image C), while on the right column (b, d, f, h) zooms at 200 μ m scale shows porosity distribution, typology (open/closed cells) and pore size.

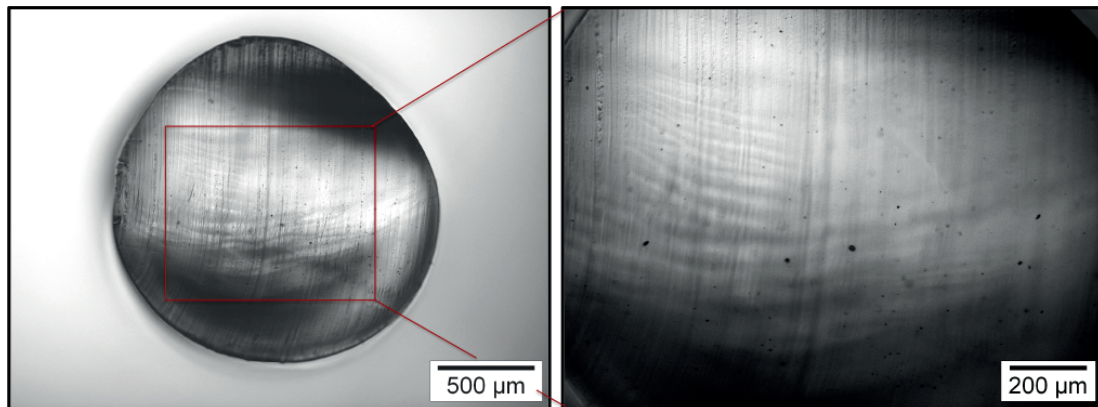


Figure 6.3 Strand cross-section of a non-saturated filament after printing. No porosity is observable after printing, due to the absence of CO₂ in the filament.

At 180 °C a core-shell structure is formed, with a well-defined skin at the surface of the strand of about 100 µm thickness with a sharp interface between the core porosity and the bulk shell.

As observed in polymer foaming, the heat transfer induces a rapid cooling of the outer skin even before development of pores or cells. This phenomenon is promoted as well by the high viscosity and low depressurization rate encountered here. At higher temperatures and subsequent lower polymer viscosity or/and higher depressurization rates of the other conditions the thick skin has disappeared. At this low temperature and deposition speed the average porosity in the core is 53.23 % with larger size pores close to the skin where the gas couldn't escape and thus promoted the growth of pores. With the increase of the extrusion rate to 100 mm/s, a higher depressurization induces a more homogenous nucleation of smaller pores everywhere through the section. A smoother gradient in porosity is observed with large cells at the centre to smaller cells with some open to the surrounding environment. Furthermore, the collapsing of cells at the centre generates a hollow-like structure with a continuous channel of about 300 µm diameter. Longitudinal flow can be considered with this type of hollow filament.

At 250 °C and 10 mm/s, the average porosity is 68.0 % and the pore size is reduced when compared to lower temperatures but the foaming expansion is larger. The temperature has reduced the viscosity offering a polymer state more favourable to homogeneous foaming. A well-defined porosity gradient is therefore formed, with pore size increasing gradually from the outer edge to the centre. The core of the strand showed to be more confined and less pore growth occurs, while in the outer volume of the filament large pore will offer higher diffusion paths. Increasing the extrusion rate at 100 mm/s always generates more nucleation sites and therefore more but smaller cells are created. The average porosity is 65.8 % and the porosity gradient is reduced.

When directly comparing the results obtained at the two extrusion temperatures, guidelines to tailor on line the morphology of a filament can be proposed. The average pore size was reduced by increasing the deposition speed, because of the induced higher depressurization rate that promotes more cell nucleation and reduces the time window for cell growth. Same consideration applies for the temperature, which increase correlates negatively with the average pore size.

The heat transfers from the heating block through the nozzle and the material influence as well the pore size distribution and pore density. Temperature gradients in the polymer induce viscosity gradients, which are tuned also by changing the deposition speed. By this, core-skin filaments or hollow filaments could be created and deposited simultaneously, inducing a slow depressurization and cooling in the first case and a fast cooling at high depressurization in the latter. How the extreme processing conditions influence the internal microstructure of the porous strands can be interpreted to guide to the creation of custom morphologies. Depositing different layers one on top of another by 3D printing layer-by-layer process enables to tune cellular structures to a precise hierarchy of micro and macro pores, as shown in Figure 6.4.

These foam morphologies were obtained under free foaming conditions (discussed in Chapter 4). The absence of a restraining mold allows the strands to foam homothetically, promoting pore growth instead of nucleation. When depositing these strands in a layer-by-layer fashion, the interface between two micro-porous strands is expected to follow a more confined behaviour (e.g. promoting nucleation and thus the creation of smaller pores), therefore creating an intrinsic gradient porosity from the core of the beam to the surface.

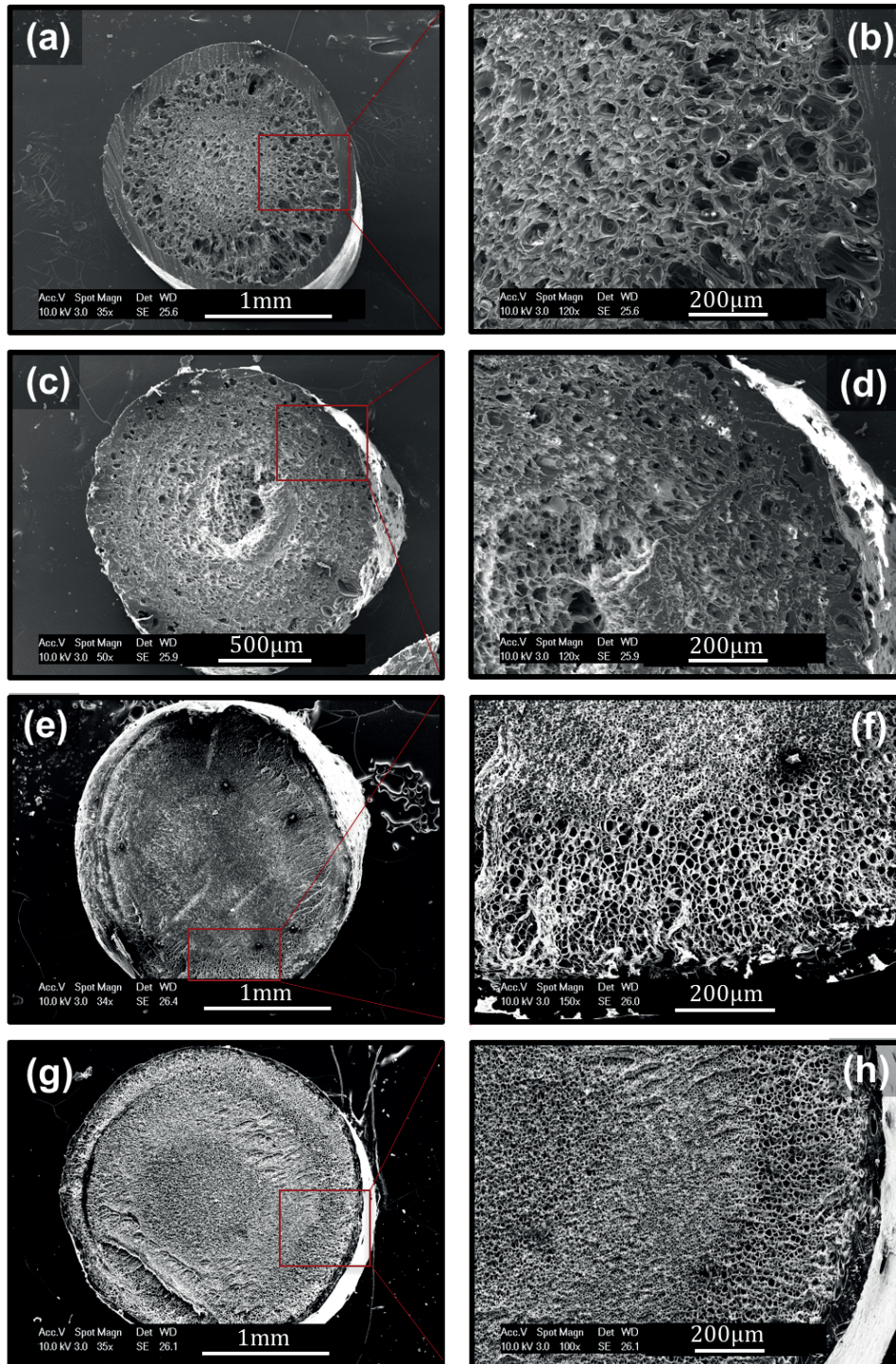


Figure 6.4 SEM images of strands morphology at extreme extrusion temperature (180 °C to 250 °C) and speed (10mm/s to 100 mm/s) at 14 wt%CO₂. At 180 °C the heat transfer through the material is non homogeneous (PLA T_m = 160 °C), afflicting pores growth. (a, b) As a result of the low printing speed (10 mm/s), a thick skin is formed on strands surface. Pore size increases homogeneously from the centre of the strand to the skin as a result of the low cooling rate and low depressurization. (c, d) At high printing speed (100 mm/s), the rapid depressurization induces pores collapsing at the strand core. A hollow-like structure with a continuous channel of an average diameter of 300 µm is formed. At 250 °C

the printing temperature is sufficient to assure to melt homogeneously the material in the nozzle. (e, f) At low printing speed (10 mm/s) pores growth is reduced, producing smaller pores compared to low temperature. A well-defined porosity gradient from centre to surface is shown, with lower skin formation. (g, h) Increase the printing speed to 100 mm/s increases as well the depressurization rate. Nucleation sites increase as a result, producing a higher number of pores compared to a lower depressurization rate.

6.3.4 Strand-to-strand interface

A multifilament structure obtained with deposition parameters of 220 °C and 25 mm/s, of polymer with 14 %w CO₂ content was then sliced and analysed at SEM with the methodology previously described. In Figure 6.5 it is possible to observe how the filaments foamed during deposition and bond together with a thick interface of about 150 µm. Intimate contact and interdiffusion¹⁸⁹ are obtained locally between two filaments during the fusion bonding. The pressure drives the first bonding phenomenon. Here the expansion of the filament during deposition certainly brings additional pressure for reaching intimate contact. The interfacial structure goes gradually from cellular intra filament structure to bulk interface and then again to cellular porous structure. As previously discussed, the deposition of porous strands in a layer-by-layer fashion promotes nucleation (confined foaming) instead of pore growth (free foaming). At the interface between the strands a smaller porosity is thus formed, thus creating intrinsically a porosity gradient.

The possibility to layer different filaments to create complex 3D shapes of foamed materials is demonstrated and expands the versatility of the classical FDM. Core-shell porous structure is a well-known morphology in nature, being in compliant vegetables structures or in stiff bone¹⁹⁶. Furthermore, structures combining oriented filaments each having different properties and functions is of main interest in the new generation of functional composites for engineering applications. Implants where vascularization or drug delivery can benefit from anisotropic porosities therefore with various diffusion paths and flow kinetics will certainly be part of the coming generation of body regeneration and repair solutions.

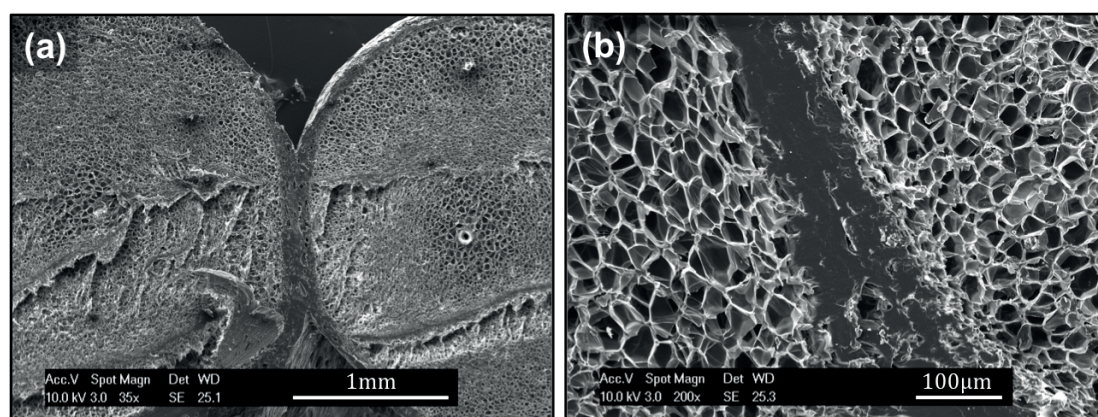


Figure 6.5 Scanning Electron Microscopy of layer-by-layer deposition of foamed strands. (a) Interface bonds between two core-shell strands. CO₂ escapes from the material during the extrusion melting phase, producing a pressure at the edge of the nozzle and allowing a good bonding between the deposited layers. As results, a thick solid interface from the shell fusion is created, showing a gradual passage from porous to bulk and porous again (b).

6.3.5 Pores density evolutions

Strand density was measured by precision scale after being printed. Two saturation conditions (7 wt%CO₂, 20 wt%CO₂) printed at three different temperatures (180, 215, 250 °C) and speeds (10, 25, 50 RPM) were considered.

At high wt%CO₂ at 215 and 250 °C, a negative correlation between printing speed and density is observed. While increasing the printing speed, the depressurization is expected to increase, producing a higher filament expansion and therefore reducing the density by increasing the strand porosity. At 180 °C, it is impossible to observe an explicit trend. These results well suit the experiments of strand expansion during printing shown in Figure 6.6, which discussion on heat exchange at the nozzle also explains the trends.

At 7% wtCO₂ strands density follows an unpredictable trend: at 250 °C density is positively correlated with printing speed, while reducing the temperature the correlation disappeared (at 215 °C) and became negatively correlated.

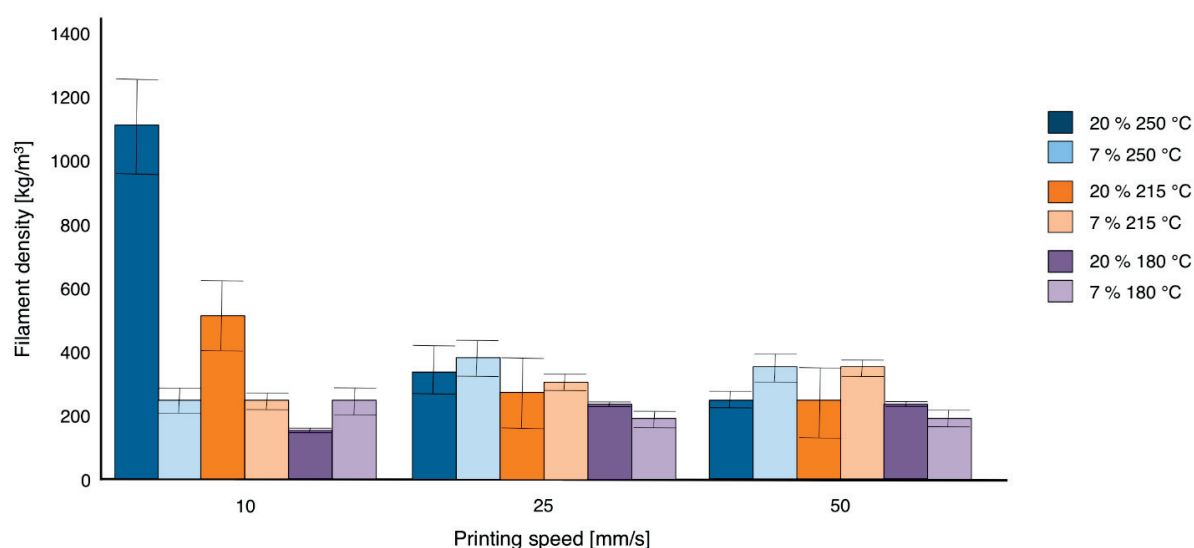


Figure 6.6 Free-flow strand density obtained at different printing speed at two set points of nozzle temperature (low 180 °C, high 250 °C) and two values of CO₂ %wt (7 %wt and 20 %wt). At 7 %wt, at 180 °C an increase in density is observed increasing the printing speed from a 10 mm/s to a 25 mm/s. No influence is shown at 50 mm/s. At 250 °C, the peak of density is at 25 mm/s, while there is no statistical difference extruding at 10 or 50 mm/s. At 20 %wt, at 180 °C there is no statistical difference among all the processing condition. However, at 250 °C, the strands density sharply falls from a 10 mm/s to 25 mm/s and finally to 50 mm/s.

6.3.6 Strand mechanical properties

Gibson-Ashby model was applied to indirectly estimate the open/closed porosity from a set of filaments at 250 °C from density measurements (Figure 6.7). Empirical data of the local filament Young's modulus were collected from instrumental nanoindentation on a set of $n = 5$ measurements of 3 samples. In Figure 6.7 it is possible to appreciate how the experimental values from nanoindentation fits in the region delimited by the two models, estimated at 100 % closed porosity ($n = 1$, top orange line) and 100 % open porosity ($n = 2$, bottom grey line). Even if the average values well fits the experiments, it is difficult to give conclusions about the mechanical properties of the single porous strand by using nanoindentation. The low reproducibility, due to the indentation of porous structures, and the curved surface of the porous filaments do not allow repeating with confidence the experiments. Triple point bending has been investigated as putative method to collect information about the Young's modulus of the porous filaments, giving promising preliminary results.

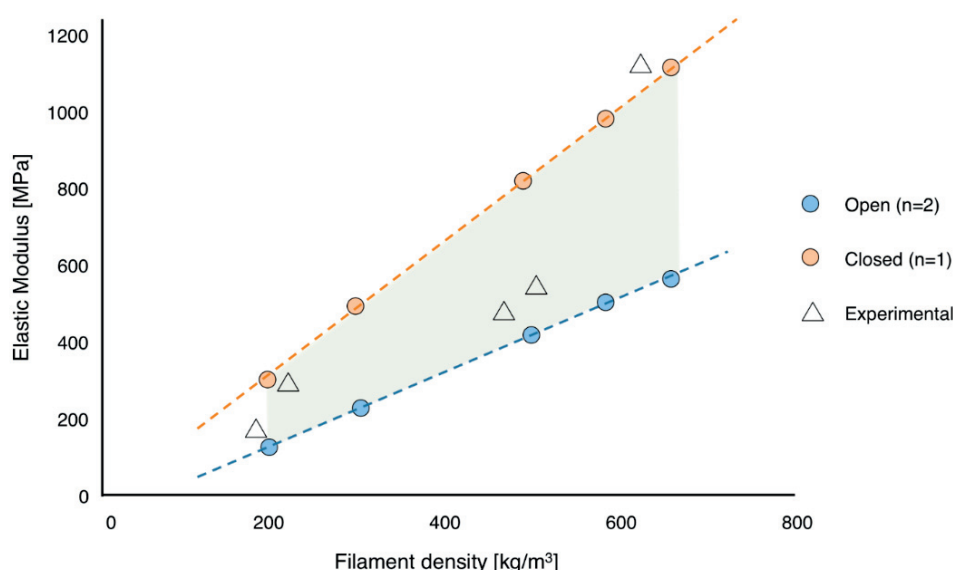


Figure 6.7 Young's modulus measured by instrumental nanoindentation ($n=3$ samples, $n=5$ measurements) and compared with Gibson-Ashby model with closed ($n=1$) and open ($n=2$) porosity. Experimental values fits in the modelling region delimited between fully open (low end) and fully closed (high end) porosity, showing a potentially good inter-connectivity of the pores.

6.3.7 3D printing of medical foams

As demonstrated with PLAm1, strands diameter (e.g. pore size and porosity) can be adjusted varying the processing parameters (printing speed and temperature). In particular, the strands expansion is observed to be maximum at 250 °C, limit temperature before to induce polymer degradation. For some applications stiff composite filaments or deformable porous filaments might be required for the overall 3D structure or for some local or directional elements only. In the next section, the two material selected for osteochondral repair from the results in Chapter 5 were selected to be processed by 3D foam printing. Printing speed was set to 50 mm/s, as soft materials (e.g. PLAPCL) are difficult to be printed at higher speeds due to jamming in the feeding system. Saturation cycles were chosen to: i) maximize the CO₂ content, ii) obtain a similar w%CO₂ content in each material and iii) keep saturation time as short as possible. 10 w%CO₂ was reached for both the materials prior to printing.

Following the same protocol of saturation and printing described in Chapter 3, a composite filament of PLAB-TCP with 77.63% open porosity was obtained (Figure 6.8), which could be used to directly 3D print bone scaffolds, guiding bone growth by controlling the 3D deposition of osteoconductive and stiff porous strands as previously demonstrated^{34,197}. In the latter case, PLAPCL strands showed a closed porosity (average 80.26%) and limited strand expansion, (average diameter: 1.42 mm). The already low stiffness of PLAPCL structures could be therefore further reduced to produce anisotropic soft foams, thanks to the low strand expansion during the printing. An example of 3D printed scaffold is given in Figure 6.9.

The difference in porosity between PLABTCP and PLAPCL can also be explained by the foaming phenomena associated with the properties of the two materials. PLABTCP is a composite material, presenting small ceramic particles embedded into a Poly(lactide) matrix. The presence of such particles promotes an increasing of material viscosity and crystallinity. Both these material features have a negative correlation with pore growth, reducing the average pore size. At higher viscosity, the pressure required to expand a single

pore is higher, producing therefore smaller pores compare with the same material at lower viscosity under the same foaming conditions. Higher crystallinity prevents CO₂ diffusion, reducing both the gas concentration in the material and thus the driving force to expand the pores. PLABTCP is therefore expected to show smaller pores, as confirmed by Figure 6.8.

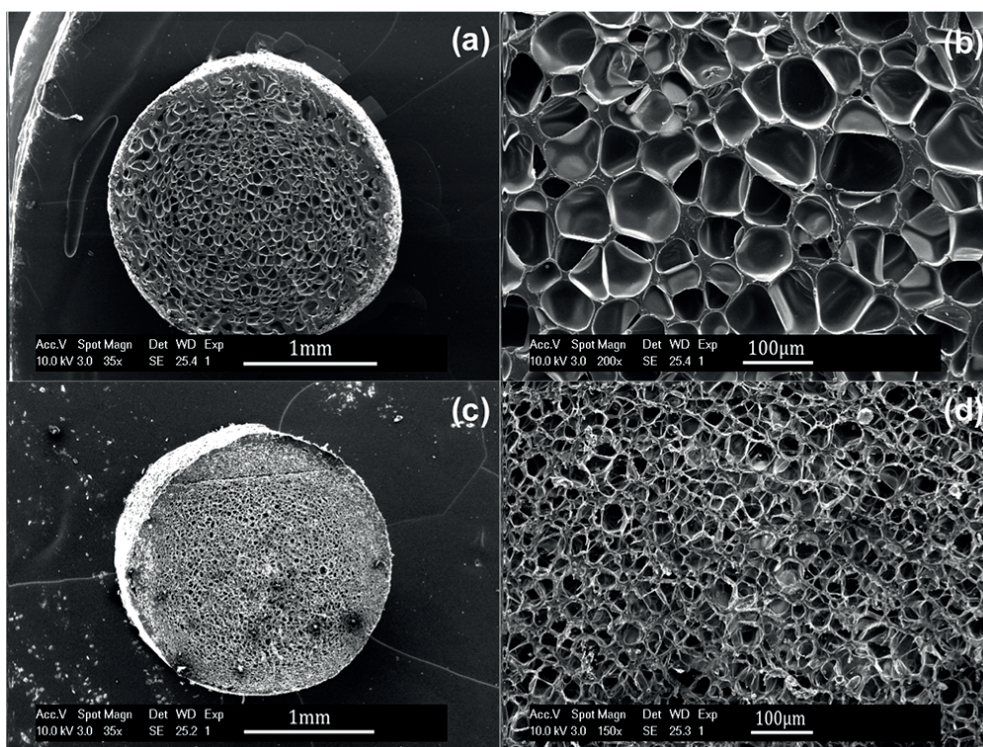


Figure 6.8 (a) SEM cross-section of a PLAPCL foamed strand, showing a close porosity (b) homogeneously distributed (average porosity: 80.26 %). (c) A PLAPCL strand showing a homogeneous open cells porosity (average porosity: 77.63 %), (d) increasing from the edge to the centre.

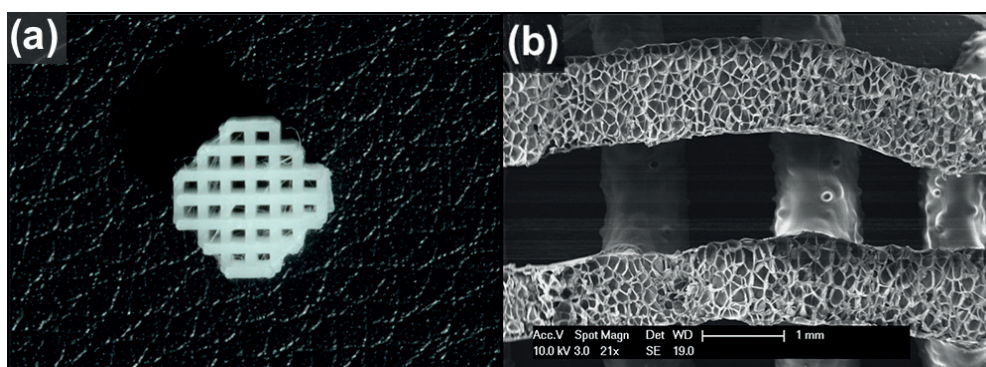


Figure 6.9 Exemplification of a hierarchical structure obtained by 3D foam printing. a) A custom geometry is created depositing porous strands, giving the overall 3D shape by layer-by-layer deposition, while b) the micro-porosity within the strands is tuned by controlling the CO₂ desaturation from the filament during the deposition.

6.4 Conclusions

In this work we introduced a new additive process, called 3D Foam Printing (3DFP), to create complex 3D hierarchical porous geometries. Physical CO₂ foaming can now be miniaturized into a FFF/FDM 3D printer, introducing for the first time the possibility to deposit porous strands into a macro-porous structure in a controlled process.

The process was first validated with PLAm1 1.75 mm filament and developed by mean of a Makerbot Replicator 2 3D printer. In particular, two processing windows have been established, describing: (i) which saturation condition shall be adopted to meet the desired CO₂ concentration in the desired filament and (ii) which printing conditions (e.g. nozzle temperature and extrusion speed) shall be used to produce the desired strand morphology (e.g. hollow, radial porosity gradient, homogeneous porosity). For the latter point, Simplify 3D, a slicing software, has been adopted to precisely monitor all the 3D printing parameters.

A link between fundamental foaming steps (e.g. nucleation, cell growth and stabilization) and printing parameter (e.g. temperature, speed and nozzle size) was established to control the micro porosity within the extruded strands. The *in situ* foamed strands can be layered to create a 3D structure with a solid interface between two porosity gradients, controlling the microstructure at each layer by varying online printing speed and temperature. This design freedom is one of the main advantage of this new technology compared to e.g. solvent casting/particulate leaching, in which the materials needs to be modified to include a porogen (e.g. salts, sugar, glycerol).

The nozzle size has a notable influence over strand desaturation and therefore over foam expansion and morphology. At small nozzle size (e.g. below 1 mm), strands porosity was negligible, non-uniform or not controllable. At larger nozzle size (e.g. 1 mm) printing parameters can be tuned to influence the porous strands during free extrusion (e.g. without depositing the strands or layering them). In particular, strand expansion at the nozzle end and micro-cellular morphology are controllable by increasing or decreasing printing temperature and speed.

Scanning Electron Microscopy investigation of multi-layered porous strands shows a thick non-porous interface between consecutive porous cores. The fusion bonding of these foams skin ensured the integrity of the final cellular structure. Mechanical properties have been assessed by instrumental nano indentation and then correlated with Gibson-Ashby models of open/closed cellular structures. The cellular filaments have modulus closed to the one of the open cell model, indicating the presence of interconnectivity.

3DFP has been here extensively characterized for an extrusion grade Poly(lactide), but also applied to different biomaterials. PLAPCL and PLABTCP composite filaments were used to successfully obtain cellular leading to the creation of sample specimens.

By being able to control pore size, distribution and morphology online while printing, this technology would allow the manufacturing of complex 3D gradient geometries with dual-porous hierarchical architectures. The combination of oriented strands each having different properties and functions is of main interest in the new generation of functional composites for engineering applications. Implants where vascularization or drug delivery can benefit from anisotropic porosities therefore with various diffusion paths and flow kinetics will certainly be part of the coming generation of body regeneration and repair solutions. The unmatched design

freedom of free form 3D hierarchical porous structures could be applied not only for tissue engineering applications, but also to positively influence fields as energy storage and microfluidics, where a tuneable multi-scale porosity is highly demanded.

Chapter 7 Conclusions and Perspectives

7.1 Conclusions

The main objective of this study was to develop novel manufacturing methods to produce hierarchical cellular structures and apply them to the creation of scaffolds for osteochondral repair. It was achieved by integrating Additive Manufacturing of polymer materials using Fused Deposition Modelling / Fused Filament Fabrication (FDM/FFF) and Supercritical carbon dioxide Foaming (ScCO_2) to produce cellular structures with tuneable micro and macro porosities. The versatility of the process allows to envisage other applications.

A process called 3D homothetic foaming was characterized for the first time. It allows foaming a 3D printed macro porous structure into a dual porosity macro and micro cellular structure. This process was exploited to create hierarchical scaffolds from a model thermoplastic material, a food grade Poly (lactide acid). All the processing steps were considered from the melting and extrusion of polymer filaments, to their deposition under different conditions, and their successive placement in 3D structures that were then foamed. For example, an initial 3D printed structure with a strength of 30 MPa at 15 % deformation could be tailored by foaming to have strengths ranging from 10 MPa to few kPa.

Filaments for 3D printing of six different biomaterials, including copolymers and composites were extruded and characterized. In particular, the effect of extrusion parameters on crystallinity and polymer degradation were investigated, showing how to process medical materials from raw powder into a well-shaped 3D structure. Homothetic foaming was applied to the 3D printed templates of the previously characterized medical materials. The processing windows were determined to control the foaming and how to tune the mechanical properties of the final micro/macro porous structure. Moreover, it was demonstrated that homothetic foaming is a selective process that could be used to foam only a single material of a multi material structure. In particular, a multi material scaffold of PLAPCL and PLABTCP was selectively foamed to mimic the osteochondral hierarchical microstructure and mechanical properties.

A second novel process to produce hierarchical micro/macro porous structures by 3D printing was described for the first time under the name of 3D Foam Printing. It was studied how to saturate a thermoplastic filament and place 3D porous strands in a layer-by-layer fashion to additively create complex cellular structures. The influence of the processing parameters on strands porosity and strands expansion was clearly described, showing how to live tune the pores morphology during the deposition. For example, hollow strands or having a radial porosity gradient were obtained. Different materials were investigated, from a food grade Poly (lactide acid) to different medical filaments.

Furthermore, local mechanical properties of human articular cartilage were established by instrumental nanoindentation. It was demonstrated that articular cartilage increases in stiffness from the superficial layer expose to cartilage-to-cartilage contact to the subchondral bone. A first step towards the mimicking of the local stiffness value observed has been obtained reproducing the average stiffness measured in human cartilage, which average value is equal to 2.5 MPa. This result was obtained by mean of a multi material structure, composed by a 3D printed composite PLA based material (PLABTCP) and a soft foamed copolymer of PLA and PCL (PLAPCL). Figure 7.1 illustrates the main obtained results, showing how the studied process and materials cover the performance area between bone and cartilage. The purple area shows the Young's modulus / density values obtainable by 3D printing of PLABTCP and PLAPCL, while the blue area the range of properties obtained after applying homothetic foaming to the original 3D structure. Finally, the green area

shows the target Young's modulus value to match the human articular cartilage properties. PLAPCL scaffolds well met the desired range of Young's modulus, but are almost two order of magnitude away in density from what observed in articular cartilage. A way to reach the desired density with the proposed PLAPCL scaffold would be to fill the macroporosity with an hydrogel. An hybrid multi-material structure would be then created, offering the density of a liquid (hydrogel density is equivalent to water density, which constitutes 70 % of the cartilage) with the mechanical properties of the PLAPCL scaffold.

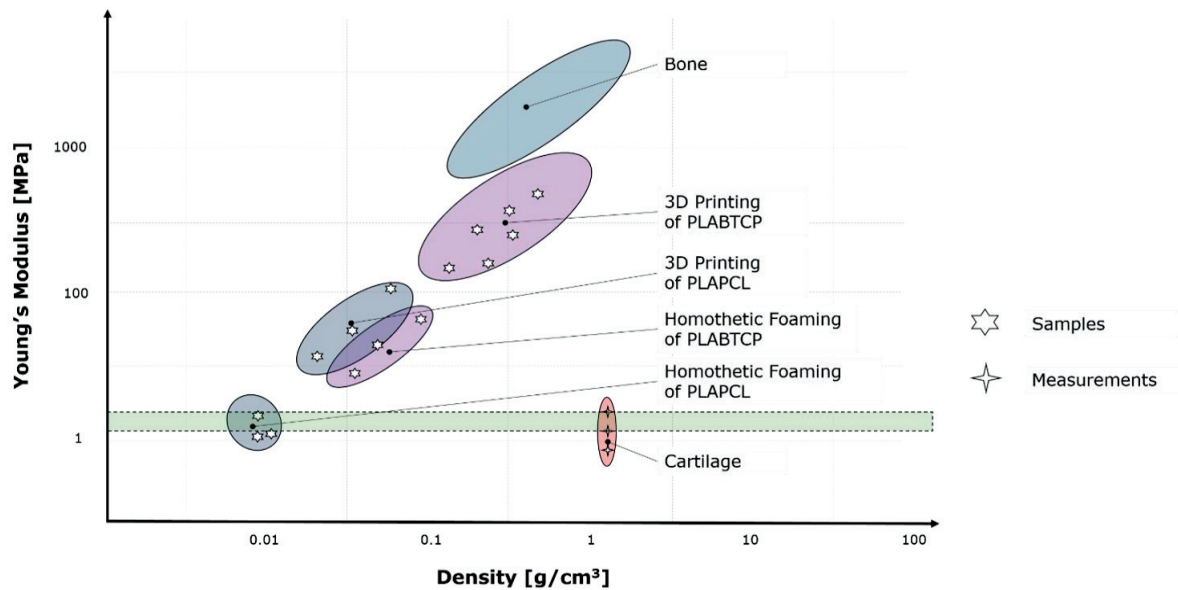
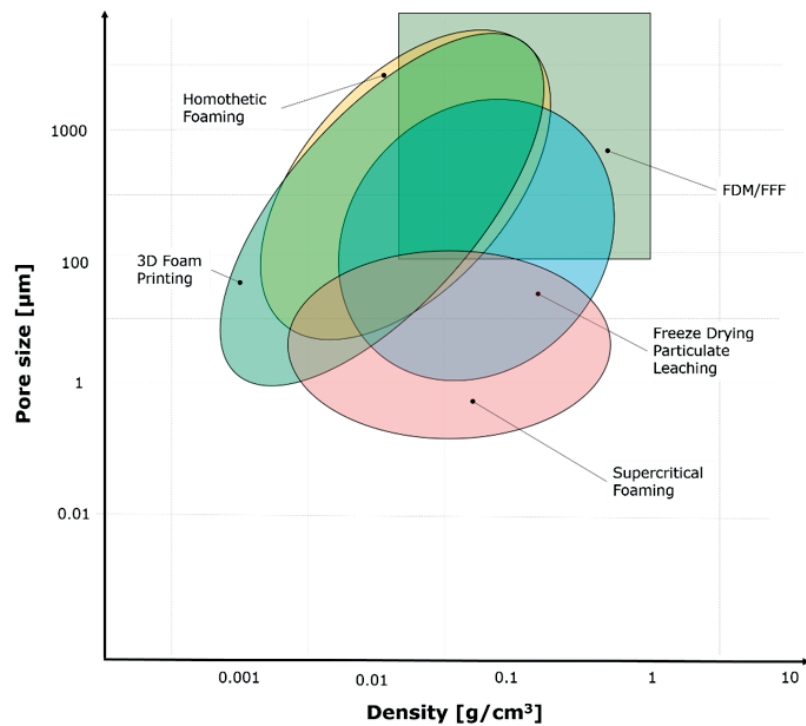


Figure 7.1 Ashby diagram comparing the structures developed by homothetic foaming and 3D foam printing with the target application of osteochondral repair. The blue area represents the range of Young's modulus / density achievable by homothetic foaming, while the purple area the one achievable by 3D printing. The green area represents the target Young's modulus value to mimic cartilage measured properties.

A comparison of homothetic foaming and 3D foam printing in comparison with other manufacturing methods to process cellular structures is made in Figure 7.2. Average pore size and structure density of different manufacturing methods were compared. While offering a greater freedom to process complex 3D geometries when compared to other methods, FDM/FFF suffers a limitation in the maximum achievable porosity. Homothetic foaming, described in Chapter 4 and 5, clearly opens the possibility to manufacture novel hierarchical cellular structures, reducing structure density and therefore the average structure stiffness. 3D foam printing, described in Chapter 6, comes as an update of the homothetic foaming, offering for the first time the possibility to live tune pore morphology and porosity gradient during the process. This was possible by demonstrating the influence of the 3D printing parameters on the micro-porosity (Chapter 6, paragraph 6.3.3).



	Supercritical Foaming	Freeze Drying Particulate Leaching	FDM/FFF	Homothetic Foaming	3D Foam Printing
Complex 3D geometry	✗	✗	✓	✓	✓
Gradient porosity	✓	✓	✓	✓	✓
Open cell porosity	✗	✓	✓	✓	✓
Solvent free	✓	✗	✓	✓	✓
Precisely tune pore size	✗	✗	✓	✓	✓
Possibility to obtain online porosity control	✗	✗	✗	✗	✓

Figure 7.2 Comparison of the state of the art manufacturing methods to produce cellular structures with the new methods described in this work, homothetic foaming and 3D foam printing.

7.2 Perspectives

7.2.1 Increase open porosity

Homothetic foaming, the process born from the combination between the high precision and reproducible technique of Fused Deposition Modelling 3D Printing and the solvent free technology of Supercritical CO_2 foaming, has been proved to work for poly(lactide) based materials.

For certain materials and foaming conditions a principal limitation of the homothetic foaming is the formation of a hard and impermeable skin of non-porous material at the surface of the structure. This phenomenon, well-known in batch foaming, could be a limitation to obtain an open porous structure and precludes the access to the micro-porosity. Given the physics of the phenomena, an approach to limit the skin formation could be the co-foaming of the 3D printed structure in a soluble polymer with viscosity close to the PLLA at the processing temperature. PEG 8M could be a good candidate to this concept, given its high MW (8,000,000u) and solubility in water. The protocol would then include a step of dipping of the PLLA scaffold in PEG, creating a protecting coating to increase the resistance to CO₂ escape from the surface of the scaffold and thus improving gas nucleation on the edges.

7.2.2 Interface quality of a 3D Printed structure

Regeneration of the osteochondral tissue suggests the application of a material able to replicate cartilage and bone mechanical properties. Co-foaming of different materials has been assessed to be limited³⁹, mainly due to the difficulty to properly control the interface between the foamed structures and thus define a tide-mark between cartilage and bone scaffold. Additive Manufacturing represents a good alternative to produce a reliable multi material structure, but the fusion bonding at the interface between two different materials is still not fully understood for the considered processes. Results showed how Compact Tension Specimen (CT) represents an interesting way to access the fracture propagation toughness at the interfaces between 3D printed layers. Another test applicable to confirm CT test results is the Double Cantilever Beam (DCB). CT and DCB tests on 3D printed multi-material structures could address the printing quality of such materials, investigating the best processing parameters to create a multi-material structures with cohesive failure.

7.2.3 Optimization of 3D Foam Printing

A new additive manufacturing method to layer porous micro cellular strands into a 3D hierarchical structure was presented in Chapter 7. The unmatched possibility to create custom-made 3D structure with designed macro and micro porosity opens interesting possibility in many different fields, in function of the applied material. In biomedical applications, a machine able to produce 3D cellular structure mimicking tissue local stiffness using biopolymers could be applied to produce patient specific scaffolds. Compared to standard machining, additive manufacturing allows saving up to 79 % of the materials. While presented here to process hierarchical structure for tissue engineering applications, this method could easily be adopted by other fields requiring complex porous 3D polymeric structures. As example, 3D foam printing of techno-polymers could be beneficial for applications in the automotive and aerospace industries, where lightweight foams with excellent mechanical properties are essential for planes and satellites. Also, complex microfluidics devices could be produced in a one-step process, playing with the variety of porous geometry that the process allows to layer down into a 3D structure.

7.3 Towards applications

This work introduces for the first time new manufacturing methods to produce 3D hierarchical structures, namely homothetic foaming and 3D Foam Printing. It was established how these methods could be applied to create a multi-material scaffold with average stiffness close to the one observed in the articular cartilage, which today represents one of the most challenging tissue to repair in the musculo-skeletal field. Poly(lactide-co-caprolactone) and Poly(lactide / β TCP) were selected to reproduce respectively cartilage and bone in osteochondral applications.

A wider analysis on the biocompatibility of such structures should be proposed as a natural continuation of this work. While preliminary results showed a poor cell affinity for this scaffold, it is known in literature that surface modification could greatly improve this critical point. Moreover, sterilization of such a structure is a key point in term of go to market strategies for the potential commercialization of such an application. Sterilization by mean of supercritical CO₂ during the homothetic foaming should be further investigated, as if proven to work it would represent a great advantage for cost reduction and material preservation.

Osteochondral grafts were proven to fail in the short-medium term, due to low mechanical stability, poor integration or cell re-differentiation into fibroblasts. A way to overcome such issues is to introduce a step priori implantation with a bioreactor with the induction of cyclic loading on the scaffold. Two different chambers would be required to differently stimulate the bone and cartilage layers. Moreover, fatigue test would be required to determine the life cycle of the proposed scaffold.

Homothetic foaming and 3D Foam Printing were here proposed to produce hierarchical structures of medical materials. In the future, these processes could be applied to different materials, opening new possibility in fields that require custom shape cellular materials with lightweight properties (e.g. Aerospace and Defence, Automotive, Packaging, etc.) (Figure 7.3).

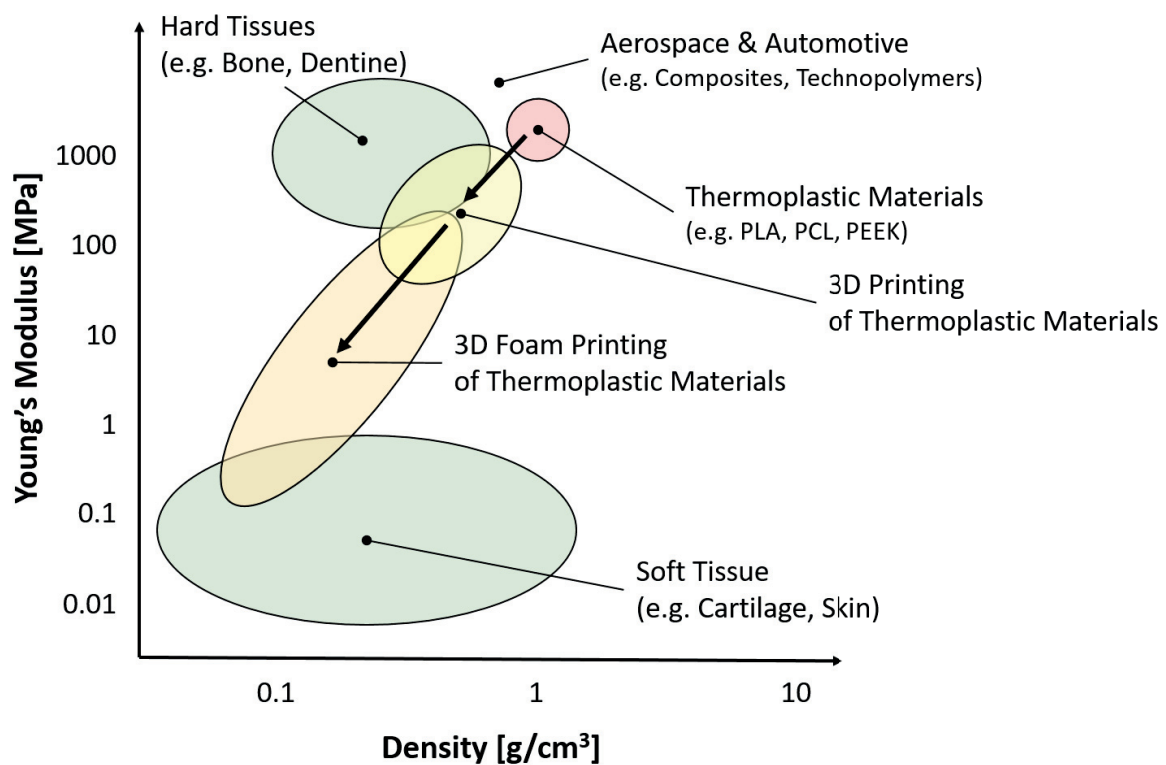


Figure 7.3 Ashby diagram showing the range of structures potentially achievable by homothetic foaming and 3D foam printing in comparison with target polymer applications, as Aerospace and Automotive¹⁹⁸.

ANNEX I Cells Response to Biomaterial

The aim of this chapter is to discuss the biocompatibility and cells response of the different scaffolds processed in Chapter 5 and Chapter 6. Preliminary in-vitro tests were conducted at first on simple 3D printed medical materials and therefore applied to foamed multi material scaffolds of PLAPCL/PLLABTCP, as pure thermoplastic structure or impregnated with an Alginate hydrogel loaded with encapsulated cells. A comparison among the different scaffold was drawn over after Presto Blue assay, comparing cells viability over a period of 3 weeks. Finally, conclusion and future perspectives on how to improve the material for the next round of in-vitro test are discussed.

AI.1 Materials and methods

AI.1.1 3D Printing

All the scaffolds were printed with a Markerbot Replicator 2, equipped with a 0.3mm nozzle size. PLAm1 was printed at 210 °C, 50 mm/s and layer heights of 0.1 mm. PLAPCL was printed at 190 °C, 40 mm/s and layer heights of 0.1 mm. Multi material PLAPCL/PLLABTCP and PLAPCL/PLA were printed under the same conditions as the mono-material structures, but stopping the printing at 50% to allow changing the input filament.

AI.1.2 Homothetic foaming

The PLAPCL/PLABTCP were foamed as explained in Chapter 5 using the best condition to maximize material density reduction (135 °C, 180 bar, 5 minutes, 60 bar/s). All the scaffolds, but the ones impregnated with Alginate were sterilized for 5 minutes at 120 °C by a steam autoclave.

AI.2 Results

AI.2.1 Cells viability on 3D printed scaffolds

In this section the biocompatibility of different 3D printed scaffolds with bovine chondrocyte after 3 weeks is discussed.

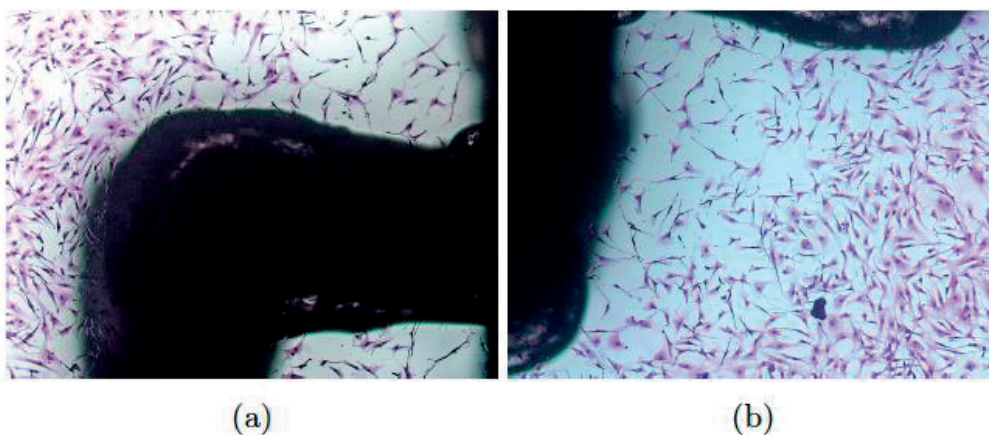


Figure AI.1 Biocompatibility test with bovine chondrocytes on a PLAm1 scaffold.

The model PLAm1 has been used to produce different 3D scaffold for the first tests. This Poly(lactide) grade is classified as a food grade (e.g. ideal for packaging application) and does not qualify as a medical material. Poly(lactide) and thermoplastics in general are well known to possess hydrophobic surfaces, e.g. reducing cells-surface interactions. In Figure AI.1 it is possible to observe how cells prefer to colonize the Petri dish around the material, creating an inhibition area surrounding the scaffold.

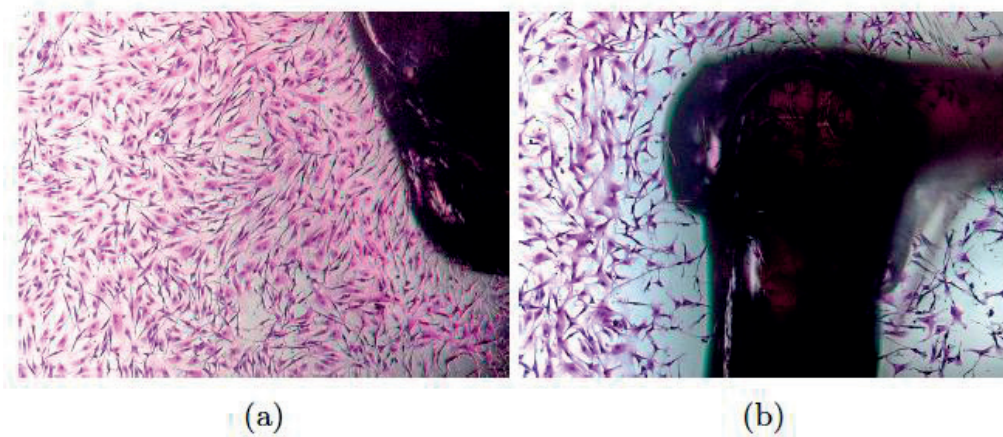


Figure AI.2 Biocompatibility test with bovine chondrocytes on PLAPCL.

The second material tested was a medical grade copolymer Poly(lactide-co-caprolactone), the PLAPCL. Medical has been reported in literature to express a hydrophobic surface, requiring therefore surface modifications treatments, as by plasma grafting of RGD peptides or by sol-gel with titanium oxide^{199,200}. Higher cells affinity was shown compared to PLAm1, as shown in Figure AI.3a. However, some regions showed a zone of inhibition as found for the food grade PLA, as observable in Figure AI.3b. This is probably due to particle release in the medium, inducing cells apoptosis, as observable in Figure AI.1b and Figure AI.3b, where the two materials were printed in a multi material structure.

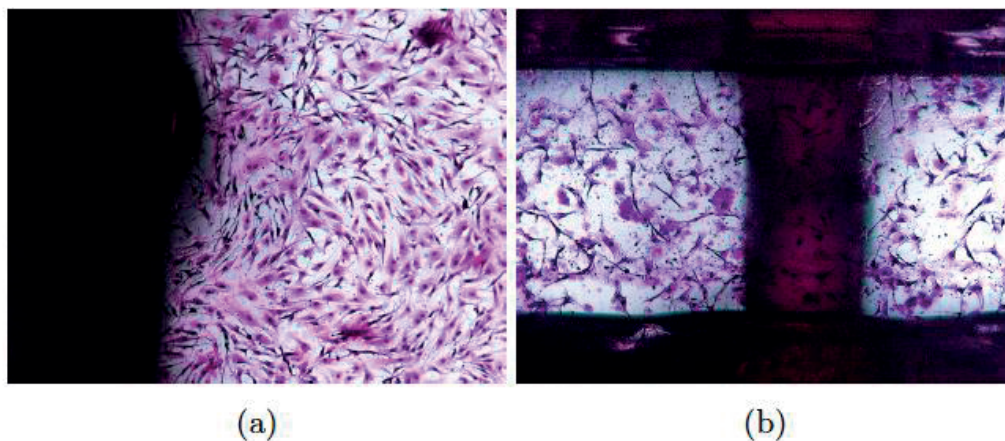


Figure AI.3 Biocompatibility test with bovine chondrocytes on a multi material scaffold PLAm1 – PLAPCL L703s.

Finally, a multi material scaffold of PLAPCL and PLABTCP was investigated by the same protocol, Figure AI.4. Two different behaviours were observed at the surface of the scaffold and in the inner porosity. While the surface of the scaffold showed a good cells attachment and viability, as could be seen in Figure AI.4a and AI.4b, within the inner porosity cells find difficult to differentiate and therefore they are incurring to apoptosis. Less particle release is observed after 3 weeks compared to PLAm1 and multi material PLAm1/PLAPCL, probably due to the longer degradation rate of PLABTCP compared to PLAm1.

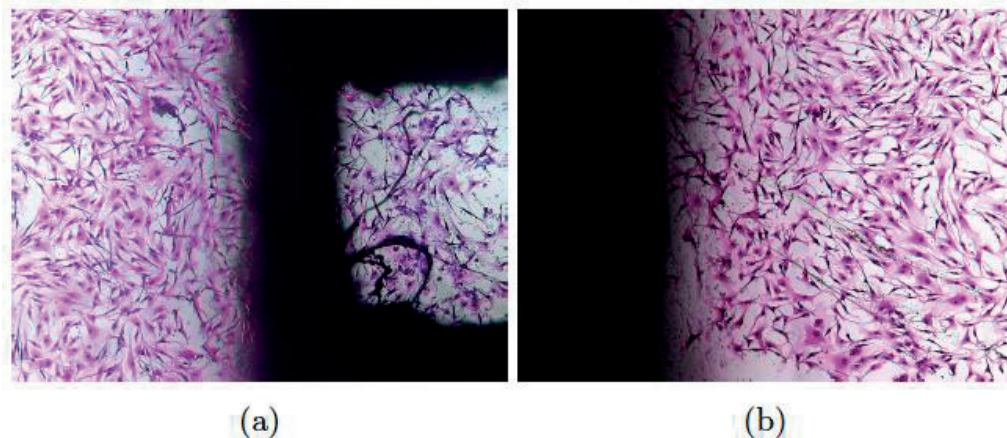


Figure AI.4 Biocompatibility test with bovine chondrocytes on multi material scaffolds of PLAPCL and PLABTCP.

AI.2.2 Cells viability in 3D printed, foamed and impregnated scaffolds

To confirm the goodness of a multi material PLAPCL/PLABTCP scaffold as osteochondral tissue replacements, further tests were conducted on week-by-week analysis of mesenchymal stem cells on such multi material scaffolds in three different conditions: before foaming (only 3D printed structure), after foaming and after foaming impregnated with an alginate hydrogel.

A Presto Blue assay was applied to a set of different scaffolds and compared with a background fluorescence of an empty control (no scaffold, no cells). Eight samples of 3D printed multi material scaffold were monitored up to 6 weeks, after which all the scaffolds experienced a severe degree of degradation. It was observed a constant increase of cells viability from week 1 to week 4, kept as average at a steady state during week 5. After week 6, delamination of the scaffold beams and fragmentation at the interface between the two materials were observed, leading to a substantial drop of MSCs viability, as showed in Figure AI.5. As known from literature, 3D printed scaffolds of Poly(lactide) and poly-caprolactone based structures has a longer degradation time than the 5 weeks we observed during the experiment^{52,201}. We postulate that for 3D printed structures, the sterilization method applied by high temperature autoclave is sufficient to trigger polymer degradation and weaken the fusion bonding at the interfaces between the deposited strands and the two materials.

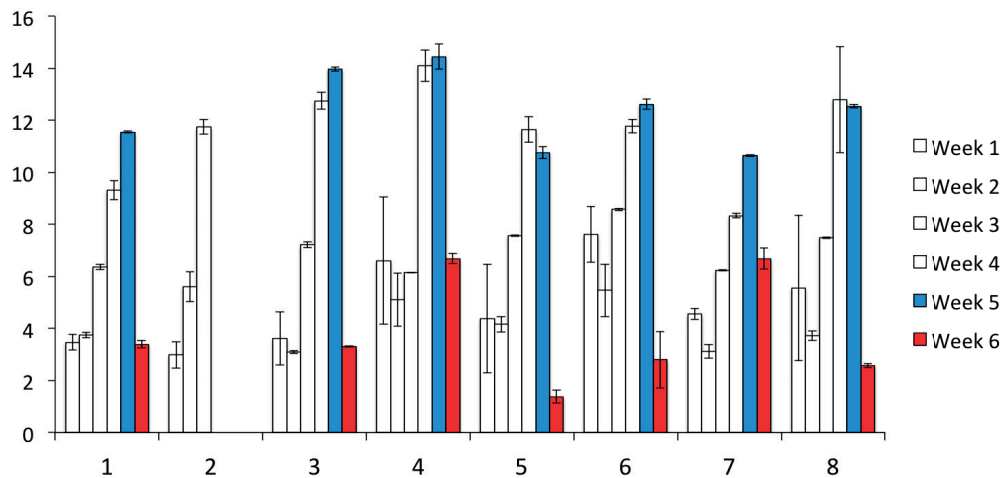


Figure AI.5 Presto Blue assay of mesenchymal stem cells viability on 3D Printed PLAPCL/PLABTCP scaffolds after 6 weeks. Cells viability increases from week 1 to week 4 and keep a constant value until week 5. At week 6 the scaffold started degrading, inducing a drop of cells fluorescence.

A second parallel test was conducted on PLAPCL/PLABTCP scaffolds after being foamed, as described in Chapter 6, for a time scale of 4 weeks. Similarly to the 3DP structures, we observed an increase in cells viability from week 1 to week 3 for three over seven samples. The remaining four scaffolds showed an early delamination after being sterilized by high temperature autoclave, which lead to scaffold fragmentation by week 4. Cells viability in these samples is steady or decreasing, showing the difficulty of MSCs to find a surface to proliferate, encountering therefore early apoptosis (Figure AI.6).

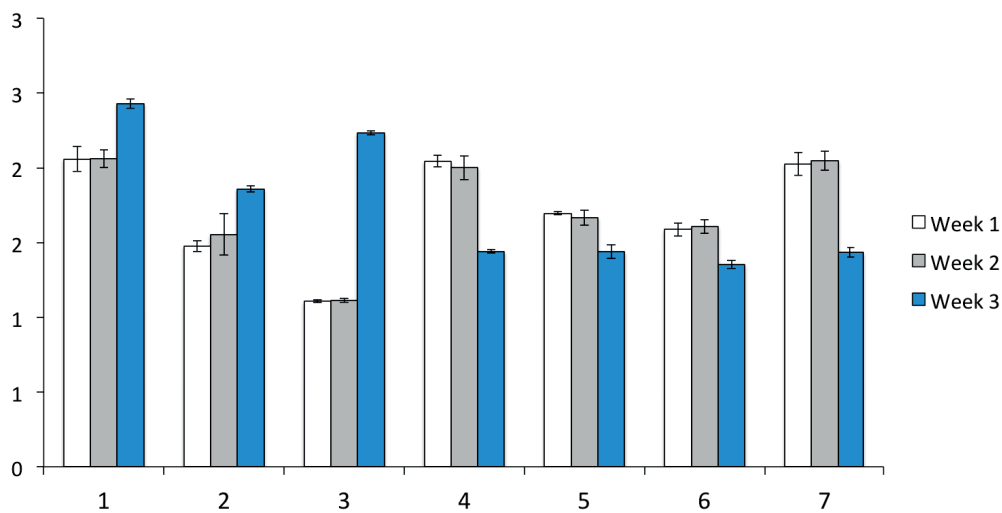


Figure AI.6 Presto Blue assay of mesenchymal stem cells viability on 3D Printed and foamed PLAPCL/PLABTCP scaffolds after 3 weeks. Cells viability increases from week 1 to week 3 in samples 1 to 3, which did not express any degradation during the observations. Viability in sample 4 to 7 was constant during week 1 and 2, while start decreasing from week 3, originated from a scaffold delamination at the interface between the two materials. This degradation was induced by the sterilization process, lead at 120 °C in autoclave, which deteriorated the scaffold mechanical properties.

In the last set of measurements, eleven PLAPCL-PLABTCP foamed scaffold were impregnated with Alginate and encapsulated MSCs for a total of 5 weeks (Figure AI.7). No pre-sterilization was necessary after the foaming, as the samples were store into a sterile 48 well plate during the manipulation under hood. During all the observation time, a steady increase of cells viability was observed, sign of healthy proliferation of the cell population within the hydrogel. The observation of cells proliferation in specific areas, as the interfaced between the hydrogel and the thermoplastics or the interfaced between the two materials was impossible due to the important thickness of the sample (about 5mm) and the low transparency of the Alginate hydrogel. At week 5 a mismanipulation led to an aspiration of the cells content in the surnatant, preventing the experiment to be continued. No evidence of degradation or delamination was observed during the process, sign that the pre-processing sterilization have as a matter of fact an influence on the thermoplastic structures.

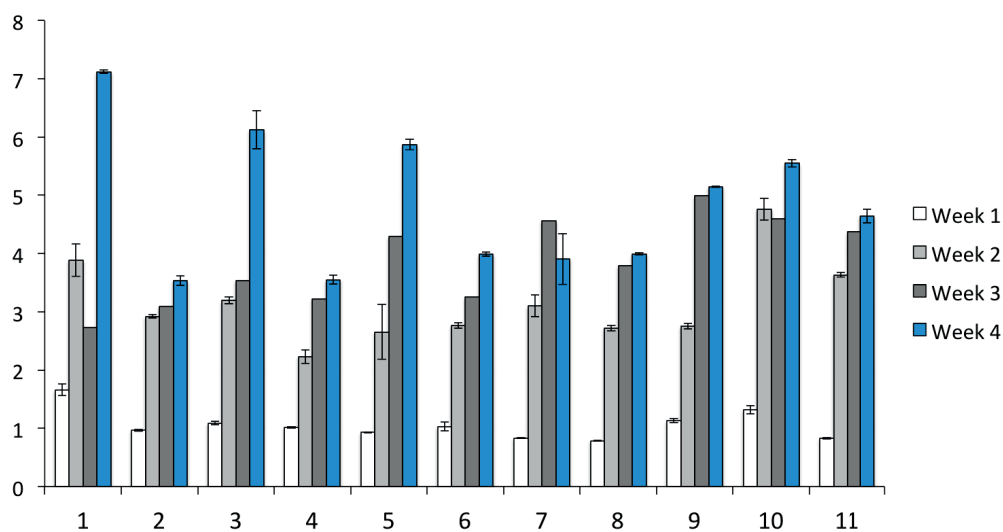


Figure AI.7 Presto Blue assay of mesenchymal stem cells viability on PLAPCL/PLABTCP foams impregnated with alginate after 4 weeks. Cells viability showed to increase from week 1 to week 4 in all samples. However, from week 5 all the structures started degrading, reducing significantly cells viability (data not shown for week 5).

Finally, a statistical analysis was conducted on cells viability evolution in the three systems by Student's test during the first three weeks of culture. As observable in Figure AI.8, all the structures, but the foamed scaffold, expressed a progressive increase of cells viability from week 1 to week 3. For the 3D printed scaffolds, a statistical difference is evicted from week 1 to week 3 ($p < 0.05$) and from week 2 to week 3 ($p < 0.01$), while no difference is shown from week 1 to week 2 ($p > 0.1$). The foamed scaffold showed no significance difference in cells viability from week 1 to week 3 ($p > 0.1$). Finally, the hybrid scaffold Alginate/multi material thermoplastics showed a progressive increase in cells viability from week 1 to week 2 ($p < 0.01$) to week 3 ($p < 0.01$). A weaker increase is showed from week 2 to week 3 ($p < 0.05$). We conclude that cells seeding on a pure thermoplastic scaffold will not be proficient for the final application. A hydrogel as the Alginate is required to keep MSC cells in a friendly medium for the first phase of the implant. Moreover, we believe that even with hydrogel impregnation a functionalization of the multi material scaffold is required to facilitate cells attachment and tissue formation on the surface of the material, improving the interface between the thermoplastics and the hydrogel.

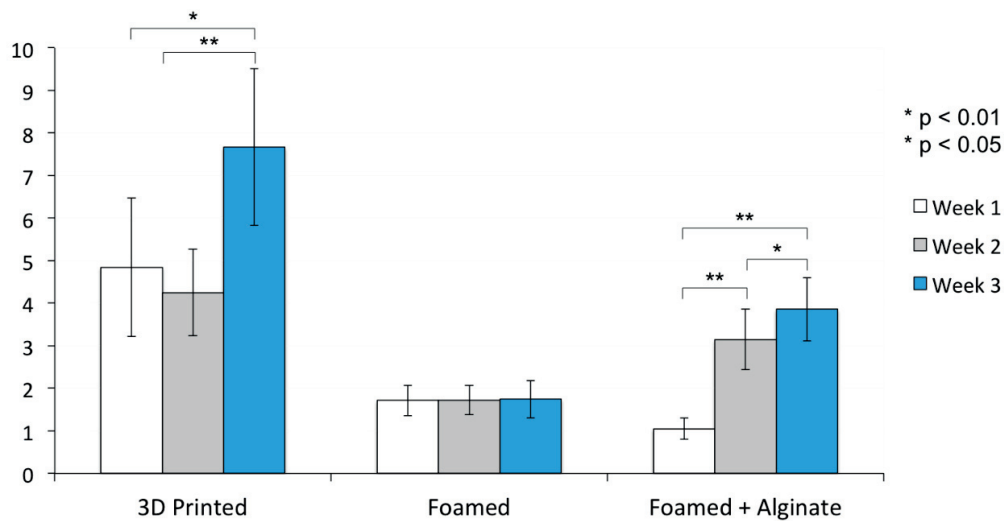


Figure AI.8 Comparison of Presto Blue assay of mesenchymal stem cells viability of PLAPCL/PLABTCP 3D printed scaffold, foam and impregnated foam with alginate. After week 1 the entire set of samples are statistically different ($p < 0.05$). At week 2, no statistical difference has been found between the 3D printed and impregnated scaffolds ($p > 0.1$), while the foamed structures showed a statistical difference with all the other conditions ($p < 0.01$). After week 3, the three scaffolds showed a statistical difference in cells viability ($p < 0.05$). The 3D Printed scaffolds expressed an increase in cell viability from week 2 to week 3 ($p < 0.01$), in accordance with what previously seen. From week 1 to week 2 there is not strong correlation in the data ($p > 0.1$). The foamed scaffolds did not show any change in average from week 1 to week 3, as also expressed by statistical analysis ($p > 0.1$). The impregnated scaffold expressed a constant increase of cells viability from week 1 to week 3 with good statistical correlation ($p < 0.01$ and $p < 0.05$ between week 2 and week 3).

AI.3 Conclusions

This chapter discussed the biocompatibility of some selected scaffolds produced as described in previous chapters and cells viability. It was demonstrated that PLAPCL/PLABTCP would potentially be a good candidate for further in vivo tests, given the good surface cells affinity. However, cells within the scaffolds showed limited proliferation and signs of apoptosis. Dip coating of Collagen I has been proposed as a solution to improve the limited surface cells affinity expressed by thermoplastic scaffolds. The presence of an Alginate hydrogel impregnating the scaffold has shown to improve cells proliferation after 4 weeks of seeding, but cells behaviour at hydrogel-scaffold interface and PLAPCL- PLABTCP interface still need to be addressed with other methods.

Scaffold sterilization has emerged to be a critical point. Autoclave vapour sterilization has shown to trigger scaffold degradation, inducing strand-to-strand delamination and material-material delamination at the interface in multi material scaffolds. An inert method, as EtO treatments or irradiation techniques may be more suited for such low-density structures. A study on the effects of the sterilization process on interfacial strength in 3D printed scaffold would be required to better understand the influence of the process not only at the molecular and surface layer, but also on the mechanicals and fatigue resistance of such geometries.

Finally, smaller and thinner samples would be more practical to be tested and avoid mismanipulation during cells culture management. Also, thinner multi material sample would help better investigate cells behaviour at the material-material interface.

ANNEX II Medical Filaments Extrusion

AII.1 Introduction

The aim of this annex is to describe the method used to produce biopolymer filaments for FDM/FFF. The processing windows to reproduce 1.75 mm filaments from biomaterials in form of granules or flakes are presented. The influence of the processing parameters (extrusion temperature and speed) on the biopolymer filaments crystallinity and degradation is then discussed, illustrating the optimal extrusion conditions.

AII.2 Materials and methods

AII.2.1 Materials

The materials used for filament extrusion are described in Table 3, Chapter 3. PLAm1 was extruded from granules, while PLLA, PLAPCL, PLABTCP, PLAPEG, PLAPGA were extruded from flake form. Blend materials (e.g. PLABTCP and PLAPEG) were mixed for 5 minutes prior the extrusion for homogenization. All materials were dried and stored as described in Chapter 3.

AII.2.2 Characterization

Filament extrusion processing windows were determined using a Noztek Touch extruder, selecting the temperature and motor speed of the extruder to produce 1.75mm diameter filament avoiding to degrade the polymers and to overheat the extruder motor. Lowest achievable temperature (remaining above the melting temperature of the crystalline phase of the material) and motor speed were applied, progressively increasing until the produced filament met the target diameter value of $1.75 \text{ mm} \pm 0.05 \text{ mm}$.

DSC and TGA analysis were performed following the protocols described in Chapter 3.

AII.3 Processing windows

AII.3.1 Food grade model material PLAm1

The processing window obtained for PLAm1 is shown in Figure AII.1. Six ideal conditions were determined out of the applied parameters: 185 °C, 195 °C and 210 °C at 10 and 30 RPM respectively.

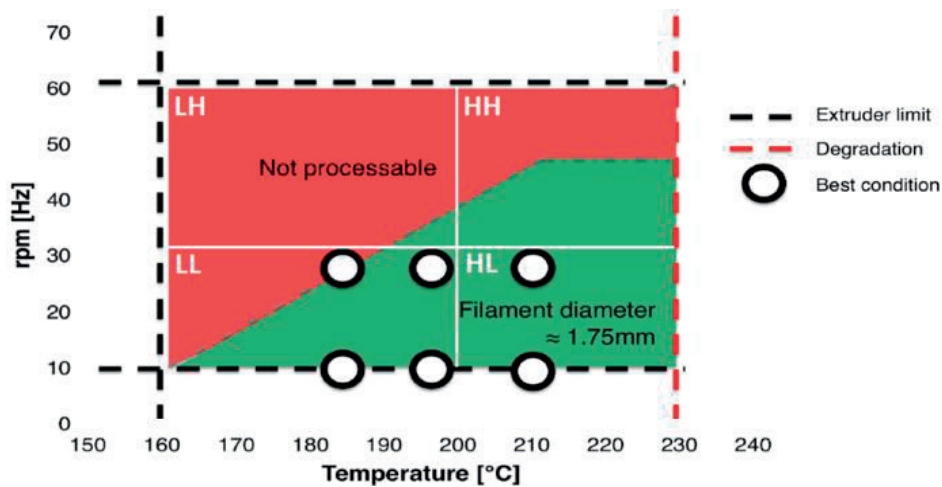


Figure All.1 Processing window to extrude non-medical grade PLAm1 at 1.75 mm filaments for Fused Deposition Modelling.

Four main processing zones were defined:

Low temperature, Low speed (LL)

Positive results were obtained in this zone, providing that the temperature is high enough to ensure a full melting of the polymer. A low extrusion temperature permits to process the material at a higher viscosity and to reduce the time necessary for the filament to cool down and reach room temperature. As a result, a filament with a constant diameter in a range close to the defined set point was obtained. A low extruding speed permits to give enough time to the granules to melt and form a homogeneous mixture inside the extruder, ensuring to obtain a good filament quality.

Low temperature, High speed (LH)

In this zone, the temperature is not high enough to ensure a homogeneous filament in a short amount of time, i.e. at a high extrusion speed. As a result, unmelt granules parts are present in the final filament, resulting in a non-constant diameter and non-homogeneous filament.

High temperature, Low speed (HL)

This zone gave good results. A higher extrusion temperature means that the viscosity of the polymer is reduced. As a result, the extrusion speed must be high enough to ensure that the extrusion flow rate (i.e. the amount of material going through the nozzle per unit time) is high enough to ensure a diameter close to the set point value.

High temperature, High speed (HH)

Under these conditions a filament as good as at low speed was produced. However, extrusion at 45rpm and above was difficult for PLAm1, due to the granules size (about 3mm in diameter), which stressed the motor, caused overheating and non-constant motor speed. As a result, the produced filament did not have a constant diameter.

Another important parameter controlling the obtained filament diameter is the distance between the extruder and the winding system. Despite that a long distance between these two elements is recommended by the Noztek user guide, better results were obtained with a short distance. The influence of this parameter is more important for higher extrusion temperature and speed (HH zone), i.e. at higher extrusion flow rate. Consequently, if a long distance is used in the HH zone, the average filament weight will induce a pulling force at the exit of the extruder head that will diminish the filament diameter, Figure All.2.

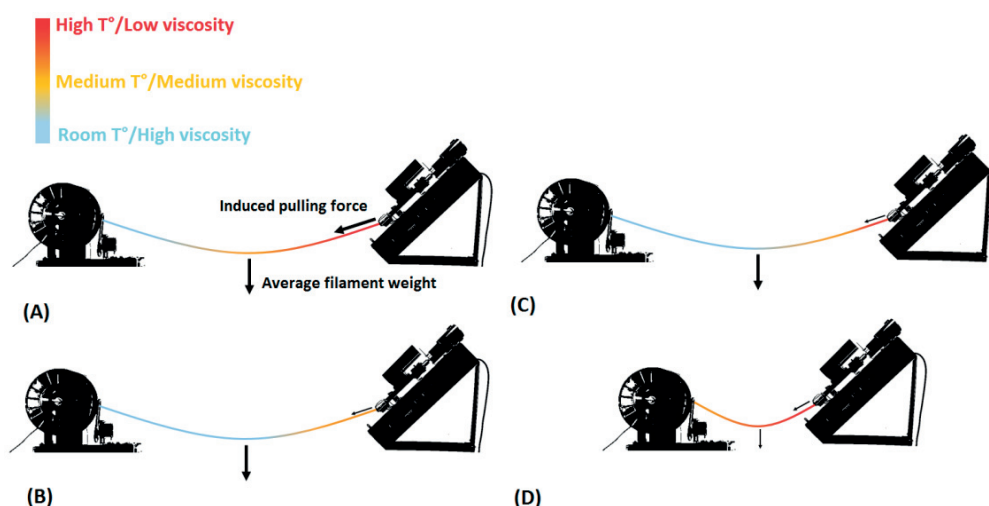


Figure All.2 Influence of the extruding parameters (temperature, speed and distance between the two elements) on the filament diameter: (A) Long distance, high temperature, high speed; (B) Long distance, lower temperature, high speed; (C) Long distance, high temperature, lower speed; (D) Lower distance, high temperature, high speed. Note: the colour code is only indicative and do not represent precise temperature values. This scheme only permits to give a simple representation of a thermo/mechanical phenomenon.

To reduce this effect, three main solutions are possible:

- **Figure All.2B:** A reduction of the extrusion temperature will increase the polymer viscosity at the exit of the extruder, decreasing the intensity of filament average weight on filament diameter.
- **Figure All.2C:** A reduction of the extrusion speed (keeping the initial high extrusion temperature) will give more time to the filament to cool down, decreasing the high temperature zone of the filament. The diameter reduction will be still important directly at the extruder exit but will be diminished on the overall filament as the length of the high temperature zone has been reduced. This explains why a combination of low extrusion temperature and speed permit is ideal to keep a diameter close to the set point value.
- **Figure All.2D:** The last solution consists in decreasing the distance between the two elements to reduce the amount of filament (and thus the average filament weight) waiting to be wound, reducing considerably the induced “pulling effect” at the exit of the extruder. However, as the distance is too small to ensure that the filament has reached room temperature before being wound, the speed of the winding system must be carefully controlled not to induce supplementary pulling on the filament.

AII.3.2 Medical materials

The same processing windows were built for medical grade materials. The following results are not exhaustive. Due to the high price of medical grade materials, only few combinations were tested to emphasize a general behaviour of the materials during extrusion. The processing windows can be refined by testing more extrusion conditions. Figure AII.3 below show the processing window for the different medical grade material.

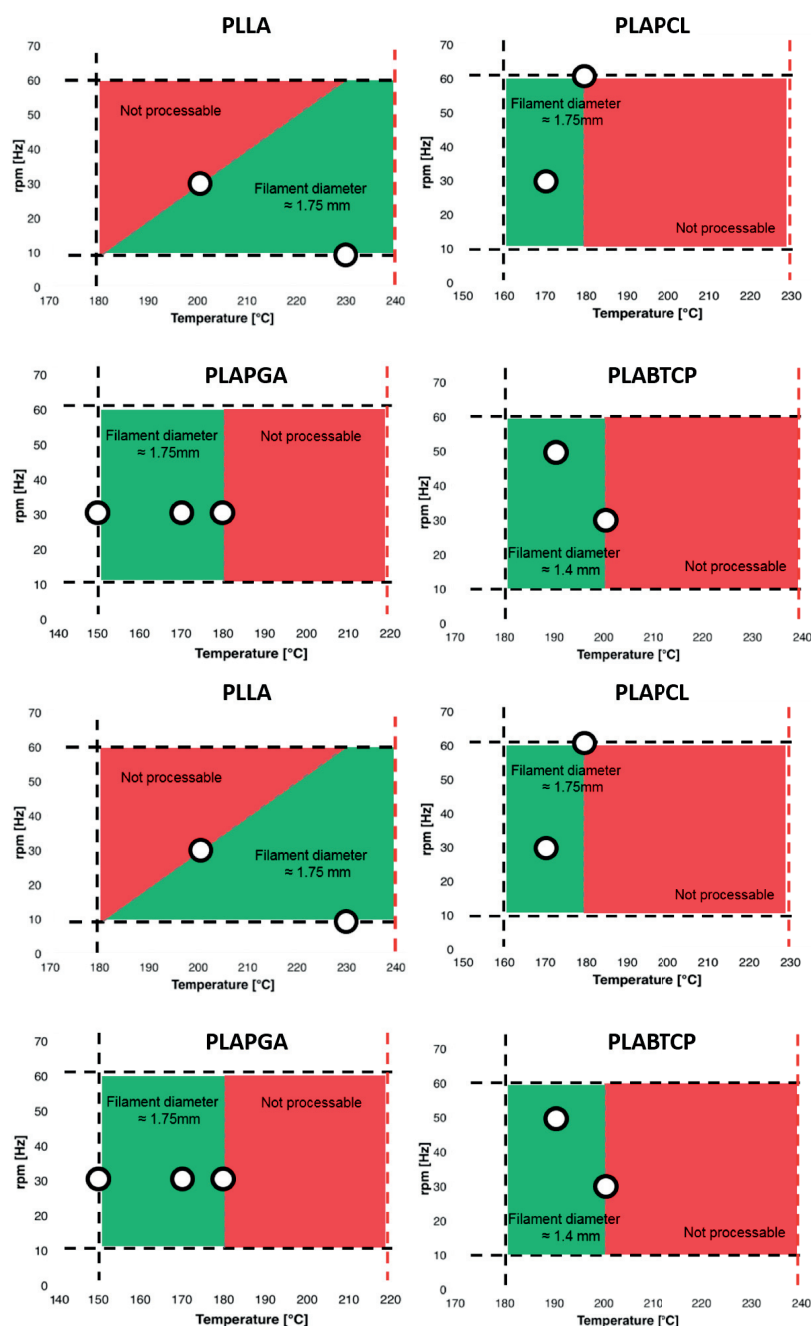


Figure AII.3 Processing window to extrude medical grade filaments of (A) PLLA, (B) PLAPCL, (C) PLAPGA, (D) PLABTCP for Fused Deposition Modelling 3D Printer

PLLA

Two tested conditions have showed to respect the acceptance criteria: 200 °C at 30rpm and 230 °C at 30 rpm, (Figure AII.3A). Differently from PLAm1, the use of PLLA has permitted to reach higher extrusion speed (up to 60 rpm, technical machine limit) and thus process the filament in the HH zone. This is due to the fact that PLLA were received as flacks that are smaller compared to PLAm1 granules, reducing the motor torque (a then overheating phenomenon) necessary to process the polymer.

Compared to PLAm1, higher temperatures were necessary to process PLLA granules. A minimum processing temperature of 180 °C was found. This value corresponds to the melting temperature of the crystalline part of PLLA granules, as shown later during DSC measurements.

The first extrusion test on this material showed that really high temperature were necessary (230 °C that is 50°C above the T_m of the material whereas 25 °C above the T_m of PLAm1 as sufficient to obtain good extrusion conditions) to obtain homogeneous filaments from the medical PLLA flacks. In order to process the material at a lower temperature, a pre-heater system was installed on the extruder, permitting to pre-melt the material around 180 °C and then extrude it at 200 °C.

It was observed that PLLA is more delicate and sensitive to degradation during the processing compared to PLAm1. Indeed, a colour change was observed around 240 °C if the residence time of the polymer was too important, e.g. at low extrusion speed.

PLAPCL

Two low temperature conditions permitted to obtain good filaments: 170 °C at 30 rpm and 180 °C at 60 rpm, Figure AII.3B. Higher temperature conditions were not studied as good results were directly obtained with low temperature condition. The time necessary to cool down this material during extrusion was observed (experimentally) to be more important compared to the other tested materials. As a result, a too high temperature or extrusion speed rendered the production and winding of a good quality filament more difficult. Below 160 °C, it was observed that the temperature was too low to produce a good filament. As shown later in the DSC measurements, the crystalline part of PLAPCL granules (representing around 14% of the material) was found to melt at a temperature close to 160 °C. Below this temperature, the crystalline part of the polymer is not molten, resulting in difficulties to obtain a homogeneous and thus a good quality filament.

Once cooled at room temperature, this material seemed to exhibit viscoelastic properties. When stretched, an elastic material quickly returns to its initial state once the stress is removed, whereas a viscous material deformed irreversibly under the action of external forces. PLAPCL filament showed an intermediate behaviour, i.e. the material could easily be deformed under stress, but needed a certain amount of time (few minutes) to recover its initial shape after stress removal. This behaviour is due to the presence of 30% (molar fraction) of ϵ -caprolactone that soften the filament. This could render the printing step more challenging and could significantly affect the mechanical properties of the obtained scaffold.

PLAPGA

Three ideal conditions were determined out of the applied parameters: 150 °C, 160 °C and 180 °C at 30 rpm, Figure AII.3C. Above 180 °C, it was observed that the viscosity of the polymer became too low to be extruded,

resulting in an amplified effect of the average filament weight, leading to a too small and non-constant filament diameter whatever the value of the extrusion speed. Below 150 °C, the viscosity was too high to produce homogeneous filaments without over-heating the motor. Because PLAPGA granules were found to be fully amorphous the factor limiting extrusion is not the melting temperature of the polymer (as it was the case before for partially crystalline polymers) but an overall too high viscosity of the amorphous polymer.

Based on quick tests, lower and higher extrusion speeds seemed also to produce good filaments; the value of 30 rpm was selected for convenience (to avoid too long extrusion time at 10 rpm and more difficult control of filament winding at extrusion speed above 30 rpm).

PLABTCP

Two conditions were found to give good filament quality: 190 °C at 50 rpm and 200 °C at 30 rpm, Figure AII.3D.

At 180 °C and below, the PLLA flakes seemed to be only partially melted and the viscosity was too high to produce homogeneous filaments without over-heating the motor. Because of the incorporation of the β -TCP ceramic particles, the filament was not transparent anymore but completely opaque with a white colour. As a result, it was quite difficult to be sure that no unmelt PLLA was present within the filament. The only element that could be used as an indicator of the filament homogeneity was the presence/absence of surface roughness, resulting from the presence/absence respectively of unmelt PLLA at the surface of the filament.

Between 200 °C and 210 °C, the filament was well homogenized but the filament diameter was already too far (around 1mm) from the set point value (1.75mm) to be accepted. For temperature higher than 210 °C, the viscosity was too low to control the extrusion process of the blend. Compared to the obtained processing window of pure PLLA where temperature until 230 °C have permitted to obtain good quality filament with a diameter close to 1.75mm, the blending of this same material with 10wt% of β -TCP ceramic powder have strongly modified its processing window. As explained before, the lower temperature limit of 180°C in the processing window was due to the melting temperature of the PLLA, whereas the highest temperature reachable was observed to be affected by β -TCP ceramic powder. Indeed, the incorporation of β -TCP considerably lowered the filament diameter during the extrusion process at both low and high temperature (a maximum of 1.4mm was reached). This phenomenon was amplified at higher temperature and thus at lower viscosity of the polymer.

PLAPEG

For this blend, no processing window was established because of the difficulty encountered to extrude this copolymer. Only one couple extrusion temperature/motor speed has permitted to obtain a good quality filament: 170 °C at 60rpm.

At $T_{ext} = 180$ °C, temperature corresponding to the melting temperature of pure PLLA and PLAPEG, the viscosity of the blend seemed to be already too low to be extruded, prohibiting the material accumulation and thus the pressure increase before the extruder nozzle, necessary phenomenon for normal extrusion condition. To obtain a good quality filament, it was necessary to decrease the extruding temperature to 170 °C that is below the theoretical melting temperature of the crystalline part of PLLA and extrude the material at the maximum motor speed (60rpm) to ensure a high enough polymer flow during the process. This condition

below the melting temperature did not prevent to obtain homogeneous filament, a diameter close to 1.6mm was successfully obtained.

AII.4 Processing influence on filaments and 3D printed structure properties

In this part, the influence of the extruding and 3D Printing process on material crystallinity was investigated. The impact of processing on material glass transition temperature (T_g), cold crystallization temperature (T_c), and melting temperature (T_m) was also explored. Finally, the influence of blending elements on these parameters was highlighted. Table 10 summarize the influence of the extrusion process (i.e. from the granule to the filament), extrusion parameters (i.e. filament only) and 3D printing process (i.e. from the filament to the scaffold) on materials T_g , T_c , T_m and λ_c . Figure AII.6 shows the degree of crystallinity for the different systems at the state of raw granules, extruded filament and printed scaffold.

Table 10 Influence of the filament extrusion process and 3D printing process on materials T_g , T_c , T_m and λ_c .

MATERIAL	SAMPLES		T_g [°C]	T_c [°C]	T_m [°C]	λ_c [%]
PLAm1	Granules		55	-	-	0
	Filament	T_{ext} =185°C, ω_{ext} =10	57	132	153	0
		T_{ext} =185°C, ω_{ext} =30	57	131	153	0
		T_{ext} =195°C, ω_{ext} =10	57	132	153	0
		T_{ext} =195°C, ω_{ext} =30	57	131	152	0
		T_{ext} =210°C, ω_{ext} =10	59	132	153	0
		T_{ext} =210°C, ω_{ext} =30	57	131	153	0
	Scaffold		62	126	153	1
PLLA	Granules		57	139	177	1
	Filament	T_{ext} =200°C, ω_{ext} =30	60	123	182	0
		T_{ext} =230°C, ω_{ext} =10	61	120	182	0
	Scaffold		62	114	181	4
PLAPCL	Filament	Granules	-	121	158	2
		T_{ext} =170°C, ω_{ext} =30	-	87	161	4
		T_{ext} =180°C, ω_{ext} =60	-	86	162	4
	Scaffold		-	85	161	4
PLAPGA	Granules		57	-	-	0
	Filament	T_{ext} =150°C, ω_{ext} =30	57	140	163	1
		T_{ext} =170°C, ω_{ext} =30	59	140	162	0
		T_{ext} =180°C, ω_{ext} =30	55	140	163	1
	Scaffold		54	129	162	0
PLABTCP	Granules		60	139	179	4
	Filament	T_{ext} =190°C, ω_{ext} =50	61	106	181	6
		T_{ext} =200°C, ω_{ext} =30	61	103	181	6
	Scaffold		62	101	181	5

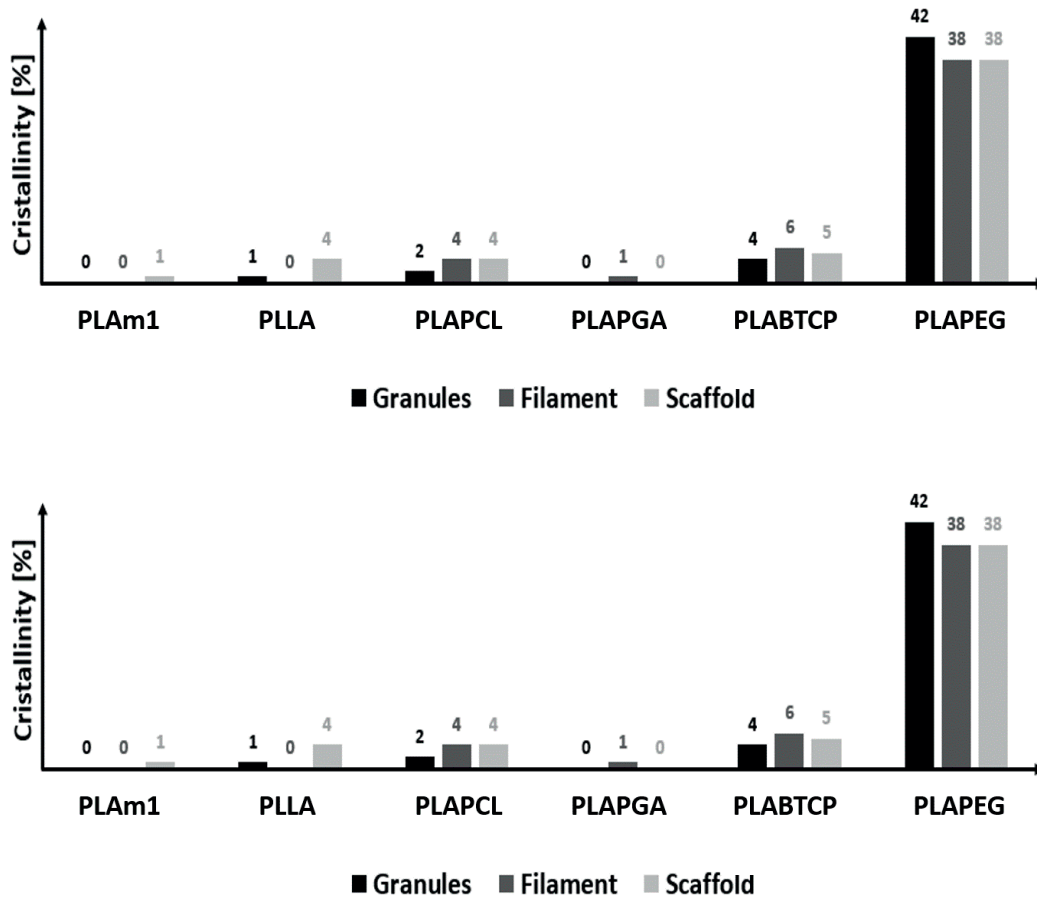


Figure All.4 Degree of crystallinity for the different systems at the state of raw granules extruded filament and printed scaffold.

From Table All.1 and Figure All.4, few key points can be highlighted:

- The extrusion and 3D printing process do not significantly influence the value of the degree of crystallinity λ_c . However, variation of T_g , T_c , T_m in the DSC curves are observed mainly during extrusion (from the granule to the filament) that constitutes the first processing step. These internal changes in the material did not affect the values of the obtained crystallinity.
- No influence of extrusion parameters (temperature and motor speed) on T_g , T_c , T_m and λ_c was observed. Even if the 3D Printing process seems not to have influence on these variables, the influence of 3D Printing parameters (temperature, printing speed, etc...) could be the next area to explore.
- All the systems can be considered to be amorphous at the state of raw pellets, extruded filament and printed scaffold except PLA207s/PEG 35000 system that showed a degree of crystallinity close to 40 %.
- The incorporation of blending elements influences material crystallinity by different physical phenomena (nucleating agent with β TCP ceramics particles, enhanced mobility by plasticiza-

tion). Controlling material crystallinity is crucial because it directly affect other material properties such as viscosity, transparency, permeability, and mechanical properties and to go further, *in vivo* behaviours.

The influence of the extrusion parameters (temperature/motor speed) and the extrusion/3D Printing process on the thermal stability (degradation temperature T_D) and kinetic of degradation (degradation rate r_D) of the different systems are shown in Figure All.5.

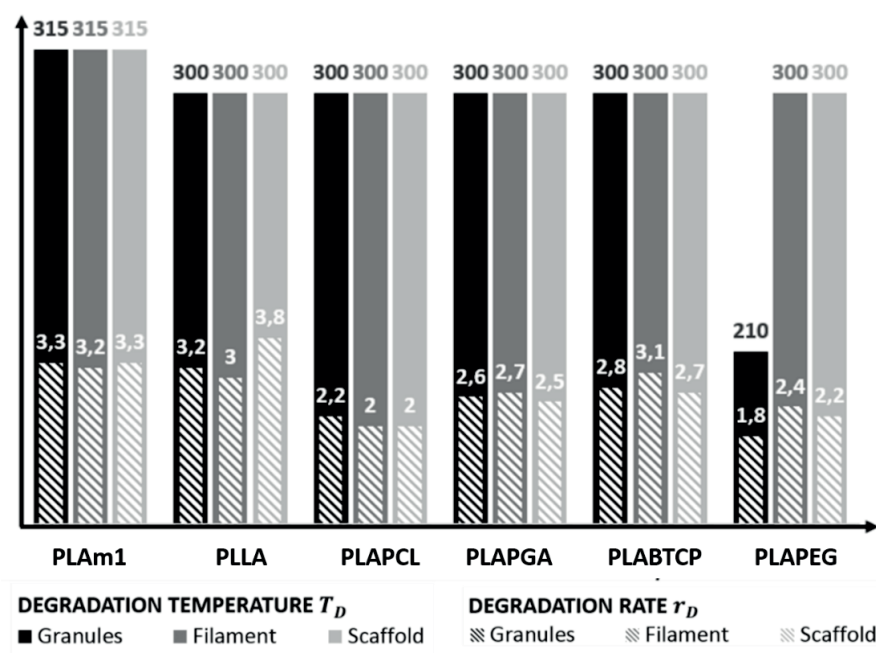


Figure All.5 Summary of the degradation temperature T_D and degradation rate r_D (absolute value of the slope) for the different systems.

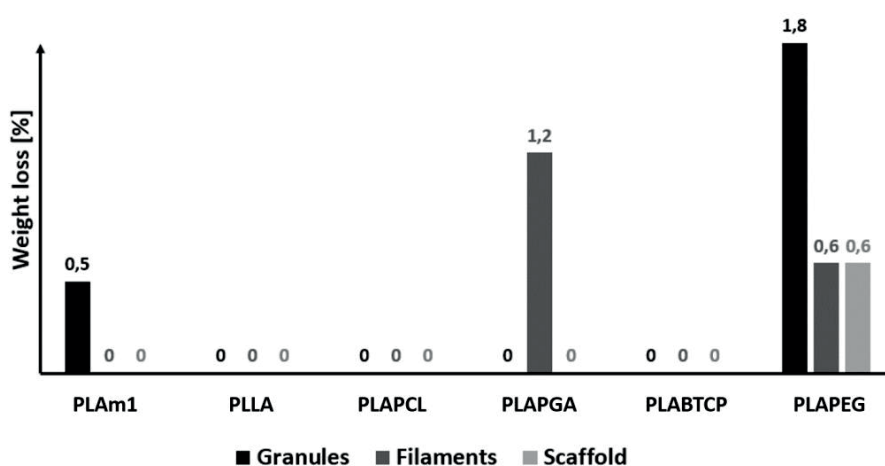


Figure All.6 Weight loss during TGA analysis for each of the produced material.

From Figure AII.6, it is observed that no significant thermal degradation is observed for all the systems, including PLAPGA granules/scaffold and PLAPEG filaments/scaffold whereas a more important thermal degradation is observed for PLALG855s filament and PLABTCP granules.

However, the values of the weight losses remain relatively small considering the fact that an important residence time (10min) of the material inside the device was considered. In order to limit the effect of thermal degradation of the material during the different processing steps, lowest processing temperature as possible must be used.

It might be observed that samples have a mass that is going above their initial value of 100 %. This was due to a simple artefact of the TGA device. The sample holder and the weighting system are separated into two distinct chambers (while being interconnected), respectively chamber 1 and chamber 2. When doing measurements in air environment, these two chambers are filled with air. In the chamber 1 containing the sample holder, the air will undergo the temperature cycle defined for the measurement whereas the air inside the chamber 2 will stay at room temperature, protecting the weighting system. As the temperature increase, the air in the chamber 1 will expand, inducing an additional pressure on the weighting system, explaining the measured value of the weight above 100 %. This artefact is in the order of 1-2 % of the total sample mass. As a result, the weight losses in the Figure AII.6 were calculated subtracting the initial weight of the sample (i.e. 100 %, removing the contribution of the artefact) by the minimum value of the weight percentage at the end of the test.

Few key points can be highlighted:

- The processing (extrusion and 3D Printing) and the extrusion parameters did not significantly affect the values of T_D and r_D for the different systems. Value of T_D close to 315 °C/300 °C respectively for PLAm1 and the medical grades materials were found. It is then assumed that, within the processing windows, material conditions are maintained. As the extrusion/3D printing temperature ranges are well below the degradation temperature, no degradation should happen to the granules/filaments/scaffold respectively during processing. As two systems were shown to be more sensitive to thermal degradation (PLAPGA filament and PLABTCP granules), the lowest processing temperature possible must be used to limit preliminary thermal degradation of the material. More investigation must be carried out to better understand the phenomena controlling the degradation process in the more sensitive copolymers.
- Blending did not affect the value of T_D but decreased the value of r_D , especially for PLAPCL and PLAPEG. An interesting further step would be to analyse the effect of the concentration of the blending elements on both T_D and r_D parameters.

AII.5 Conclusions

Neat thermoplastic granules and powders were successfully processed into 1.75 mm filaments for FDM/FFF machines. Different protocols were drawn from different material systems, producing neat Poly(L-lactide) (PLLA), blend (PLAPEG), copolymer (PLAPCL, PLAPGA) and composite (PLABTCP) filaments. It was demonstrated that different materials shall be processed under different extrusion conditions (e.g. temperature and

motor speed) to better control filaments diameter. This was essential to 3D print precise structures as shown in Chapter 4 and Chapter 5.

The influence of all the processing conditions at the different processing stages (extrusion of granules/powder into filaments and 3D printing of filaments into 3D structure in the was determined on two material properties: crystallinity and degradation. None of the processing phases introduced a significant modification of the materials properties. This is an index of good processing windows, which do not affect the material during the transformation. The original crystallinity is maintained, while no degradation has been observed in the samples, preserving the mechanical properties of the neat material.

BIBLIOGRAPHY

1. Baur, J. & Silverman, E. Challenges and Opportunities in Multifunctional Nanocomposite Structures for Aerospace Applications. *MRS Bulletin* **32**, 328–334 (2007).
2. Noor, A. K., Venneri, S. L., Paul, D. B. & Hopkins, M. A. Structures technology for future aerospace systems. *Comput. Struct.* **74**, 507–519 (2000).
3. Månson, J.-A.E., Wakeman, M.D., and Bernet, N. *Composite Processing and Manufacturing - An Overview, in Comprehensive Composite Materials.* (2000).
4. Bhosale, a. M. & Richardson, J. B. Articular cartilage: structure, injuries and review of management. *Br. Med. Bull.* **87**, 77–95 (2008).
5. Mano, J. & Reis, R. Osteochondral defects: present situation and tissue engineering approaches. *J. tissue Eng. ...* 261–273 (2007). doi:10.1002/term
6. O'Shea, T. M. & Miao, X. Bilayered scaffolds for osteochondral tissue engineering. *Tissue Eng. Part B. Rev.* **14**, 447–464 (2008).
7. Cheung, H. Y., Lau, K. T., Lu, T. P. & Hui, D. A critical review on polymer-based bio-engineered materials for scaffold development. *Compos. Part B Eng.* **38**, 291–300 (2007).
8. Temenoff, J. S. & Mikos, A. G. Review: Tissue engineering for regeneration of articular cartilage. *Biomaterials* **21**, 431–440 (2000).
9. Izadifar, Z., Chen, X. & Kulyk, W. Strategic Design and Fabrication of Engineered Scaffolds for Articular Cartilage Repair. *J. Funct. Biomater.* **3**, 799–838 (2012).
10. Gibson, L.J. and Ashby, M. F. *Cellular Solids: Structure and Properties.* (1999).
11. Mathieu, L. M., Bourban, P. E. & Månson, J. A. E. Processing of homogeneous ceramic/polymer blends for bioresorbable composites. *Compos. Sci. Technol.* **66**, 1606–1614 (2006).
12. Howdle, S.M., Watson, M.S., Whitaker, M.J., Popov, V.K., Davies, M.C., Mandel, F.S., Wang, J.D., and Shakesheff, K. M. Supercritical fluid mixing: preparation of thermally sensitive polymer composites containing bioactive materials. *Chem. Commun.* 109–110 (2001).
13. Chua, C. K., Liu, M. J. J. & Chou, S. M. Additive Manufacturing-assisted scaffold-based Tissue Engineering. 13–21 (2012).
14. Melchels, F. P. W. *et al.* Additive manufacturing of tissues and organs. *Prog. Polym. Sci.* **37**, 1079–1104 (2012).
15. Malda, J. *et al.* 25th anniversary article: Engineering hydrogels for biofabrication. *Adv. Mater.* **25**, 5011–28 (2013).
16. Visser, J. *et al.* Biofabrication of multi-material anatomically shaped tissue constructs. *Biofabrication* **5**, 35007 (2013).
17. Boere, K. W. M. *et al.* Covalent attachment of a three-dimensionally printed thermoplast to a gelatin hydrogel for mechanically enhanced cartilage constructs. *Acta Biomaterialia* (2014). doi:10.1016/j.actbio.2014.02.041

BIBLIOGRAPHY

18. Prabhu, S., Raja, V. K. B. & Nikhil, R. Applications of Cellular Materials – An Overview. *Appl. Mech. Mater.* **766–767**, 511–517 (2015).
19. Banhart, J. Manufacture, characterisation and application of cellular metals and metal foams. *Progress in Materials Science* **46**, 559–632 (2001).
20. Gibson, L. J. & Ashby, M. . *Cellular Solids, structure and properties*. Cambridge university press (1997). doi:10.1557/mrs2003.79
21. Harris, L. D., Kim, B. S. & Mooney, D. J. Open pore biodegradable matrices formed with gas foaming. *J. Biomed. Mater. Res.* **42**, 396–402 (1998).
22. Murphy, C. M., Haugh, M. G. & O'Brien, F. J. The effect of mean pore size on cell attachment, proliferation and migration in collagen-glycosaminoglycan scaffolds for bone tissue engineering. *Biomaterials* **31**, 461–466 (2010).
23. Mathieu, L. Processing of porous polymer composites for bone tissue engineering, in Laboratoire de Technologie des Composites et Polymères (LTC). (Ecole Polytechnique Federale de Lausanne (EPFL), 2005).
24. Wolcott, M. P. Cellular solids: Structure and properties. *Materials Science and Engineering: A* **123**, 282–283 (1990).
25. Carletti, E., Motta, A. & Migliaresi, C. Scaffolds for tissue engineering and 3D cell culture. *Methods Mol. Biol.* **695**, 17–39 (2011).
26. Nam, Y. S. & Park, T. G. Porous biodegradable polymeric scaffolds prepared by thermally induced phase separation. *J. Biomed. Mater. Res.* **47**, 8–17 (1999).
27. Thadavirul, N., Pavasant, P. & Supaphol, P. Development of polycaprolactone porous scaffolds by combining solvent casting, particulate leaching, and polymer leaching techniques for bone tissue engineering. *J. Biomed. Mater. Res. - Part A* **102**, 3379–3392 (2014).
28. Cao, Y., Croll, T. I., Lees, J. G., Tuch, B. E. & Cooper-White, J. J. Scaffolds, stem cells, and tissue engineering: A potent combination! *Australian Journal of Chemistry* **58**, 691–703 (2005).
29. Lin, W. J. & Lu, C. H. Characterization and permeation of microporous poly(ϵ -caprolactone) films. *J. Memb. Sci.* **198**, 109–118 (2002).
30. Japon, S. Modification moléculaire du poly(éthylène téréphtalate) par mise en oeuvre réactive pour le contrôle dynamique du moussage. (Ecole Polytechnique Federale de Lausanne (EPFL), 1999).
31. Mathieu, L. M., Montjovent, M. O., Bourban, P. E., Pioletti, D. P. & Manson, J. A. E. Bioresorbable composites prepared by supercritical fluid foaming. *J. Biomed. Mater. Res. - Part A* **75**, 89–97 (2005).
32. Mathieu, L. M. *et al.* Architecture and properties of anisotropic polymer composite scaffolds for bone tissue engineering. *Biomaterials* **27**, 905–916 (2006).
33. Kim, S.-S., Sun Park, M., Jeon, O., Yong Choi, C. & Kim, B.-S. Poly(lactide-co-glycolide)/hydroxyapatite composite scaffolds for bone tissue engineering. *Biomaterials* **27**, 1399–1409 (2006).
34. Ignatius, A. A., Betz, O., Augat, P. & Claes, L. E. In vivo investigations on composites made of resorbable ceramics and poly(lactide) used as bone graft substitutes. *J. Biomed. Mater. Res.* **58**, 701–709 (2001).
35. Bühler, M. rocessing of fibre and porosity gradients in cellular thermoplastic composites, in

BIBLIOGRAPHY

- Laboratoire de Technologie des Composites et Polymères (LTC). (Ecole Polytechnique Federale de Lausanne (EPFL): Lausanne., 2008).
36. Bühler, M., Bourban, P. E. & Månson, J. A. E. Cellular composites based on continuous fibres and bioresorbable polymers. *Compos. Part A Appl. Sci. Manuf.* **39**, 1779–1786 (2008).
 37. Bühler, M., Bourban, P. E. & Månson, J. A. E. Cellular thermoplastic composites with microstructural gradients of fibres and porosity. *Compos. Sci. Technol.* **68**, 820–828 (2008).
 38. Cooper, A. I. Polymer synthesis and processing using supercritical carbon dioxide. *Journal of Materials Chemistry* **10**, 207–234 (2000).
 39. Cuénoud, M. Hybrid Polymer Foams for Osteochondral Tissue Engineering. (École polytechnique fédérale de Lausanne - EPFL, 2013).
 40. Woodruff, M. A. & Hutmacher, D. W. The return of a forgotten polymer—Polycaprolactone in the 21st century. *Progress in Polymer Science* **35**, 1217–1256 (2010).
 41. Peltola, S. M., Melchels, F. P. W., Grijpma, D. W. & Kellomäki, M. A review of rapid prototyping techniques for tissue engineering purposes. *Ann. Med.* **40**, 268–280 (2008).
 42. Hollister, S. J. Porous scaffold design for tissue engineering. *Nat. Mater.* **4**, 518–524 (2005).
 43. Ballyns, J. J. & Bonassar, L. J. Image-guided tissue engineering. *J. Cell. Mol. Med.* **13**, 1428–1436 (2009).
 44. Vaezi, M., Seitz, H. & Yang, S. A review on 3D micro-additive manufacturing technologies. doi:10.1007/s00170-012-4605-2
 45. de Gans, B. J., Duineveld, P. C. & Schubert, U. S. Inkjet Printing of Polymers: State of the Art and Future Developments. *Adv. Mater.* **16**, 203–213 (2004).
 46. Melchels, F. P. W. *et al.* Additive manufacturing of tissues and organs. *Progress in Polymer Science* **37**, 1079–1104 (2012).
 47. Schmid, M. & Wegener, K. Additive Manufacturing: Polymers applicable for laser sintering (LS). in *Procedia Engineering* **149**, 457–464 (2016).
 48. Hutmacher, D. W. Scaffolds in tissue engineering bone and cartilage. *Biomaterials* **21**, 2529–2543 (2000).
 49. Bates, S. R. G., Farrow, I. R. & Trask, R. S. 3D printed polyurethane honeycombs for repeated tailored energy absorption. *Mater. Des.* **112**, 172–183 (2016).
 50. Hutmacher, D. W. *et al.* Mechanical properties and cell cultural response of polycaprolactone scaffolds designed and fabricated via fused deposition modeling. *J. Biomed. Mater. Res.* **55**, 203–216 (2001).
 51. Serra, T., Planell, J. A. & Navarro, M. High-resolution PLA-based composite scaffolds via 3-D printing technology. *Acta Biomater.* **9**, 5521–5530 (2013).
 52. Bose, S., Vahabzadeh, S. & Bandyopadhyay, A. Bone tissue engineering using 3D printing. *Mater. Today* **16**, 496–504 (2013).
 53. Korpela, J. *et al.* Biodegradable and bioactive porous scaffold structures prepared using fused deposition modeling. *J. Biomed. Mater. Res. - Part B Appl. Biomater.* **101**, 610–619 (2013).
 54. Utrecht, U. 3D-Printed skull implanted in patient. (2014).

BIBLIOGRAPHY

55. Yang, P. J. & Temenoff, J. S. Engineering orthopedic tissue interfaces. *Tissue Eng. Part B. Rev.* **15**, 127–141 (2009).
56. Shimomura, K. & Moriguchi, Y. Osteochondral tissue engineering with biphasic scaffold: Current strategies and techniques. ... *Eng.* **0**, (2014).
57. Beris, A. E., Lykissas, M. G., Papageorgiou, C. D. & Georgoulis, A. D. Advances in articular cartilage repair. *Injury* **36 Suppl 4**, S14-23 (2005).
58. Hoppe, A., Güldal, N. S. & Boccaccini, A. R. A review of the biological response to ionic dissolution products from bioactive glasses and glass-ceramics. *Biomaterials* **32**, 2757–74 (2011).
59. Jiang, J. *et al.* Bioactive stratified polymer ceramic-hydrogel scaffold for integrative osteochondral repair. *Ann. Biomed. Eng.* **38**, 2183–96 (2010).
60. Mano, J. F. & Reis, R. L. Osteochondral defects: Present situation and tissue engineering approaches. *J. Tissue Eng. Regen. Med.* **1**, 261–273 (2007).
61. Loh, Q. L. & Choong, C. Three-Dimensional Scaffolds for Tissue Engineering Applications: Role of Porosity and Pore Size. *Tissue Eng. Part B Rev.* **19**, 485–502 (2013).
62. Yoo, H. S., Kim, T. G. & Park, T. G. Surface-functionalized electrospun nanofibers for tissue engineering and drug delivery. *Advanced Drug Delivery Reviews* **61**, 1033–1042 (2009).
63. Hutmacher, D. W. & Dalton, P. D. Melt electrospinning. *Chemistry - An Asian Journal* **6**, 44–56 (2011).
64. Dalton, P. D. *et al.* Electrospinning and additive manufacturing: converging technologies. *Biomater. Sci.* **1**, 171–185 (2013).
65. Chang, K. Y., Hung, L. H., Chu, I. M., Ko, C. S. & Lee, Y. Der. The application of type II collagen and chondroitin sulfate grafted PCL porous scaffold in cartilage tissue engineering. *J. Biomed. Mater. Res. - Part A* **92**, 712–723 (2010).
66. Liu, A. *et al.* Surface modification of bioactive glass nanoparticles and the mechanical and biological properties of poly(l-lactide) composites. *Acta Biomater.* **4**, 1005–1015 (2008).
67. Ma, Z., Gao, C., Gong, Y. & Shen, J. Cartilage tissue engineering PLLA scaffold with surface immobilized collagen and basic fibroblast growth factor. *Biomaterials* **26**, 1253–1259 (2005).
68. Goddard, J. M. & Hotchkiss, J. H. Polymer surface modification for the attachment of bioactive compounds. *Progress in Polymer Science (Oxford)* **32**, 698–725 (2007).
69. Murphy, W. L., Peters, M. C., Kohn, D. H. & Mooney, D. J. Sustained release of vascular endothelial growth factor from mineralized poly(lactide-co-glycolide) scaffolds for tissue engineering. *Biomaterials* **21**, 2521–2527 (2000).
70. Li, C., Vepari, C., Jin, H.-J., Kim, H. J. & Kaplan, D. L. Electrospun silk-BMP-2 scaffolds for bone tissue engineering. *Biomaterials* **27**, 3115–3124 (2006).
71. Aydin, H. M. A three-layered osteochondral plug: Structural, mechanical, and in vitro biocompatibility analysis. *Adv. Eng. Mater.* **13**, (2011).
72. Schek, R. M., Taboas, J. M., Hollister, S. J. & Krebsbach, P. H. Tissue engineering osteochondral implants for temporomandibular joint repair. *Orthod. Craniofacial Res.* **8**, 313–319 (2005).

BIBLIOGRAPHY

73. Ghosh, S., Viana, J. C., Reis, R. L. & Mano, J. F. Bi-layered constructs based on poly(l-lactic acid) and starch for tissue engineering of osteochondral defects. *Mater. Sci. Eng. C* **28**, 80–86 (2008).
74. Rezwan, K., Chen, Q. Z., Blaker, J. J. & Boccaccini, A. R. Biodegradable and bioactive porous polymer/inorganic composite scaffolds for bone tissue engineering. *Biomaterials* **27**, 3413–3431 (2006).
75. Mohamad Yunus, D., Bretcanu, O. & Boccaccini, A. R. Polymer-bioceramic composites for tissue engineering scaffolds. in *Journal of Materials Science* **43**, 4433–4442 (2008).
76. Drury, J. L. & Mooney, D. J. Hydrogels for tissue engineering: Scaffold design variables and applications. *Biomaterials* **24**, 4337–4351 (2003).
77. Hoffman, A. S. Hydrogels for biomedical applications. *Advanced Drug Delivery Reviews* **64**, 18–23 (2012).
78. Smeds, K. A. & Grinstaff, M. W. Photocrosslinkable polysaccharides for in situ hydrogel formation. *J. Biomed. Mater. Res.* **54**, 115–121 (2001).
79. Li, X. *et al.* In situ injectable nano-composite hydrogel composed of curcumin, N,O-carboxymethyl chitosan and oxidized alginate for wound healing application. *Int. J. Pharm.* **437**, 110–119 (2012).
80. Schmocker, A. *et al.* A photopolymerized composite hydrogel and surgical implanting tool for a nucleus pulposus replacement. *Biomaterials* **88**, 110–119 (2016).
81. Xynos, I. D. *et al.* Bioglass 45S5 Stimulates Osteoblast Turnover and Enhances Bone Formation In Vitro: Implications and Applications for Bone Tissue Engineering. 321–329 (2000). doi:10.1007/s002230001134
82. Alves da Silva, M. L. *et al.* Chitosan/polyester-based scaffolds for cartilage tissue engineering: assessment of extracellular matrix formation. *Acta Biomater.* **6**, 1149–57 (2010).
83. Fithian, D. C., Kelly, M. a & Mow, V. C. Material properties and structure-function relationships in the menisci. *Clin. Orthop. Relat. Res.* 19–31 (1990). doi:10.2144/000113917
84. Kempson, G. E., Freeman, M. A. & Swanson, S. A. Tensile properties of articular cartilage. *Nature* **220**, 1127–8 (1968).
85. Jurvelin, J. S. *et al.* Surface and Subsurface Morphology of Bovine Humeral Articular Cartilage as Assessed by Atomic Force and Transmission Electron Microscopy. *J. Struct. Biol.* **117**, 45–54 (1996).
86. Korhonen, R. K. *et al.* Comparison of the equilibrium response of articular cartilage in unconfined compression, confined compression and indentation. *J. Biomech.* **35**, 903–909 (2002).
87. Roth, V. & Mow, V. C. The intrinsic tensile behavior of the matrix of bovine articular cartilage and its variation with age. *J. Bone Joint Surg. Am.* **62**, 1102–17 (1980).
88. Oh, S. H., Kim, T. H., Im, G. II & Lee, J. H. Investigation of pore size effect on chondrogenic differentiation of adipose stem cells using a pore size gradient scaffold. *Biomacromolecules* **11**, 1948–1955 (2010).
89. Wu, H. *et al.* Fabrication of chitosan-g-polycaprolactone copolymer scaffolds with gradient porous microstructures. *Mater. Lett.* **62**, 2733–2736 (2008).
90. Schoof, H., Apel, J., Heschel, I. & Rau, G. Control of pore structure and size in freeze-dried collagen

BIBLIOGRAPHY

- sponges. *J. Biomed. Mater. Res.* **58**, 352–357 (2001).
91. Nie, T., Xue, L., Ge, M., Ma, H. & Zhang, J. Fabrication of poly(L-lactic acid) tissue engineering scaffolds with precisely controlled gradient structure. *Mater. Lett.* **176**, 25–28 (2016).
 92. Puppi, D. *et al.* Additive manufacturing of wet-spun polymeric scaffolds for bone tissue engineering. *Biomed. Microdevices* **14**, 1115–1127 (2012).
 93. Liu, H. *et al.* Biomimetic tendon extracellular matrix composite gradient scaffold enhances ligament-to-bone junction reconstruction. *Acta Biomater.* **56**, 129–140 (2017).
 94. Nicholas, S., Prechi, D., Whitely, M. & Elizabeth, C.-H. Fabrication of biomimetic bone grafts with multi-material 3D printing. *Biofabrication* **9**, 25020 (2017).
 95. Hunter, W. Of the Structure and Diseases of Articulating Cartilages, by William Hunter, Surgeon. *Philosophical Transactions of the Royal Society of London* **42**, 514–521 (1742).
 96. Niederauer, G. G. *et al.* Evaluation of multiphase implants for repair of focal osteochondral defects in goats. *Biomaterials* **21**, 2561–2574 (2000).
 97. Tuli, R. *et al.* Human mesenchymal progenitor cell-based tissue engineering of a single-unit osteochondral construct. *Tissue Eng.* **10**, 1169–1179 (2004).
 98. Akizuki, S., Mow, V. C., Muller, F., Pita, J. C. & Howell, D. S. Tensile properties of human knee joint cartilage. II. Correlations between weight bearing and tissue pathology and the kinetics of swelling. *J. Orthop. Res.* **5**, 173–186 (1987).
 99. Madry, H., Ochi, M., Cucchiaroni, M., Pape, D. & Seil, R. Large animal models in experimental knee sports surgery: focus on clinical translation. *J Exp Orthop* **2**, 1–12 (2015).
 100. Goldring, M. B. Osteoarthritis and cartilage: the role of cytokines. *Curr. Rheumatol. Rep.* **2**, 459–465 (2000).
 101. Fortier, L. a, Barker, J. U., Strauss, E. J., McCarrel, T. M. & Cole, B. J. The role of growth factors in cartilage repair. *Clin. Orthop. Relat. Res.* **469**, 2706–15 (2011).
 102. Solchaga, L. A. *et al.* Treatment of osteochondral defects with autologous bone marrow in a hyaluronan-based delivery vehicle. *Tissue Eng.* **8**, 333–347 (2002).
 103. Wilder, F. V., Hall, B. J., Barrett, J. P. & Lemrow, N. B. History of acute knee injury and osteoarthritis of the knee: A prospective epidemiological assessment. The Clearwater Osteoarthritis Study. *Osteoarthr. Cartil.* **10**, 611–616 (2002).
 104. Langer, R. & Vacanti, J. P. Tissue Engineering. *Science (80-.)*. **260**, 920–926 (1993).
 105. Marga, F. *et al.* Toward engineering functional organ modules by additive manufacturing. *Biofabrication* **4**, 22001 (2012).
 106. Meyvis, T. K. L. *et al.* A comparison between the use of dynamic mechanical analysis and oscillatory shear rheometry for the characterisation of hydrogels. *Int. J. Pharm.* **244**, 163–168 (2002).
 107. Nooeaid, P., Salih, V., Beier, J. P. & Boccaccini, A. R. Osteochondral tissue engineering: Scaffolds, stem cells and applications. *J. Cell. Mol. Med.* **16**, 2247–2270 (2012).
 108. Hutmacher, D. W. Scaffolds in tissue engineering bone and cartilage. *Biomaterials* **21**, 2529–43 (2000).

BIBLIOGRAPHY

109. Ahsan, T. & Sah, R. L. Biomechanics of integrative cartilage repair. *Osteoarthr. Cartil.* **7**, 29–40 (1999).
110. Khan, I. M., Gilbert, S. J., Singhrao, S. K., Duance, V. C. & Archer, C. W. Cartilage integration: evaluation of the reasons for failure of integration during cartilage repair. A review. *Eur. Cell. Mater.* **16**, 26–39 (2008).
111. Guo, X. *et al.* Repair of osteochondral defects with autologous chondrocytes seeded onto bioceramic scaffold in sheep. *Tissue Eng.* **10**, 1830–1840 (2004).
112. Gao, J., Dennis, J. E., Solchaga, L. A., Goldberg, V. M. & Caplan, A. I. Repair of Osteochondral Defect with Tissue-Engineered Two-Phase Composite Material of Injectable Calcium Phosphate and Hyaluronan Sponge. *Tissue Eng.* **8**, 827–837 (2002).
113. Tuli, R. *et al.* Human Mesenchymal Progenitor Cell-Based Tissue Engineering of a Single-Unit Osteochondral Construct. *Tissue Eng.* **10**, 1169–1179. (2004).
114. Kempson, G. E., Spivey, C. J., Swanson, S. A. V & Freeman, M. A. R. Patterns of cartilage stiffness on normal and degenerate human femoral heads. *J. Biomech.* **4**, (1971).
115. Mow, V. C., Gibbs, M. C., Lai, W. M., Zhu, W. B. & Athanasiou, K. A. Biphasic indentation of articular cartilage-II. A numerical algorithm and an experimental study. *J. Biomech.* **22**, 853–861 (1989).
116. Setton, L. A., Zhu, W. & Mow, V. C. The biphasic poroviscoelastic behavior of articular cartilage: Role of the surface zone in governing the compressive behavior. *J. Biomech.* **26**, 581–592 (1993).
117. Carrier, R. L. *et al.* Cardiac tissue engineering: Cell seeding, cultivation parameters, and tissue construct characterization. *Biotechnol. Bioeng.* **64**, 580–589 (1999).
118. Armstrong, C. G. & Mow, V. C. Variations in the intrinsic mechanical properties of human articular cartilage with age, degeneration, and water content. *J. Bone Joint Surg. Am.* **64**, 88–94 (1982).
119. Brown, T. D. & Singerman, R. J. Experimental determination of the linear biphasic constitutive coefficients of human fetal proximal femoral chondroepiphysis. *J. Biomech.* **19**, 597–605 (1986).
120. Bursać, P. M., Obitz, T. W., Eisenberg, S. R. & Stamenović, D. Confined and unconfined stress relaxation of cartilage: Appropriateness of a transversely isotropic analysis. *J. Biomech.* **32**, 1125–1130 (1999).
121. DiSilvestro, M. R. & Suh, J. K. F. A cross-validation of the biphasic poroviscoelastic model of articular cartilage in unconfined compression, indentation, and confined compression. *J. Biomech.* **34**, 519–525 (2001).
122. Woodfield, T. B. F. *et al.* Polymer scaffolds fabricated with pore-size gradients as a model for studying the zonal organization within tissue-engineered cartilage constructs. *Tissue Eng.* **11**, 1297–311 (2005).
123. Hunter, W. Of the structure and disease of articulating cartilages. 1743. *Clin. Orthop. Relat. Res.* **42**, 3–6 (1995).
124. Doherty, M. Articular Cartilage and Osteoarthritis. *Ann. Rheum. Dis.* **51**, 1028–1028 (1992).
125. Roberts, C. R. *et al.* Ultrastructure and tensile properties of human tracheal cartilage. *J. Biomech.* **31**, 81–86 (1997).
126. Williamson, A. K., Chen, A. C., Masuda, K., Thonar, E. J. M. A. & Sah, R. L. Tensile mechanical properties of bovine articular cartilage: Variations with growth and relationships to collagen network components. *J. Orthop. Res.* **21**, 872–880 (2003).

BIBLIOGRAPHY

127. Shepherd, D. E. T. & Seedhom, B. B. The 'instantaneous' compressive modulus of human articular cartilage in joints of the lower limb. *Rheumatology* **38**, 124–132 (1999).
128. Shepherd, D. E. T. & Seedhom, B. B. A technique for measuring the compressive modulus of articular cartilage under physiological loading rates with preliminary results. *Proc. Inst. Mech. Eng. Part H J. Eng. Med.* **211**, 155–165 (1997).
129. Chen, A. C., Bae, W. C., Schinagl, R. M. & Sah, R. L. Depth- and strain-dependent mechanical and electromechanical properties of full-thickness bovine articular cartilage in confined compression. *J. Biomech.* **34**, 1–12 (2001).
130. Berteau, J. P., Oyen, M. & Shefelbine, S. J. Permeability and shear modulus of articular cartilage in growing mice. *Biomech. Model. Mechanobiol.* **15**, 205–212 (2016).
131. Hayes, W. Some viscoelastic properties of human articular cartilage. *Acta Orthop. Belg.* **38 Suppl 1**, 23–31 (1972).
132. Jurvelin, J. S., Buschmann, M. D. & Hunziker, E. B. Optical and mechanical determination of Poisson's ratio of adult bovine humeral articular cartilage. *J. Biomech.* **30**, 235–241 (1997).
133. Jin, H. & Lewis, J. L. Determination of Poisson's Ratio of Articular Cartilage by Indentation Using Different-Sized Indenters. *J. Biomech. Eng.* **126**, 138 (2004).
134. Choi, A. P. C. & Zheng, Y. P. Estimation of Young's modulus and Poisson's ratio of soft tissue from indentation using two different-sized indentors: Finite element analysis of the finite deformation effect. *Med. Biol. Eng. Comput.* **43**, 258–264 (2005).
135. Wang, C. C. B., Hung, C. T. & Mow, V. C. An analysis of the effects of depth-dependent aggregate modulus on articular cartilage stress-relaxation behavior in compression. *J. Biomech.* **34**, 75–84 (2001).
136. Wilson, W., Huyghe, J. M. & Van Donkelaar, C. C. Depth-dependent compressive equilibrium properties of articular cartilage explained by its composition. *Biomech. Model. Mechanobiol.* **6**, 43–53 (2007).
137. Mow, V. C., Holmes, M. H. & Michael Lai, W. Fluid transport and mechanical properties of articular cartilage: A review. *Journal of Biomechanics* **17**, 377–394 (1984).
138. Ateshian, G. A., Warden, W. H., Kim, J. J., Grelsamer, R. P. & Mow, V. C. Finite deformation biphasic material properties of bovine articular cartilage from confined compression experiments. *J. Biomech.* **30**, 1157–1164 (1997).
139. Frisbie, D. D., Cross, M. W. & McIlwraith, C. W. A comparative study of articular cartilage thickness in the stifle of animal species used in human pre-clinical studies compared to articular cartilage thickness in the human knee. *Vet. Comp. Orthop. Traumatol.* **19**, 142 (2006).
140. Shepherd, D. E. T. & Seedhom, B. B. Thickness of human articular cartilage in joints of the lower limb. *Ann. Rheum. Dis.* **58**, 27–34 (1999).
141. Sophia Fox, A. J., Bedi, A. & Rodeo, S. A. The Basic Science of Articular Cartilage: Structure, Composition, and Function. *Sports Health* **1**, 461–468 (2009).
142. Park, S., Krishnan, R., Nicoll, S. B. & Ateshian, G. A. Cartilage interstitial fluid load support in unconfined compression. *J. Biomech.* **36**, 1785–1796 (2003).

BIBLIOGRAPHY

143. Wall, A. & Board, T. Biosynthetic response of cartilage explants to dynamic compression. in *Classic Papers in Orthopaedics* 427–429 (2014). doi:10.1007/978-1-4471-5451-8_108
144. Jurvelin, J. S., Buschmann, M. D. & Hunziker, E. B. Mechanical anisotropy of the human knee articular cartilage in compression. *Proc. Inst. Mech. Eng. Part H J. Eng. Med.* **217**, 215–219 (2003).
145. Laasanen, M. S. *et al.* Biomechanical properties of knee articular cartilage. *Biorheology* **40**, 133–40 (2003).
146. Chen, S. S., Falcovitz, Y. H., Schneiderman, R., Maroudas, A. & Sah, R. L. Depth-dependent compressive properties of normal aged human femoral head articular cartilage: Relationship to fixed charge density. *Osteoarthr. Cartil.* **9**, 561–569 (2001).
147. McLeod, M. A., Wilusz, R. E. & Guilak, F. Depth-dependent anisotropy of the micromechanical properties of the extracellular and pericellular matrices of articular cartilage evaluated via atomic force microscopy. *J. Biomech.* **46**, 586–592 (2013).
148. Reignier, J. & Huneault, M. A. Preparation of interconnected poly(l-lactide-caprolactone) porous scaffolds by a combination of polymer and salt particulate leaching. *Polymer (Guildf).* **47**, 4703–4717 (2006).
149. Liao, C. J. *et al.* Fabrication of porous biodegradable polymer scaffolds using a solvent merging/particulate leaching method. *J. Biomed. Mater. Res.* **59**, 676–681 (2002).
150. Ho, M. H. *et al.* Preparation of porous scaffolds by using freeze-extraction and freeze-gelation methods. *Biomaterials* **25**, 129–138 (2004).
151. Xu, N. *et al.* 3D artificial bones for bone repair prepared by computed tomography-guided fused deposition modeling for bone repair. *ACS Appl. Mater. Interfaces* **6**, 14952–14963 (2014).
152. Gu, P. & Li, L. Fabrication of biomedical prototypes with locally controlled properties using FDM. *CIRP Ann. - Manuf. Technol.* **51**, 181–184 (2002).
153. Kalita, S. J., Bose, S., Hosick, H. L. & Bandyopadhyay, A. Development of controlled porosity polymer-ceramic composite scaffolds via fused deposition modeling. *Mater. Sci. Eng. C* **23**, 611–620 (2003).
154. Delabarde, C. Bioresorbable Nanocomposite Foams for Bone Tissue Engineering. (2011).
155. Martin, O. & Avérous, L. Poly(lactic acid): plasticization and properties of biodegradable multiphase systems. *Polymer (Guildf).* **42**, 6209–6219 (2001).
156. Mohapatra, A. K., Mohanty, S. & Nayak, S. k. Effect of PEG on PLA/PEG blend and its nanocomposites: A study of thermo-mechanical and morphological characterization. *Polym. Compos.* **35**, 283–293 (2014).
157. Pitt, G. G., Gratzl, M. M., Kimmel, G. L., Surles, J. & Sohindler, A. Aliphatic polyesters II. The degradation of poly (DL-lactide), poly (ε-caprolactone), and their copolymers in vivo. *Biomaterials* **2**, 215–220 (1981).
158. Veronese, F. M. & Pasut, G. PEGylation, successful approach to drug delivery. *Drug Discov. Today* **10**, 1451–1458 (2005).
159. Cao, H. & Kuboyama, N. A biodegradable porous composite scaffold of PGA/beta-TCP for bone tissue engineering. *Bone* **46**, 386–395 (2010).

BIBLIOGRAPHY

160. Haaparanta, A.-M. *et al.* Porous polylactide/beta-tricalcium phosphate composite scaffolds for tissue engineering applications. *J. Tissue Eng. Regen. Med.* **4**, 366–373 (2010).
161. Siqueira, L., Passador, F. R., Costa, M. M., Lobo, A. O. & Sousa, E. Influence of the addition of β -TCP on the morphology, thermal properties and cell viability of poly (lactic acid) fibers obtained by electrospinning. *Mater. Sci. Eng. C. Mater. Biol. Appl.* **52**, 135–143 (2015).
162. Inoguchi, H. *et al.* Mechanical responses of a compliant electrospun poly(L-lactide-co- ϵ -caprolactone) small-diameter vascular graft. *Biomaterials* **27**, 1470–1478 (2006).
163. Lia Rimondini, Nicolo Nicoli-Aldini, Milena Fini, Gaetano Guzzardella, Matilde Tschon, R. G. In vivo experimental study on bone regeneration in critical bone defects using an injectable biodegradable PLA/PGA copolymer. *Oral Surgery, Oral Med. Oral Pathol. Oral Radiol. Endodontology* **99**, 148–154 (2005).
164. N. Turner, B., Strong, R. & A. Gold, S. A review of melt extrusion additive manufacturing processes: I. Process design and modeling. *Rapid Prototyp. J.* **20**, 192–204 (2014).
165. Kong, Y. & Hay, J. N. The measurement of the crystallinity of polymers by DSC. *Polymer (Guildf)*. **43**, 3873–3878 (2002).
166. Henton, D. E., Gruber, P., Lunt, J. & Randall, J. Polylactic acid technology. *Nat. fibers, Biopolym. biocomposites* 527–577 (2005).
167. Boissard, C. Processing of Sustainable Cellular Biocomposites. (École polytechnique fédérale de Lausanne - EPFL, 2012).
168. Nofar, M. & Park, C. B. Poly (lactic acid) foaming. *Progress in Polymer Science* **39**, 1721–1741 (2014).
169. Chauvet, M., Sauceau, M. & Fages, J. Extrusion assisted by supercritical CO₂: A review on its application to biopolymers. *J. Supercrit. Fluids* **120**, 408–420 (2017).
170. Mantila Roosa, S. M., Kemppainen, J. M., Moffitt, E. N., Krebsbach, P. H. & Hollister, S. J. The pore size of polycaprolactone scaffolds has limited influence on bone regeneration in an in vivo model. *J. Biomed. Mater. Res. - Part A* **92**, 359–368 (2010).
171. Lien, S. M., Ko, L. Y. & Huang, T. J. Effect of pore size on ECM secretion and cell growth in gelatin scaffold for articular cartilage tissue engineering. *Acta Biomater.* **5**, 670–679 (2009).
172. Lee, S. T., Kareko, L. & Jun, J. Study of Thermoplastic PLA Foam Extrusion. *J. Cell. Plast.* **44**, 293–305 (2008).
173. Tai, H. *et al.* Control of pore size and structure of tissue engineering scaffolds produced by supercritical fluid processing. *Eur. Cell. Mater.* **14**, 64–77 (2007).
174. Tsivintzelis, I., Marras, S. I., Zuburtikudis, I. & Panayiotou, C. Porous poly(l-lactic acid) nanocomposite scaffolds prepared by phase inversion using supercritical CO₂ as antisolvent. *Polymer (Guildf)*. **48**, 6311–6318 (2007).
175. Collins, N. J., Bridson, R. H., Leeke, G. A. & Grover, L. M. Particle seeding enhances interconnectivity in polymeric scaffolds foamed using supercritical CO₂. *Acta Biomater.* **6**, 1055–1060 (2010).
176. Goel, S. K. & Beckman, E. J. Generation of microcellular polymeric foams using supercritical carbon dioxide. II: Cell growth and skin formation. *Polym. Eng. Sci.* **34**, 1148–1156 (1994).

BIBLIOGRAPHY

177. Zhou, C., Wang, P. & Li, W. Fabrication of functionally graded porous polymer via supercritical CO₂ foaming. *Compos. Part B Eng.* **42**, 318–325 (2011).
178. Hutmacher, D. W. Mechanical properties and cell cultural response of polycaprolactone scaffolds designed and fabricated via fused deposition modeling. *J. Biomed. Mater. Res.* **55**, 203–216 (2001).
179. Keeney, M. & Pandit, A. The osteochondral junction and its repair via bi-phasic tissue engineering scaffolds. *Tissue Eng. Part B. Rev.* **15**, 55–73 (2009).
180. Wang, F. *et al.* Precision extruding deposition and characterization of cellular poly- ϵ -caprolactone tissue scaffolds. *Rapid Prototyp. J.* **10**, 42–49 (2004).
181. Sachlos, E. & Czernuszka, J. T. Making scaffolds work: a review on the application of solid freeform fabrication technology to the production of tissue engineering scaffolds. *Eur. Cell Mater.* **5**, 29–40 (2003).
182. Dunkelman, N. S. *et al.* Cartilage production by rabbit articular chondrocytes on polyglycolic acid scaffolds in a closed bioreactor system. *Biotechnol. Bioeng.* **46**, 299–305 (1995).
183. Park, S. I., Rosen, D. W., Choi, S. kyum & Duty, C. E. Effective mechanical properties of lattice material fabricated by material extrusion additive manufacturing. *Addit. Manuf.* **1**, 12–23 (2014).
184. Yoon, Y. Heat expandable biopolymers for one-step production of foam core sandwich composites. (EPFL, 2016).
185. Chockalingam, K., Jawahar, N., Chandrasekar, U. & Ramanathan, K. N. Establishment of process model for part strength in stereolithography. *J. Mater. Process. Technol.* **208**, 348–365 (2008).
186. Pilipović, A., Raos, P. & Šercer, M. Experimental analysis of properties of materials for rapid prototyping. *Int. J. Adv. Manuf. Technol.* **40**, 105–115 (2009).
187. Jain, P. K., Pandey, P. M. & Rao, P. V. M. Effect of delay time on part strength in selective laser sintering. *Int. J. Adv. Manuf. Technol.* **43**, 117–126 (2009).
188. Es-Said, O. S. *et al.* Effect of Layer Orientation on Mechanical Properties of Rapid Prototyped Samples. *Mater. Manuf. Process.* **15**, 107–122 (2000).
189. Plummer, C. J. G., Bourban, P. E., Zanetto, J. E., Smith, G. D. & Manson, J. A. E. Nonisothermal fusion bonding in semicrystalline thermoplastics. *J. Appl. Polym. Sci.* **87**, 1267–1276 (2002).
190. Zanetto, J. E., Plummer, C. J. G., Bourban, P. E. & Manson, J. A. E. Fusion bonding of polyamide 12. *Polym. Eng. Sci.* **41**, 890–897 (2001).
191. Kikuchi, M. *et al.* Development of guided bone regeneration membrane composed of ??-tricalcium phosphate and poly (L-lactide-co-glycolide-co-??- caprolactone) composites. *Biomaterials* **25**, 5979–5986 (2004).
192. Abràmoff, M. D., Magalhães, P. J. & Ram, S. J. Image processing with imageJ. *Biophotonics International* **11**, 36–41 (2004).
193. Rasband, W. ImageJ. *U. S. Natl. Institutes Heal. Bethesda, Maryland, USA* //imagej.nih.gov/ij/ (2012).
194. Schneider, C. A., Rasband, W. S. & Eliceiri, K. W. NIH Image to ImageJ: 25 years of image analysis. *Nat. Methods* **9**, 671–675 (2012).

BIBLIOGRAPHY

195. Pasquale, J., Marascio, M. & Bourban, P.-E. *Medical grade filaments for Fused Deposition Modeling: Processing and Application to Osteochondral Tissue Engineering*. (2016).
196. Krauss, S. *et al.* Inhomogeneous fibril stretching in antler starts after macroscopic yielding: Indication for a nanoscale toughening mechanism. *Bone* **44**, 1105–1110 (2009).
197. Kikuchi, M. *et al.* Development of guided bone regeneration membrane composed of beta-tricalcium phosphate and poly (L-lactide-co-glycolide-co-epsilon-caprolactone) composites. *Biomaterials* **25**, 5979–86 (2004).
198. Gibson, L. J. & Ashby, M. F. *Cellular materials in nature and medicine. Integrative and Comparative Biology* **51**, (2010).
199. Matsuno, H., Matsuyama, R., Yamamoto, A. & Tanaka, K. Enhanced cellular affinity for poly(lactic acid) surfaces modified with titanium oxide. *Polym. J.* **47**, 505–512 (2015).
200. Ho, M.-H. *et al.* Promotion of Cell Affinity of Porous PLLA Scaffolds by Immobilization of RGD Peptides via Plasma Treatment. *Macromol. Biosci.* **6**, 90–98 (2006).
201. Serra, T., Mateos-Timoneda, M. A., Planell, J. A. & Navarro, M. 3D printed PLA-based scaffolds. *Organogenesis* **9**, 239–244 (2013).

CURRICULUM VITAE

MATTEO MARASCIO GREGORIO MODESTO

Route de la Maladière 16
1022 Chavannes-près-Renens

19.05.1989
Italian passport

+41 078 652 62 89
m.marascio@gmail.com

PROFESSIONAL EXPERIENCE

- 2014-2018 PhD Thesis in Material Science at the Swiss Federal Institute of Technology in Lausanne (EPFL) at the Laboratory for Processing of Advanced Composite (LPAC).
Title: "Hierarchical cellular structures produced by 3D Printing and Supercritical Foaming", in collaboration with the Laboratory of Biomechanical Orthopaedics (LBO) and the Centre Hospitalier Universitaire Vaudois (CHUV).
- 2014 Internship at the Laboratory of Polymer and Composite Technology (LTC)

EDUCATION

- 2014-2018 PhD Thesis at the Laboratory for Processing of Advanced Composite (LPAC), EPFL (CH)
- 2011-2013 Dual Master's Degree in Biomedical Engineering at Politecnico di Milano and Politecnico di Torino (IT)
- 2011-2013 Diploma from Alta Scuola Politecnica (IT)
- 2008-2011 Bachelor's Degree *cum laude* in Biomedical Engineering at Politecnico di Milano (IT)

VOULENTEERING AND LEADERSHIP EXPERIENCE

- 2016, 2017 Promoter and main organiser of two Doctoral Summer School on Additive Manufacturing of Polymers at the EPFL (CH), in collaboration with ETH (CH) and the CCMX (CH).

CONFERENCES AND AWARDS

- C1. M. Marascio et al., "Micro-macro porous 3D scaffold by 3D printing and supercritical foaming", SSB+RM 2015, Lausanne (EPFL), June 2015.
- C2. M. Marascio et al., "3D printing and supercritical foaming for novel hierarchical scaffolds", Biofabrication, Utrecht (NL), November 2015.
- C3. M. Marascio et al., "Hierarchical cellular materials: combining 3D printing and supercritical foaming", EPFL Material Science Research Day, Lausanne (CH), November 2015. **Best presentation award.**
- C4. M. Marascio et al., "Directional foaming of scaffold by integration of 3D printing and supercritical CO₂ foaming", World Biomaterial Congress 2016, Montreal (CA), May 2016.
- C5. M. Marascio et al., "Hierarchical macro-micro porous structures for Tissue Engineering applications", Micro- and Nanotechnology in Switzerland, Fribourg (CH), March 2017. **Invited speaker.**

CURRICULUM VITAE

- C6. M. Marascio et al. "3D printing of thermoplastic hierarchical foams", EUPOC 2017, Gargnano (IT), May 2017.
- C7. M. Marascio et al, "3D Printing method to produce hierarchical structure with continuous porosity gradient", EPFL Material Science Research Day, Lausanne (CH), June 2017. **Best poster award.**

PUBLICATIONS

- P1. Apicella, Alessandra, et al. "The Influence of Arginine on the Response of Enamel Matrix Derivative (EMD) Proteins to Thermal Stress: Towards Improving the Stability of EMD-Based Products." *PloS one* 10.12 (2015): e0144641.
- P2. Apicella, Alessandra, et al. "Scaffold requirements for periodontal regeneration with enamel matrix derivative proteins." *Colloids and Surfaces B: Biointerfaces* (2017).
- P3. Marascio, Matteo*, Apicella Alessandra* et al. "Molecular dynamics simulations of the intrinsically disordered protein amelogenin." *Journal of Biomolecular Structure and Dynamics* 35.8 (2017): 1813-1823. (*equal contribution)
- P4. Marascio, Matteo, et al. "3D Printing of Polymers with Hierarchical Continuous Porosity." *Advanced Materials Technologies* (2017).
- P5. Antons Jens, Marascio Matteo et al. "Depth-dependent mechanical properties of human articular cartilage obtained by indentation measurements". – *Submitted*.
- P6. Marascio, Matteo et al. "Foaming 3D Cellular Structure into 3D Dual Porous Structures by Homothetic Foaming" – *to be submitted*.
- P7. Marascio, Matteo et al. "Multi Material Hierarchical Structures Produced by Homothetic Foaming" – *to be submitted*.

PATENTS

- P1. Marascio, Matteo et al. "Hierarchical porous structure", EP17171756.4.

